A NUMERICAL STUDY OF MAGNETIC AND NON-MAGNETIC GEOPHYSICAL FLUID DYNAMICS

by

PAUL FOTHERINGHAM

A thesis submitted to the Faculty of Science, University of Glasgow, for the degree of Doctor of Philosophy

Department of Mathematics,
University of Glasgow
March 2000

ProQuest LLC.
789 East Eisenhower Parkway
P.O. Box 1346
Ann Arbor, MI 48106 – 1346

Contents

List of Figures

List of Tables

Preface

This thesis is submitted to the University of Glasgow in accordance with the requirements for the degree of Doctor of Philosophy. No part of it has been previously submitted by the author for a degree at any other University. The results contained in this thesis are claimed as original except where indicated in the text.

The majority of the calculations which form the basis of this thesis were performed on DEC ALPHA, SUN and SGI workstations.

Acknowledgements

I would like to express my thanks to my supervisor, Dr. Rainer Hollerbach, for his advice and guidance throughout my period of research. I would also like to acknowledge the help and support received from the Department of Mathematics, in particular the generous amount of computing time allocated to me.

I am grateful to the Engineering and Physical Sciences Research Council who provided funding for this work through a research studentship, award reference number 96004646.

During my time as a postgraduate I was made welcome by the other research students, a few of which I would like to take the opportunity to mention here: Graeme Morrison for many helpful discussions, Wasiq Hussain for having a joke for every occasion, and finally, my office companions for proving that all mathematicians are a commutative law short of an Abelian group.

Finally, I would like to thank my family for their continued support throughout my time at Glasgow University. I thank my sister for taking the time to proof read this work from a non-technical standpoint. However, I accept the responsibility for any mistakes that may still be present. Special thanks are due to my mother who very kindly supplied an endless stream of high quality packed lunches without missing a single day.

Summary

The subject of fluid dynamics contains some of the last remaining unsolved challenges in classical physics. In particular, the dynamics of rotating fluids still pose many unanswered questions despite the availability of modern supercomputers. It is often the case that the parameter regimes in which we are interested are those which are the most difficult to reach. It is therefore common to focus on specific aspects of a problem rather than try to solve the complete set of governing equations.

In the case of rotating fluid dynamics, one such aspect is that of inertial modes. These are oscillations of the fluid arising solely from the pressure and Coriolis forces in the momentum equation. In a sphere or spherical shell, inertial modes may be excited and maintained by precession of the rotation axis. In the first part of this thesis we shall consider the unforced inertial oscillations in spherical geometry. This simplified approach still gives us slowly decaying inertial modes which we believe will exhibit the same behaviour as their forced counterparts. The motivation for studying this problem is to try to explain the origin of the internal shear layers that are known to exist within the structure of these modes.

In the second part of this thesis we move into the realm of Magnetohydrodynamics where the rotating fluid is now treated as an electrical conductor and can therefore conduct currents under the action of electromagnetic fields. Again we focus on one specific area, that of magnetic stability, as opposed to solving the full 3-D dynamo equations. Here we are interested in the stability of axisymmetric magnetic fields (generated via an alpha effect) to nonaxisymmetric perturbations. This analysis will

help to determine how strong a field we can expect to find in the liquid iron core of the Earth and if it is possible for that field to equilibrate at lower field strengths than the critical onset value. This may be important in understanding the mechanism of geomagnetic reversals.

Chapter 1

Introduction

When Sir Isaac Newton wrote his masterpiece, the Principia, in the 17th century, the subject of fluid dynamics was still in its infancy. Indeed, it was not until the mid 18th century that the concept of an internal pressure was introduced by John Bernoulli. Soon after, Euler put forward a set of equations which would govern the motion of an inviscid fluid ie. a fluid which feels no frictional forces between adjacent moving parts. It was apparent from experiment that the behaviour of a fluid with very little viscosity would usually bear no resemblance to the predictions of the purely inviscid theory and so a theory of viscosity was required to provide a better understanding of the problem. This was introduced by Cauchy in 1822 in the form of a stress tensor and by the mid 19th century the framework was complete with Stokes supplying the necessary constitutive law describing the compressibility of the fluid.

The equation of motion as we would write it today is,

$$\frac{\partial \mathbf{u}}{\partial t} + (\mathbf{u}.\nabla)\mathbf{u} = -\frac{1}{\rho}\nabla P + \nu\nabla^2\mathbf{u} + \mathcal{F} \tag{1.1}$$

and the constitutive law for an incompressible fluid is simply given by,

$$\nabla \cdot \mathbf{u} = 0 \tag{1.2}$$

Here $\mathbf{u}$ represents the fluid velocity, ρ the (constant) density and ν the viscosity of the fluid. The $\mathcal{F}$ term represents whatever body forcing is applied to the fluid. It is

clear that if one sets ν=0 and looks at the inviscid case then eq(1.1) changes character and the number of boundary conditions required is reduced. For $\nu = 0$ a no normal flow condition is usually imposed for non-porous boundaries, whereas with a finite ν something more is required. This typically takes the form of a no-slip condition, whereby fluid cannot move relative to the boundary, or a stress-free condition, where the fluid exerts no tangential stress on the adjacent boundary. In either of these cases one will invariably find boundary layers developing in the flow when ν becomes small. This is due to the bulk of the interior flow behaving as if $\nu = 0$ as one would intuitively expect. In general this interior inviscid flow does not satisfy the boundary conditions and so an adjustment has to be made over a short lengthscale to match things up. This narrow region is called a boundary layer .These are typically regions of high shear and can make some problems of vanishing viscosity difficult to solve numerically. If solved analytically, then a common approach is to expand the velocity field, $\mathbf{u}$, into an inviscid part and a boundary layer flow.

1.1 Rotating fluids and inertial oscillations

When one considers the problem of a rotating fluid in a container the same boundary layers exist and are called Ekman layers. These are by no means the only shear layers that can accumulate in the flow and hence are not always the primary limiting factor for numerical computation. Another example is the Stewartson layer, first studied analytically by Proudman (1956) and later Stewartson (1957,1965). This particular example illustrates the active roles that shear layers (in this case the Ekman layers) may play in the overall solution to a hydrodynamic problem.

The Stewartson layer arises in a spherical shell where the inner and outer boundaries rotate at slightly different angular frequencies. Proudman found that the layer manifests itself on the *tangent cylinder* - the cylinder parallel to the rotation axis which is tangent to the inner sphere at the equator. An important feature which emerged

from the analysis was that the flow had a different structure in the two regions separated by the tangent cylinder. Outside the cylinder, where the only surfaces in contact with the fluid are the top and bottom outer boundaries, the fluid rotates rigidly with the angular velocity of the outer boundary. Inside the cylinder, the inviscid body also rotates rigidly but with an angular velocity that is the average of the inner and outer boundaries. Ekman layers must consequently form but not merely for the purpose of matching the angular velocities of the fluid to the boundary. If one assumes that the inner boundary has the lower angular velocity then fluid there will be expelled along the boundary away from the rotation axis. Similarly, fluid at the outer boundary will do the opposite and so the top Ekman layer transports fluid towards the axis. Since the flow is incompressible there is a secondary mainstream flow set up whereby fluid from the outer boundary flows down to the inner boundary. The Stewartson layer matches the angular velocities between the internal and external regions of the tangent cylinder but more importantly transports fluid upwards along its own length, thus completing a circuit with the Ekman layers and the secondary flow.

From this illustrative example it is clear that shear layers in rotating fluids are not always present just to smooth out large velocity differences but may play a key role in fluid transport. In other words, if shear layers are found in the solution of a hydrodynamic problem then one would like to be sure that the exact purpose of that layer is clear.

Having established this, we will now concern ourselves with another type of shear layer altogether. It is known that inertial oscillations of a rotating fluid may support internal shear layers, the exact purpose of which is not clearly known. The nondimensionalised momentum equation for fluid motion with respect to a reference frame attached to the rotating container is,

$$\frac{\partial \mathbf{u}}{\partial t} + (\mathbf{u}\cdot\nabla)\mathbf{u} + 2\hat{\mathbf{k}}\times\mathbf{u} = -\nabla P + E\nabla^2\mathbf{u} + \mathcal{F} \tag{1.3}$$

where the Ekman number, E, is defined as

$$E = \frac{\nu}{\Omega \mathcal{L}^2} \tag{1.4}$$

Here we have nondimensionalised length by the gap width ie. the difference between outer and inner radii. This is denoted by $\mathcal{L}$ and for the Earth is about 2260km. Time is measured by the rotational timescale Ω^{-1} and the scale for $\mathbf{u}$ is then simply taken as $\mathcal{L}/\Omega^{-1}$. P and $\mathcal{F}$ are now suitably non-dimensionalised pressure and forcing respectively, with $\hat{\mathbf{k}}$ the unit vector in the direction of the rotation axis, here taken to be the z direction. We can ignore the other inertial force which normally arises, the centrifugal force, since this can be incorporated as a modified pressure gradient, as can the self gravitation of our system.

Now that we are in a rotating non-inertial frame we have introduced the Coriolis force $2\hat{\mathbf{k}} \times \mathbf{u}$ to our equations. This force plays a key role not only in the study of inertial modes, as we shall see shortly, but in the whole theory of rotating fluids. To illustrate this point, consider a force balance dominated by the Coriolis force and pressure gradients alone. Eq(1.3) becomes,

$$2\hat{\mathbf{k}} \times \mathbf{u} \approx -\nabla P \tag{1.5}$$

Upon taking the curl of both sides we obtain

$$\frac{\partial \mathbf{u}}{\partial z} \approx 0 \tag{1.6}$$

This is known as the Taylor-Proudman theorem and shows that flows in rapidly rotating systems will attempt to be independent of the co-ordinate parallel to the rotation axis. In the presence of viscosity or other such forces this constraint may be broken. Returning to the example of the Stewartson layer, we see that the mainstream flow in the regions either side of the tangent cylinder satisfy the above constraint. For the inertial modes we will consider next, it is unlikely that the constraint will be adhered

to, since these oscillations have rapid timescales leading to an O(1) balance involving the inertial terms (hence the nomenclature).

What are inertial oscillations? In reality these are nothing more than the normal modes of eq(1.3) where the entire fluid oscillates with the same frequency. The restoring force for these oscillations is a combination of the Coriolis force and the pressure gradient. Many studies of these modes have taken place in the context of precessing flows (Bondi & Lyttleton 1953, Stewartson & Roberts 1963, Busse 1968). If precession is present then this can act as a forcing to the flow (Malkus 1968) and can therefore maintain these oscillations at a constant amplitude. To see why this is so mathematically, it is easiest to look at the equivalent of eq(1.3) in the precessing frame. This can be obtained by simply making the following substitutions into eq(1.3),

$$\hat{\mathbf{k}} \rightarrow \hat{\mathbf{k}} + \Omega_{\mathbf{P}} \quad , \quad \mathcal{F} = (\hat{\mathbf{k}} \times \Omega_{\mathbf{P}}) \times \mathbf{r} \tag{1.7}$$

where Ω_P is the ratio of the precessional angular frequency to the basic rotation frequency. The new inertial force that appears is called the Poincaré force and is clearly similar in form to the centrifugal force. The crucial difference between these two forces is that the Poincaré force cannot be folded into the pressure term as a gradient of some potential. Instead this force supplies a net torque to the fluid and can drive the flow. One of the earliest studies made of this system was by Poincaré (1910), hence the nomenclature. For the geometry of an oblate spheroid, he found an exact analytic solution to the governing equations,

$$u_r = 0, \quad u_\theta = -a(\eta, \Omega)(1+\eta) r \sin(\phi + t), \quad u_\phi = -a(\eta, \Omega)(1+\eta) r \cos\theta \cos(\phi + t) \tag{1.8}$$

where η is the oblateness of the spheroid and where the amplitude, a, can be given explicitly in terms of η and Ω. This solution represents a rotation of fluid about an axis displaced slightly from the container's rotation axis and is commonly referred to as the "spinover" mode. For an account of the structure and stability of this

solution see Kerswell (1993). Since the motion has no viscous dissipation, eq(1.8) is independent of E and is an exact, finite amplitude solution of eqs(1.3),(1.7). It does not, however, satisfy no-slip boundary conditions, although it does satisfy stress free boundary conditions in the special case of an exact sphere. (Here the motion is a spherical rigid body rotation.)

It should be noted that even though eq(1.8) is a nonlinear solution of eqs(1.3),(1.7) we are not really interested in the fully nonlinear problem, the reason being that precession is generally a small effect. For example, the Earth's precession rate due to its interaction with the Sun and the Moon is 7.72×10^{-12} rad s^{-1} whereas the sidereal rotation rate is 7.27×10^{-5} rad s^{-1}. A spinover mode for the Earth would therefore only deviate slightly from a solid body rotation aligned with the sidereal rotation axis. As such, we can then describe the behaviour using the linearised form of eq(1.3) in the original nonprecessing frame.

If no-slip boundary conditions are applied then there will inevitably be Ekman boundary layers developing. Normally in rotating fluid problems the width of the Ekman layer scales as $E^{1/2}$ for these particular boundary conditions. However, Roberts & Stewartson (1963) showed this scaling breaks down at critical latitudes. This had already been hinted at in the work of Bondi & Lyttleton (1953) who studied a spherical cavity under precession. Their method of assuming a constant width Ekman layer to correct for the effects of viscosity yielded a contradiction on attempting to solve their equations. The results found by Roberts & Stewartson suggested that the width of the Ekman layer should actually scale as $E^{2/5}$ at the critical latitude. Furthermore, the critical latitude itself has a finite extent along the boundary and this was found to scale as $E^{1/5}$.

The question of what effect these boundary layer breakdowns will have on the flow in the interior has remained open for some time. Greenspan (1968) suggested that the breakdown regions might initiate the formation of shear layers along the characteristic

directions of the system. These are lines, or surfaces depending on the dimensionality of the system, associated with hyperbolic equations, along which discontinuities in boundary conditions can propagate. Walton (1975) used a non-precessing split-disk configuration to focus on the effect of a discontinuity in the boundary condition and found that the irregularity in the boundary was indeed propagated along the characteristics. His analysis showed that in the limit $E \to 0$, the shear layers obtained had widths scaling as $E^{1/3}$ and that in the inviscid case there would be singular surfaces on the characteristics. This study was extended by Kerswell (1995) who also used the split-disk system. For the discontinuous boundary conditions he confirmed the existence of internal shear layers and showed that they can carry sufficient angular momentum to influence the mean flow. Unfortunately he was unable to give details of exactly how the mean flow is affected but he did manage to calculate the scalings for the widths of the shear layers by smoothing the boundary discontinuity. If this was smoothed over an extent less than the natural $E^{1/3}$ width of the shear layers then they would be unable to see the fine structure at the boundary. Instead they would behave as if there was a discontinuous boundary condition and hence retain their $E^{1/3}$ scaling. On the other hand, if the smoothing was over a larger extent then the layers would see this fine structure and adapt to it with the appropriate scaling.

Returning then to the original problem, we would like to know how these results will affect the solution in a precessing spheroidal body. The first thing to note is that with all the different possible scalings which are possible in the flow, one would have to take a very complicated expansion for $\mathbf{u}$ to do a standard asymptotic analysis. Thus, as Kerswell pointed out, there is little progress to be made by looking at the problem any further analytically. Instead, we may be able to gain some insight into the workings of the problem via a numerical approach. From a numerical point of view, it is much simpler to work in a purely spherical geometry than a spheroidal one. As a consequence, however, the precessional motion of the container can no longer be

transmitted to the fluid via surface pressures. This leaves the small viscous forces on their own and so it is simpler instead to consider the unforced momentum equation (1.3) with $\mathcal{F} = 0$. The justification for this is that the unforced form of eq(1.3) also supports a spinover mode, albeit slowly decaying due to the effects of viscosity. The spinover mode is an inertial oscillation of particular interest since it is experimentally the easiest to excite. Simply let the fluid spin up with the rotating container to a solid body rotation and then impulsively tip the rotation axis of the container to obtain the spinover mode. As was noted by Greenspan (1968), precession is nothing more than a sequence of infinitesimal changes in the direction of the rotation axis and hence the spinover mode is likely to be important.

Not only does eq(1.3) support a spinover mode but it also has the predicted shear layers. These were first analysed numerically by Hollerbach & Kerswell (1995) for both a full sphere and a spherical shell. They studied the linearised form of eq(1.3) and explicitly substituted in the normal mode time dependence $e^{i\omega t}$ giving,

$$i\omega\mathbf{u} + 2\hat{\mathbf{k}} \times \mathbf{u} = -\nabla P + E\nabla^2\mathbf{u} \tag{1.9}$$

The linear theory of inertial modes is well documented by Greenspan (1968) who showed that the frequency of a single mode must lie in the range $-2 < \omega_r < 2$ ($\Re\{\omega\} = \omega_r$). The spinover mode has the purely real frequency of 1 in the inviscid case but has a complex frequency with $\omega_r \approx 1$ when E is finite. When $E = 0$, eq(1.9) is hyperbolic and has characteristic surfaces. These are cones, coaxial with the rotation axis and with half angles, φ, given by,

$$\varphi = \sin^{-1}\left(\frac{\omega_r}{2}\right) \tag{1.10}$$

which is also the latitude of the critical regions found in the previous studies. Hyperbolic systems allow the propagation of discontinuities in the boundary or initial conditions along the characteristics. Hollerbach & Kerswell looked at eq(1.9) with

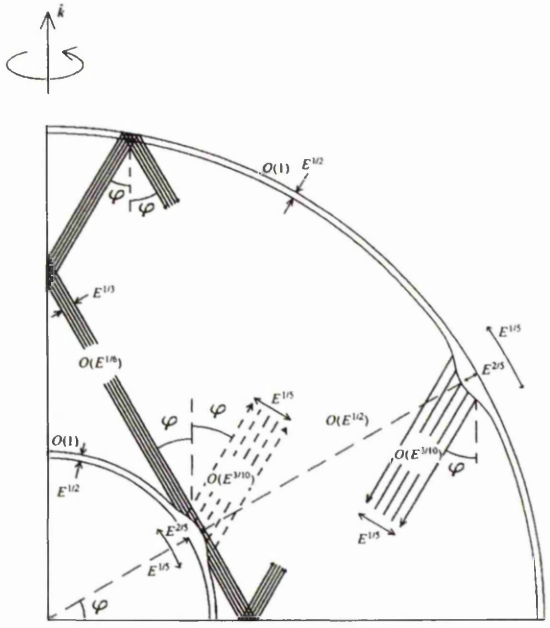

Figure 1.1: Orientations and predicted scalings of the internal shear layers associated with the spinover mode. (from Kerswell 1995)

finite E and tried to reduce viscosity as far as numerically possible. In this case the system is now elliptic and as such does not possess characteristic surfaces. However, one would still expect to see a smoothed out version of a discontinuity along the characteristics ie. shear layers. At the outer boundary, only one orientation is possible since the surface is concave to the fluid. At the inner boundary (if present) there are two possibilities, one where the characteristics of the associated hyperbolic system meet the surface tangentially and one where they come off at an angle φ. The different orientations are outlined in Figure 1.1.

Also marked on the diagram are the expected scalings for the shear layers obtained by applying the Roberts & Stewartson scalings for the critical regions to Kerswell's results for shear layer widths. The shear layers coming off the boundaries non-tangentially will see a generating region of width $E^{1/5} > E^{1/3}$ and hence adapt to an $E^{1/5}$ scaling. The tangential layer on the inner boundary sees the local modified Ekman layer width of $E^{2/5} < E^{1/3}$ and so takes on the larger $E^{1/3}$ scaling. In their

study, Hollerbach & Kerswell noted that only the tangential shear layer is spawned in the shell and that this layer is indeed thinner than the non-tangential layer seen in the full sphere for equivalent Ekman numbers. It is, however, difficult to obtain the precise scalings numerically as there is no clearly defined method for establishing the width of a given shear layer. The results of Hollerbach & Kerswell were certainly not inconsistent with the proposed scalings and so the analytic work seems to agree reasonably well with the numerical findings.

There is one other important point to note about inertial modes in a spherical shell which does not apply to the full sphere counterparts. As pointed out by Rieutord & Valdettaro (1997), it may not be possible to deduce asymptotic scaling laws for the decay rates as $E \to 0$. In their work they were able to give an example of a mode that had an increasing decay rate over a small range of decreasing E. This was shown to be directly attributable to a global change in the shear layer pattern resulting from small changes in frequency. Typically a given reflection pattern can exist over a small frequency interval due to the finite thickness of the layers. This interval becomes smaller and smaller with decreasing Ekman number which can result in two possibilities. On one hand, the variation in frequency of a mode with decreasing E will be small enough such that it always remains in the "stability" interval and an asymptotic scaling exists. On the other hand, the dependence of frequency on E will be large enough to destabilise the pattern. Rieutord & Valdettaro found that the destabilising of a given pattern always resulted in a more complicated pattern ie. one with more shear layers and hence greater global dissipation. This phenomenon could manifest itself indefinitely as the Ekman number is reduced thus eliminating the possibility of an asymptotic scaling law with E.

It is still not clear, however, why internal shear layers exist at all. Certainly hyperbolic systems allow discontinuities to propagate but is it always necessary? We aim to tackle this question by looking at the effect of the generating region more

closely. In particular we want to establish the dependence of internal shear layers on the boundary conditions imposed. Despite the spinover mode being of primary importance in many studies, we will not restrict ourselves to this one mode. This allows us to study the generic behaviour of the internal structure of inertial modes. These modes can play a role not just in the liquid outer core of the Earth but also in the dynamics of our atmosphere. The latter can also be modelled as a spherical shell but with different boundary conditions and so we will be able to establish the difference in behaviour, if any, between the two different applications.

1.2 Magnetic instabilities in rotating fluids

In the second part of this thesis we wish to extend our fluid dynamical problem to include the effects of electromagnetic fields. This is clearly needed to properly explain the dynamics of the core of the Earth since it is now widely accepted that the fluid motions which occur there maintain the geodynamo.

If the fluid is taken to be an electrical conductor, then currents may flow and subsequently generate magnetic fields. If one assumes the fluid is electrically neutral, then the effects of electric fields can be ignored and so the magnetic field will simply be referred to hereafter as the field. Magnetic fields, whether generated by the currents in the fluid or having external sources, can act back on the currents in the fluid. It is the form of Ohm's Law accounting for a moving conductor which plays a central role in MHD theory. By taking its curl and applying three of Maxwell's equations (ignoring displacement currents) it can be written in the following nondimensional form,

$$\frac{\partial \mathbf{B}}{\partial t} = \nabla \times (\mathbf{u} \times \mathbf{B}) + \nabla^2 \mathbf{B} \tag{1.11}$$

This is known as the induction equation and determines the evolution of the field under the influence of the flow and Ohmic dissipation. In the perfectly conducting limit where diffusion is absent it can be shown (see, for example, Moffatt 1978) that

lines of magnetic field behave exactly as if they were frozen into the fluid. This can be a useful aid in visualising the interaction between the flow and the field even in the finitely conducting regime provided diffusion is not too large. The momentum equation (1.3) now includes the Lorentz force, $\mathcal{F} = \mathbf{j} \times \mathbf{B}$ and since the current $\mathbf{j} = 1/\mu_0 \nabla \times \mathbf{B}$ this becomes,

$$Ro\left(\frac{\partial \mathbf{u}}{\partial t} + (\mathbf{u}.\nabla)\mathbf{u}\right) + 2\hat{\mathbf{k}} \times \mathbf{u} = -\nabla P + E\nabla^2 \mathbf{u} + (\nabla \times \mathbf{B}) \times \mathbf{B} \tag{1.12}$$

The Rossby number, $Ro = \eta/\Omega\mathcal{L}^2$ where η is the magnetic diffusivity, now appears because we are nondimensionalising time on the more appropriate and much slower magnetic diffusion time. Ro represents the ratio of inertial to Coriolis forces and is believed to be small for the Earth's core, possibly of order 10^{-9}. The magnetic field $\mathbf{B}$ here has been nondimensionalised as to keep the magnitudes of the Coriolis and Lorentz forces the same ie. $\mathcal{B} = \sqrt{\Omega\rho\mu_0\eta}$.

If one were to attempt to solve eqs(1.11),(1.12) as part of a full dynamo calculation, a third equation would be needed. The fluid motions can amplify the field and vice versa but a simple energetics argument shows that ultimately the system will decay to the trivial state due to the Ohmic and viscous dissipation. To have a self sustaining dynamo one needs to overcome these losses and there is a variety of ways to do this. As regards the geodynamo there are three possible candidates for energy sources. The first is the precession of the Earth as discussed in the previous section which was initially proposed by Malkus (1968). This is rarely used in geodynamo models since it is not clear that the process is efficient enough at converting energy for this to solely maintain the dynamo. Loper (1975) and Rochester et al. (1975) argued that precessionally induced laminar flow could not be a viable candidate for the dynamo energy source, however more recently Kerswell (1996), in the spirit of the original Malkus argument, has shown that a fully turbulent precessing core could more efficiently transform the available energy. Doubts certainly remain about precessional forcing but the concept

still enjoys some attention. For example, a recent study by Tilgner (1998) looked at the kinematic dynamo problem where the Poincaré flow is imposed and the growth or decay of solutions to eq(1.11) studied.

The other two energy sources are both buoyancy driven. One is due to compositional effects which arise due to the gradual freezing of outer core material onto the solid inner core. The outer core fluid is composed not only of iron, but also of small quantities of lighter elements, possibly sulphur, oxygen or silicon, which are segregated from the iron upon freezing. Since these elements are lighter they are therefore buoyant and will rise up through the core thus stirring the fluid. A "mushy zone" is expected at the inner core boundary (ICB) (Loper & Roberts 1981) consisting of a mixture of fluid and solid where the solid part may take the form of dendrites. The thickness of this zone is not clear since theoretically the entire inner core should be mushy with the mass fraction of solid increasing with depth. In contrast, seismic evidence suggests a sharp transition at the ICB. In terms of the governing equation then the buoyant material in the body of the fluid can easily enough be modelled by a standard buoyancy equation but the boundary conditions are not so obvious with the possible finite thickness of the mushy zone. The concept of a compositionally powered dynamo was first proposed by Braginsky (1963) although Verhoogen (1961) had previously noted that the freezing process could be an energy source for the dynamo.

The other buoyancy related forcing is a purely thermal effect and can be driven partly by the latent heat released during the freezing process, specific heat released due to the cooling of the inner core, and also partly by radiogenic heating in the core itself. The radiogenic heating is likely to come from the decay of K^{40} which could possibly exist with iron at core pressures (Parker et al. 1996). However it is not clear whether the sparseness of potassium in the mantle justifies a higher abundance in the core since the compositions of Venus and Mars point to an overall lack of potassium in the terrestrial planets (Liu 1986). Numerous reports suggest that thermal buoyancy is

not as efficient as compositional buoyancy (see for example Loper (1978), Gubbins et al. (1979)) and much of the heat that is generated could simply be conducted away. Thermal buoyancy is easy to model though and has received considerable attention (see for example Olson et al. (1999), Kuang & Bloxham (1997), Zhang & Jones (1996), Katayama et al. (1999) and Walker & Barenghi (1997)).

Despite the fierce debate over which of the two forms of buoyancy is likely to dominate, the general consensus now is that both are likely to play an equally important role, as pointed out by Braginsky & Roberts (1995). Some of the major 3-D simulations are now using combined compositional and thermal buoyancies (Glatzmaier & Roberts 1996). These fully consistent 3-D simulations are, however, very costly in terms of CPU and are only feasible on the quickest of supercomputers. For this reason it is common to study a "watered down" version of the dynamo problem to attempt to obtain a numerically tractable problem. One such approach is to restrict attention to the so called "$2\frac{1}{2}$D" model where the axisymmetric state is solved for, in addition to a sole nonaxisymmetric mode chosen arbitrarily. These models allow a wider range of parameter space to be covered and have been used by Sarson et al. (1998) and Morrison & Fearn (2000) amongst others.

Despite its advantages the $2\frac{1}{2}$D model is clearly badly resolved in the azimuthal direction. To regain the resolution and become fully 3-D again one needs to simplify some other part of the problem. One way to do this is to bypass the geophysical forcing mechanisms outlined above. Indeed we use an extreme application of this in our non-magnetic study of inertial modes covered in the previous section. There we simply ignored the forcing altogether but in the dynamo problem we must of course provide some forcing, otherwise what we are modelling is not a dynamo anymore!

A common way of bypassing the conventional forcing is by imposing a basic state and then perturbing that state and following the evolution of instabilities, if any. The basic state is not subject to diffusion and is therefore maintained indefinitely

and can act as a source of energy for the instabilities. This sort of analysis, while not strictly geophysically accurate, can certainly give information about the dynamo process. Since the mantle is an insulator, only the poloidal part of the field is visible at the surface of the Earth (for the mathematical definition of the poloidal and toroidal parts of the field, see eq(3.14). For axisymmetric fields, the toroidal part is nothing more than the ϕ component, with the poloidal part then being the remainder). If differential rotation is important in the core, as is believed to be the case, then the "hidden" toroidal component could be much larger than the observed poloidal part due to field line stretching by the flow. Magnetic stability analyses can provide upper bounds for the strength of the toroidal component of the field by investigating the onset of instability of a given field configuration.

Furthermore, if one follows the nonlinear evolution of an instability then one may gain insight into the reversal process of the geodynamo. Typically the geomagnetic field is stable for relatively long periods of time ($\sim 10^5$ years) but will reverse occasionally over a shorter timescale ($\sim 10^4$ years). Taking the basic state to represent the stable long term field, the evolution of the instability could be interpreted as the mechanism whereby the field reverses. This has been studied using a highly simplified model by Parker (1969) and Levy (1972) in the context of mean field dynamos. They envisaged a sudden change in the poloidal flow giving rise to reversal of toroidal field throughout the core, followed by the poloidal field. In particular, one would like to know if it is possible for the instability to evolve to a state with lower energy than at the critical point of stability. Numerous studies have been made to ascertain this information, which utilised the further simplification of a cylindrical model as opposed to the more realistic spherical geometry. This simplification was justified on the grounds that a rotating cylinder and a rotating sphere possess the same symmetries. Since our spherical study will extend the results of the previous cylindrical work we will now review the results to date.

The first numerical results to appear were from a series of studies by Fearn (1983, 1984, 1985 and 1988) where the imposed basic field took the form

$$\mathbf{B}_0 = B_M s F(s) \hat{\phi} \tag{1.13}$$

In magnetic stability analyses the field is typically nondimensionalised using a measure of the imposed field strength, here B_M. This introduces the Elsasser number to eq(1.12) as the coefficient of the Lorentz force which is therefore defined as

$$\Lambda = \frac{B_M^2}{\Omega \rho \mu_0 \eta} \tag{1.14}$$

This is the controlling parameter in magnetic stability studies and can be interpreted as a measure of magnetic diffusion, η, as well as imposed field strength. It is possible to define a more general version of the Elsasser number which more accurately represents the global variation of a given imposed field. We will define the energetic Elsasser number by

$$\Lambda' = \frac{\frac{1}{V}\int B^2 dV}{\Omega \rho \mu_0 \eta} \tag{1.15}$$

where V is the volume of the computational domain.

The work of Fearn suggested that $\Lambda \geq O(1)$ for instability. The classification of the instabilities was also investigated in terms of ideal and resistive modes. The ideal modes can exist in the diffusionless limit $\Lambda \to \infty$ and are triggered by gradients in the imposed field. The resistive modes depend on diffusion in the form of field line breaking and reconnection near critical surfaces. The difference can be easily identified in the limit $\Lambda \to \infty$ but recent work by McLean & Fearn (1996) has shown that it is impossible to separate the two for finite Λ.

Hutcheson & Fearn (1995) then investigated the nonlinear evolution of the instabilities of eq(1.13) for one particular choice of $F(s)$. The cylinder had an aspect ratio (height/radius) of $\pi/2$ and they were able to achieve an Ekman number of 4.5×10^{-3}

using a spectral- timestepping code. Equilibrated nonlinear solutions could only be found for $\Lambda > \Lambda_C$, indicative of a supercritical bifurcation. The solution in the supercritical regime was dominated by the most unstable axially dependent mode from the linear analysis (in a cylinder, modes with an axial wavenumber of zero may exist providing the ends are stress free and perfectly conducting, but they are nevertheless unphysical because they imply an infinite lengthscale in the z direction). The nonaxisymmetric part took the form of an azimuthally drifting wave with a frequency similar to that of the most unstable mode. The axisymmetric flow contained some regions of differential rotation, which is typically a destabilising feature and so might have been expected to induce subcriticality.

Two later papers, Hutcheson & Fearn (1996, 1997), then investigated the influence a z-dependence in the basic state might have on the critical linear onset parameters and then the equilibrated nonaxisymmetric solution. This allowed a more realistic dipole basic state to be considered as well as some more complicated quadrupole states. The importance of critical surfaces, where $\mathbf{k} \cdot \mathbf{B}_0 = 0$ for an instability of wavenumber $\mathbf{k}$, was also investigated. It was postulated and subsequently confirmed that the dipole states were more prone to instability than the quadrupole due to the extra critical surface at the equator. Indeed for the dipole basic state which had the equator as its only critical surface, the linear eigenfunction was seen to concentrate about this region.

When the nonlinear evolution of the linear instabilities was followed it was again discovered that the azimuthal symmetry breaking bifurcation was supercritical in nature regardless of whether a dipole or quadrupole basic state was used. For both parities of basic state the first bifurcation was to a state with even azimuthal wavenumbers with dipole symmetry for the dipole state and quadrupole for the quadrupolar state. Attention was focussed then mainly on the dipole basic state which had two subsequent bifurcations as Λ was increased. The first was to a solution with all az-

imuthal wavenumbers still of dipole symmetry and the second was the transition to all azimuthal wavenumbers with mixed parity. For each bifurcation the effect of the symmetry breaking was to extract more energy from the basic state than was being done before the bifurcation. For the mixed parity solution the energy associated with the dipole part dominated the contribution from the quadrupole part. In the mixed parity regime it was also noted that the axisymmetric feedback from the nonaxisymmetric parts dominated over the energies from the individual nonaxisymmetric modes.

The final point they addressed is whether the solutions were in an Ekman state or a Taylor state. The origin of these two regimes can best be explained by considering the momentum equation in the magnetostrophic limit, when both inertia and viscosity are neglected. Setting Ro and E equal to zero in eq(1.12) gives

$$2\hat{\mathbf{k}} \times \mathbf{u} = -\nabla P + (\nabla \times \mathbf{B}) \times \mathbf{B} \tag{1.16}$$

and by integrating the ϕ component of this equation over an imaginary cylinder, $C(s)$, one then obtains

$$\int_{C(s)} u_s dS = \int_{C(s)} [(\nabla \times \mathbf{B}) \times \mathbf{B}]_\phi \, dS \quad , \quad \forall s \tag{1.17}$$

This applies everywhere in our domain, in particular our cylinders, $C(s)$, extend right up to the boundaries. Since we are modelling an incompressible flow this implies there can be no net flux of fluid out of the curved surface of $C(s)$. Hence we arrive at Taylor's constraint

$$\int_{C(s)} [(\nabla \times \mathbf{B}) \times \mathbf{B}]_\phi \, dS = 0 \quad , \quad \forall s \tag{1.18}$$

after Taylor (1963). Since E is very small in the Earth's core, one would like to know how this idealised expression is modified for small but finite viscosity. The cylinders, $C(s)$, no longer touch the boundaries, but instead extend only to the edge of the Ekman layers which must now exist. Applying a local Cartesian analysis to

calculate the Ekman flux correction of the boundary layer (Fearn 1994) one arrives at the expression

$$V_G(s) = E^{-\frac{1}{2}}\left(\frac{\cos\theta}{2}\right)^{\frac{1}{2}} \int_{z_{bottom}}^{z_{top}} \langle(\nabla \times \mathbf{B}) \times \mathbf{B}\rangle_\phi \, dz \tag{1.19}$$

where $\langle\rangle$ denotes the azimuthal average. The zonal flow V_G is known as the geostrophic flow, and can be thought of as the first nonlinear effect to become important. In other words, for small amplitudes, field equilibration in the weakly supercritical regime will be brought about by the geostrophic flow. If a solution equilibrates via this mechanism then it is said to be in an Ekman state. From eq(1.19) we have V_G of order 1 when $\mathbf{B}$ is $O(E^{1/4})$ and hence the solutions are dependent on viscosity. In the more strongly supercritical regime field equilibration will be dominated by other nonlinear effects and the solution should adapt to satisfy eq(1.18). This is achieved by internal cancellation in the integral since $\mathbf{B}$ is now $O(1)$ and the solutions are then independent of viscosity. This type of evolution for fluids of small viscosity is known as the Malkus-Proctor scenario after Malkus & Proctor (1975).

The solutions of Hutcheson & Fearn were found to be Ekman states with a clear dependence on the Ekman number. They did notice that the solutions became less viscously controlled at higher Λ but it was clear that their value of $E(= 4.5\times10^{-4})$ was still too large to access the magnetostrophic regime and be able to obtain true Taylor states. To be able to investigate Taylor states it is therefore not possible, at present, to use the conventional approach of retaining a finite E in the numerical calculation since Hutcheson & Fearn were already at the limit of computational resources. An alternative approach was adopted by Ogden & Fearn (1995), Fearn, Lamb, McLean & Ogden (1997) and McLean (1997) using the magnetostrophic approximation outlined earlier. The method was to solve eq(1.16) but retain the effects of viscosity in the boundary layers by solving eq(1.19) for the geostrophic flow.

Ogden & Fearn (1995) studied the effect of differential rotation on an imposed

field with thermal buoyancy acting as well. They found if the differential rotation contained large enough regions of negative shear ie. $d\Omega/ds < 0$ then the initial effect could be destabilising and that this effect was most prominent for high Roberts number $q = \nu/\kappa$. This was consistent with the local analysis of Acheson(1983), which had previously noted the destabilising effect of negative shear. The purpose of the other two studies was to isolate the effect that the differential rotation of the geostrophic flow might have on magnetic instabilities and to highlight potential differences with the finite E approach. By arbitrarily prescribing differential rotations $u_\phi = s\Omega(s)$ in the linear onset problem it was confirmed that regions of negative shear were required to reduce the critical Elsasser number, Λ_C, for instability. It was also demonstrated that differential rotation could destabilise a field which was magnetically stable. If the strength of the differential rotation was increased further then it became a stabilising agent for both magnetically stable and unstable fields. In the nonlinear regime various magnetically unstable field configurations were tried, with McLean (1997) including the realistic dipole field parity. For the s-dependent fields only those that concentrated field near to the inner core boundary produced subcritical bifurcations. This was consistent with the linear results since only for this field configuration did the associated V_G have significant regions of negative shear. The addition of z-dependence destabilised the system for dipole fields concentrated at the outer boundary but stabilised it for all other fields. However, in virtually all the cases tested the bifurcation was subcritical.

The subcriticality of the magnetostrophic solutions was a direct consequence of the initial destabilising effect of the geostrophic flow. The viscous analyses showed only supercritical behaviour since other nonlinear effects were dominant at the geophysically unrealistic value of E used. Both analyses were based in a cylindrical annulus model to enable a simplification of the governing equations, and indeed this would seem to be the "natural" geometry for the geostrophic flow since $V_G = V_G(s)$. However, in a

cylindrical geometry, where the end walls are flat, one can show that $V_G = V_G(s, \phi)$. This shows that the geostrophic flow behaves in a fundamentally different way in the two geometries, and so it is desirable to remove this inconsistency. We wish to extend the cylindrical model results to the realistic spherical shell geometry, where V_G really is only a function of s alone.

Walker & Barenghi (1998) have shown that there are difficulties in implementing the magnetostrophic approximation in a sphere. The internal cancellation in the Taylor integral when solutions are in Taylor states needs to be computed accurately, otherwise the geostrophic flow can act as an artificial source of energy which numerically destabilises the system rapidly. In a shell there is also the possibility of problems at the tangent cylinder, as pointed out by Hollerbach & Proctor (1993). The second problem can be circumvented by using a full sphere geometry and this is the approach we had originally hoped to take allowing us to model both the viscous and the magnetostrophic regimes. Unfortunately we encountered severe numerical instabilities when implementing the viscous code and were limited to Ekman numbers $E > 10^{-3}$. Subsequently we decided to focus attention on the spherical shell geometry to get better results for the viscous regime but at the same time sacrificing the magnetostrophic regime. We will be able to compare our results with the viscous studies of Hutcheson & Fearn and investigate whether subcriticality can exist in the spherical geometry at similar Ekman numbers to that used in the cylindrical analysis. We also hope to identify the role of differential rotation in our solutions.

Chapter 2

Inertial Modes

In this chapter we will be concerned with the topic of inertial oscillations in rapidly rotating spherical shells. This branch of fluid dynamics has many applications but is also of interest in its own right as a topic of fundamental importance. Geophysical models of both the molten outer core and the gaseous atmosphere can benefit from this study, but any system with a contained rotating fluid is relevant. In particular, the behaviour of the fluid propellant in spacecraft has received some attention (Kerswell 1996). In our study we will first demonstrate the existence of the shear layers and then proceed to examine the structure of the modes with respect to changes in the boundary conditions. We will be primarily interested in the combinations generated by two choices of boundary condition; no-slip and stress free. In the fluid outer core of the Earth it is believed that no-slip conditions are appropriate at both boundaries whereas a simple model of the atmosphere would have no-slip at the inner boundary and stress free at the outer. We will not restrict ourselves to these two combinations and will also analyse the additional two cases where both boundaries are stress free and where the inner is stress free and the outer no-slip.

For the spinover mode we know the difference is crucial. Poincaré's solution satisfies stress free conditions at each boundary in the case of a purely spherical shell. This solution represents nothing more than a solid body rotation of fluid and hence exhibits no shear layer structure whatsoever. The numerical study by Hollerbach & Kerswell

(1995) shows clearly that when no-slip conditions are implemented there is a shear layer structure superimposed on the underlying solid body rotation. Recalling from eq(1.10) that the shear layers are located on the characteristic cones one would expect the pattern to be inclined at 30^o to the rotation axis. This is exactly what was observed. One should also note that the shear layer reflection pattern obtained closes on itself exactly. One can show this is true for all inner core radii up to one half of the outer core radius and is not just a fluke result. We will take advantage of this fact later when we look for other modes to study.

2.1 Governing equations and numerical solution

We will study the unforced system of inertial modes in a spherical shell. We will also assume that we can linearise the momentum equation in the rotating frame. This is justified since precession is small compared to the underlying rotation rate and thus the fluid would be expected to deviate only slightly from solid body rotation with the container. For an incompressible fluid we therefore have

$$i\omega\mathbf{u} + 2\hat{\mathbf{k}} \times \mathbf{u} = -\nabla P + E\nabla^2\mathbf{u} \tag{2.1a}$$

$$\nabla \cdot \mathbf{u} = 0 \tag{2.1b}$$

where we have expressed the fluid velocity as $\mathbf{u}(r, \theta, \phi)e^{i\omega t}$ due to the linear nature of the problem. We will refer to $\omega_r = \Re(\omega)$ as the frequency of the mode and $\omega_i = \Im(\omega)$ as the decay rate.

The boundary conditions we will apply are represented by

$$\mathbf{u} = \mathbf{0} \tag{2.2a}$$

for no-slip, and

$$u_r = \frac{\partial}{\partial r}\left(\frac{u_\theta}{r}\right) = \frac{\partial}{\partial r}\left(\frac{u_\phi}{r}\right) = 0 \tag{2.2b}$$

for stress free.

To satisfy eq(2.1b), we use the familiar poloidal-toroidal decomposition for the flow field in its full nonaxisymmetric form

$$\mathbf{u} = \nabla \times (e\hat{\mathbf{r}}) + \nabla \times \nabla \times (f\hat{\mathbf{r}}) \tag{2.3}$$

where the defining scalars e and f are subsequently expanded as

$$e(r,\theta,\phi) = \sum_{n=1}^{N} e_n(r) P_{n_1}^{(m)}(\cos\theta)\exp[im\phi + i(\omega_0 + \tilde{\omega})t] \tag{2.4a}$$

$$f(r,\theta,\phi) = \sum_{n=1}^{N} f_n(r) P_{n_2}^{(m)}(\cos\theta)\exp[im\phi + i(\omega_0 + \tilde{\omega})t] \tag{2.4b}$$

The $P_{n_i}^{(m)}$ represent associated Legendre functions of degree n_i and order m. We choose $n_1 = 2n + m - 2$ and $n_2 = 2n + m - 1$ thereby incorporating a particular equatorial symmetry into our expansions. The symmetry chosen corresponds to that intrinsic to the spinover mode and has the property that

$$\begin{aligned} u_r(r,\pi-\theta,\phi) &= -u_r(r,\theta,\phi) \\ u_\theta(r,\pi-\theta,\phi) &= u_\theta(r,\theta,\phi) \\ u_\phi(r,\pi-\theta,\phi) &= -u_\phi(r,\theta,\phi) \end{aligned} \tag{2.5}$$

There is nothing apparently special about this symmetry and one could carry out the whole analysis with the opposite symmetry for completeness. However, it should be noted that the chosen symmetry is opposite to that which allows columnar roll formation, a commonly favoured symmetry in rotating fluid systems. We therefore cannot be certain that the other class of modes would behave similarly, however, we can see no reason why the results that we report here should be affected by a different equatorial symmetry. One should also note that we have written the complex frequency ω as the sum of two parts, ω_0 and $\tilde{\omega}$. This is to facilitate the use of an inverse iteration procedure which will be detailed shortly.

With these expansions, the r-components of $\nabla\times$(2.1a) and $\nabla\times\nabla\times$(2.1a) become

$$\begin{aligned}
&\sum_{n=1}^{N}\left[n_1(n_1+1)i\omega_0 - 2im - En_1(n_1+1)L_{n_1}\right]\frac{e_n}{r^2}P_{n_1}^{(m)}(\cos\theta) \\
&\quad + \sum_{n=1}^{N}\frac{2}{r^2}\left[\frac{n_2(n_2+1)}{r} - \frac{d}{dr}\right]f_n\sin\theta\frac{d}{d\theta}P_{n_2}^{(m)}(\cos\theta) \\
&\quad + \sum_{n=1}^{N}\frac{2}{r^2}n_2(n_2+1)\left[\frac{2}{r} - \frac{d}{dr}\right]f_n\cos\theta\,P_{n_2}^{(m)}(\cos\theta) \\
&= -\tilde{\omega}\sum_{n=1}^{N}n_1(n_1+1)i\frac{e_n}{r^2}P_{n_1}^{(m)}(\cos\theta)
\end{aligned} \tag{2.6a}$$

$$\begin{aligned}
&\sum_{n=1}^{N}\left[n_2(n_2+1)i\omega_0 - 2im - En_2(n_2+1)L_{n_2}\right]L_{n_2}\frac{f_n}{r^2}P_{n_2}^{(m)}(\cos\theta) \\
&\quad - \sum_{n=1}^{N}\frac{2}{r^2}\left[\frac{n_1(n_1+1)}{r} - \frac{d}{dr}\right]e_n\sin\theta\frac{d}{d\theta}P_{n_1}^{(m)}(\cos\theta) \\
&\quad - \sum_{n=1}^{N}\frac{2}{r^2}n_1(n_1+1)\left[\frac{2}{r} - \frac{d}{dr}\right]e_n\cos\theta\,P_{n_1}^{(m)}(\cos\theta) \\
&= -\tilde{\omega}\sum_{n=1}^{N}n_2(n_2+1)iL_{n_2}\frac{f_n}{r^2}P_{n_2}^{(m)}(\cos\theta)
\end{aligned} \tag{2.6b}$$

where

$$L_{n_i} = \frac{1}{r^2}\frac{d^2}{dr^2}r^2 - \frac{n_i(n_i+1)}{r^2} \tag{2.7}$$

The associated boundary conditions (2.2) then become

$$f_n = \frac{d}{dr}f_n = e_n = 0 \tag{2.8a}$$

for no-slip, or

$$f_n = \frac{d}{dr}\left(\frac{1}{r^2}\frac{d}{dr}f_n\right) = \frac{d}{dr}\left(\frac{1}{r^2}e_n\right) = 0 \tag{2.8b}$$

for stress-free. Using the appropriate relations (see Appendix A) one finds that e_n couples to f_n and f_{n-1} and that f_n couples to e_n and e_{n+1}. It is obvious that the azimuthal modes do not couple and so we can choose a value of m to study from

the outset. For any particular value of m we expect to see a spectrum of modes with frequencies lying between -2 and 2 as in the corresponding inviscid analysis. Of course, since we have retained viscosity, each mode in the spectrum will have its own particular decay rate so that the spectrum is two dimensional in ω space.

One can then arrange eq(2.6) with either eq(2.8a) or eq(2.8b) to form a complex matrix eigenvalue problem of the form

$$\mathbf{A}\mathbf{v} = \tilde{\omega}\mathbf{B}\mathbf{v} \tag{2.9}$$

Here $\mathbf{A}$ is a block tri-diagonal matrix and $\mathbf{B}$ is a block diagonal matrix with the number of blocks increasing with the angular truncation N and the size of each block with the radial truncation M (details can be found in Appendix A). As the Ekman number, E, is lowered, we expect the shear layers to become thinner. This will require increasingly high truncation in r and θ to resolve the increasingly fine structures which appear. We were able to obtain approximately 1 Gbyte of memory which allowed us to achieve truncations as high as $N = 141, M = 172$. This proved sufficient to resolve the shear layers at values of E as low as $10^{-6.5}$.

System (2.9) is solved using an inverse iteration procedure which involves supplying a guess, ω_0 for the frequency. The algorithm then converges to the frequency $\omega = \omega_0 + \tilde{\omega}$ closest to the guess by producing a correction $\tilde{\omega}$ at each iterative stage. Since the decay rates are small, convergence was usually quite fast using only a purely real guess for the frequency. Even at the highest truncations the inversion of $\mathbf{A}$ usually took $\sim$10 CPU minutes at most with each subsequent iteration stage taking about $\sim$1 CPU minute. The limiting factor in the calculation was the amount of available memory. With this procedure one can then find any number of modes in a relatively short time.

At each iteration the eigenvector $\mathbf{v}$, which contains the structure of the mode, is also updated. Since the problem has been linearised the complex eigenvector has both an arbitrary amplitude and an arbitrary phase. Before we can compare any

two modes we need to define some sort of consistent method of normalisation. The approach adopted in Hollerbach & Kerswell (1995) for the spinover mode focussed on the angular momentum of the solution and allowed amplitude and phase normalisation in one condition. This was convenient since the spinover mode consists mainly of a solid body rotation which could then be subtracted out, allowing one to focus on the small viscous correction. In general though, it is difficult to see how one could extend this technique to the other modes in the spectrum. In this light we have decided to normalise our solutions in a two-stage process. Firstly, the amplitude, including that of the spinover mode, is normalised by setting the kinetic energy to one. The phase is normalised by focusing on the meridional section for which there is no net flux of fluid ie.

$$\int_0^{\pi/2} \int_{r_i}^{r_0} u_\phi r \, dr d\theta = 0 \tag{2.10}$$

Of course, this condition has no particular significance attached to it but it does at least allow us to compare modes in a consistent manner.

The code was tested by reproducing results by previous authors. Firstly, the spherical shell spinover results from Hollerbach & Kerswell (1995) for no-slip boundary conditions were verified. In particular we reproduced the frequencies in Table 2. and the plots in Figure 3. of their paper. This was not surprising, since the code had been adapted from the original Hollerbach & Kerswell code. Secondly, the frequencies in Table 1. of Rieutord (1995) were reproduced. This confirmed that we had properly extended the original code to azimuthal wavenumbers other than 1 and to frequencies other than 1.

2.2 Spectrum analysis

Before testing the effect of changes in boundary condition on internal shear layers we must first establish what modes we will look at. The spinover mode is a definite

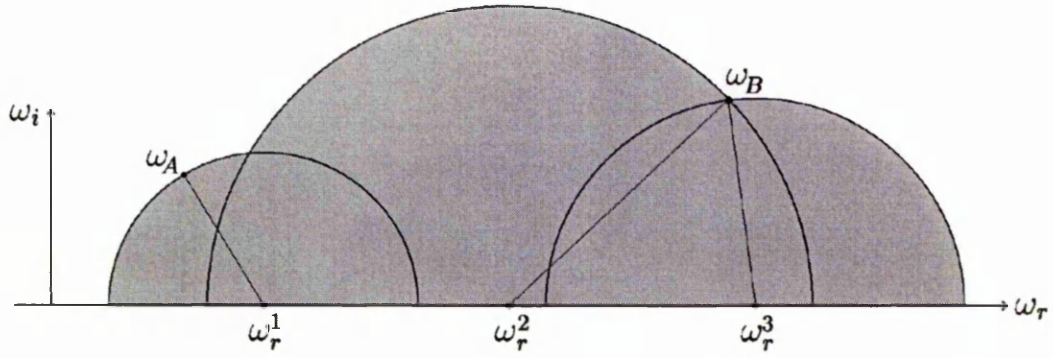

Figure 2.1: Mapping out ω space for low decay rates. The guess ω_r^1 converges to ω_A, which therefore negates the possibility of a mode existing within the shaded semicircle. Similarly, ω_r^2 and ω_r^3 both converge to ω_B, completing the mapping of modes having the lowest decay rates.

candidate and corresponds to an $m = 1$ mode with frequency close to 1. We would like to examine modes with other frequencies though, and also of differing wavenumber. To find all the modes in the spectrum for any given m would require searching a 2-D parameter space in both frequency and decay rate. To simplify matters we searched only for the modes with lowest decay rate. By this, we mean that the guess for our inverse iteration procedure was always purely real allowing us to search the 1-D space of frequencies. Since the iteration procedure converges to the complex frequency closest to the guess (ie. with the smallest $|\tilde{\omega}|$) we then map out a small section of the 2-D parameter space as shown in Figure 2.1.

This technique was easily automated with the frequency stepped from -2 to 2 in steps of 0.025 and at each step the iteration process was continued until convergence was better than 99.99999%. Spectrums for $m = 0, 1$ and 2 were obtained at a fairly moderate Ekman number of 10^{-5} and were carried out with no-slip boundary conditions on both boundaries. The radius ratio of our shell was fixed at 1/3. Of course, for $m = 0$ the modes in the half interval $\omega \in [0, 2]$ are the only unique modes since eq(2.6) is invariant under $\omega_r \to -\omega_r$. The spectrums were found to be fairly densely packed with the 160 initial guesses on the interval $\omega \in [-2, 2]$ returning, on average,

120 different modes. The typical spacing between modes in terms of frequency was then $1/30 = 0.033$ and the decay rates varied between about $0.01 - 0.03$.

This shows that there is a large number of modes available to choose from. If one picks a mode at random out of the spectrum and looks at its structure then one will always find shear layers. Recall from eq(1.10) that the orientation of the layers is given by

$$\varphi = \sin^{-1}\left(\frac{\omega_r}{2}\right) \tag{2.11}$$

For the spinover mode, $\varphi = 30^o$, which leads to a simple, closed reflection pattern. However, for a randomly selected mode, the frequency will be such that φ no longer necessarily leads to a closed pattern. We examined such modes and found the plots to contain multiple reflections which haphazardly crossed and recrossed over each other. This has the result that the shear layers become less distinct entities making it difficult to focus on any one in particular.

This suggests that we should focus attention on only those modes having clear reflection patterns. This will, in general, be the case if the pattern is closed. Since eq(2.11) is independent of m we could look for modes having $\omega_r = 1$, or indeed $\omega_r = -1$ as well. All of these should produce shear layer patterns similar to that of the spinover mode. However, we can find yet more modes with closed patterns by noting that any two modes with frequencies satisfying $\omega_1^2 + \omega_2^2 = 4$ will have similar patterns, the two being related by a simple reflection through the line $\theta = \pi/4$. Since we know that $\omega_r = \pm 1$ yield a closed pattern, we can say the same for $\omega_r = \pm\sqrt{3}$. The other obvious possibility is the rectangular pattern obtained when $\varphi = 45^o$ ie. $\omega_r = \pm\sqrt{2}$.

Since the spectrum is so densely packed, we can usually find a good approximation to the frequency that we want. Of course, we could, in principle, find a mode arbitrarily close to any desired value of ω_r by scanning through the entire range of decay rates but it turns out to be sufficient to examine only those with the smallest decay rates. For

the case of $\omega_r \sim \pm\sqrt{2}$ we find that the pattern is not the expected rectangular closed shape. The shear layers are inclined at angles very close to 45^o but there are multiple parallel layers throughout the interior. Perhaps the rectangular pattern is extremely unstable to the small changes in the shear layer orientation brought about by the discrete nature of our spectrum. By our stated criterion, these modes are therefore no use to us and will not be considered any further here.

Of the two remaining sets of patterns that we examined we felt that the shear layers associated with the frequences $\pm\sqrt{3}$ were the clearest. These are the modes we will study in the following section, to determine whether the stark contrast between different boundary condition configurations which exists for the spinover mode can exist for other more general modes. It should be noted that we have checked all the results reported in the next section are valid for the frequencies we have discounted here.

2.3 Results

Before presenting the results, we shall describe the terminology we shall use to classify the different boundary condition configurations. Table 2.1 lists the four different combinations of inner and outer boundary conditions as set-ups A through D. For simplicity, we will refer to a particular combination via the appropriate letter throughout the rest of this Chapter. Since we know that the choice of boundary conditions has

Set-up	Inner	Outer
A	No-slip	No-slip
B	Stress-free	Stress-free
C	No-slip	Stress-free
D	Stress-free	No-slip

Table 2.1: The four possible combinations of boundary conditions.

an enormous influence on the spinover mode we shall begin by examining this mode first. Figure 2.2 shows the four different set-ups for this mode at $E = 10^{-6}$. Plot (A)

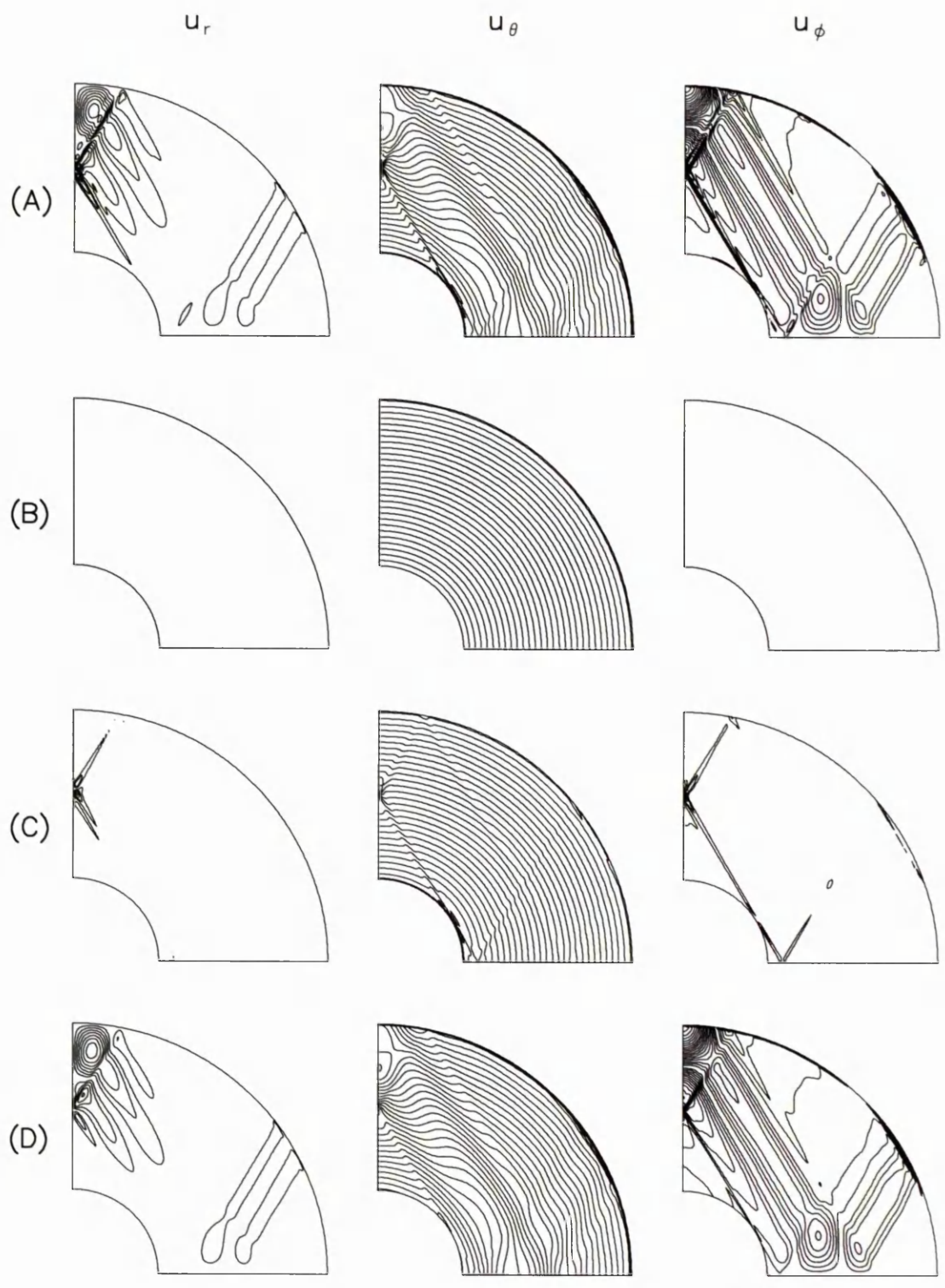

Figure 2.2: Contour plots of the spinover mode at $E = 10^{-6}$. Contour intervals are 0.010 for both u_r and u_θ and 0.025 for u_ϕ.

shows a reasonably clear pattern of internal shear layers, in particular it is obvious that the layer spawned tangentially from the inner core boundary and its associated reflections are dominant. While this figure may look dissimilar to the corresponding figure of Hollerbach & Kerswell, one must bear in mind that we have not subtracted out the solid body rotation. We are also choosing to show all three components of the flow at the same no-flux slice, whereas Hollerbach & Kerswell plotted u_ϕ 90^o out of phase with the other two components. Plot (B) shows us exactly what we would expect. The solid body rotation that satisfies eq(2.1a) also satisfies stress free boundary conditions on each boundary and so here we see the analytic form given in eq(1.8). There are no contours in the u_ϕ component because we are plotting at the slice where u_ϕ has no flux. Looking at a different slice reveals the predicted z-dependent structure ie. the $r\cos\theta$ factor from u_ϕ in eq(1.8), and reinforces our belief that our code works for both types of boundary conditions.

The stark contrast between plots (A) and (B) then raises the question as to which of the remaining two set-ups will look more like (A), and which more like (B). Noting again how the pattern in (A) seems to be triggered by the inner boundary, one might expect that removing the no-slip condition from the outer boundary would make little difference but removing it from the inner to make a substantial difference. If we look at plot (C) we can see that our beliefs are not correct since there is a dramatic reduction in shear layer strength, almost to the point of recovering a pure solid body rotation. Even more surprising is the result shown in plot (D) which is implying that the no-slip condition on the inner boundary is playing a very minor role in determining the overall strength of the pattern. A first reaction would be to automatically assume the code was wired up the wrong way and that plots (C) and (D) are actually the wrong way around. This is definitely not the case since one can just make out the Ekman layers on the boundaries where the no-slip condition is being applied.

Having illustrated the basic question we wish to explore, we now turn our attention

to various other modes. As discussed in the previous section the modes with the clearest shear layer patterns are those with $\omega_r \sim \pm\sqrt{3}$. Table 2.2 lists the frequencies for the $m = 1$ mode with $\omega_r \sim +\sqrt{3}$ at two values of the Ekman number. Although these are good approximations (to within about one percent) to the ideal frequency of 1.732, we must bear in mind that at any finite value of E, the finite thickness of the shear layers can easily account for any slight deviation from the exactly closed pattern that the frequency discrepancy might cause. The frequencies in Table 2.2 suggest that we may have a similar trend to the results for the spinover mode. The frequency does not change much over the four set-ups but, nevertheless, there is still a slight correlation between (A) and (D) as there is between (B) and (C). This is much more pronounced in the corresponding decay rates where there is a whole order of magnitude difference between the two pairs of cases. Not surprisingly there is a larger decay rate for case (A) since we have thicker Ekman boundary layers than in (B) due to the no-slip condition. Of course, the increased dissipation in case (D) could then simply be attributed to the longer outer boundary still having a no-slip condition and therefore dominating the dissipation.

	$E = 10^{-5.5}$	$E = 10^{-6.5}$
A	(1.7139,0.0055)	(1.7134,0.0018)
B	(1.7130,0.0007)	(1.7131,0.0003)
C	(1.7131,0.0007)	(1.7132,0.0003)
D	(1.7138,0.0054)	(1.7134,0.0018)

Table 2.2: Complex frequencies ω_r for the least damped mode nearest $+\sqrt{3}$ for $m = 1$.

The structure of this mode is plotted in Figure 2.3 at $E = 10^{-5.5}$ to enable a better comparison of the interior behaviour as we change the boundary conditions. The first point to note is the sharpness of the shear layer pattern despite our frequency differing slightly from $\sqrt{3}$. The pattern is as expected, a reflection of the spinover pattern about a line at $\theta = \pi/4$ with critical latitudes now at $\varphi = \pi/3$. The pattern is much more pronounced than that of the spinover mode because we are not dominated by a solid

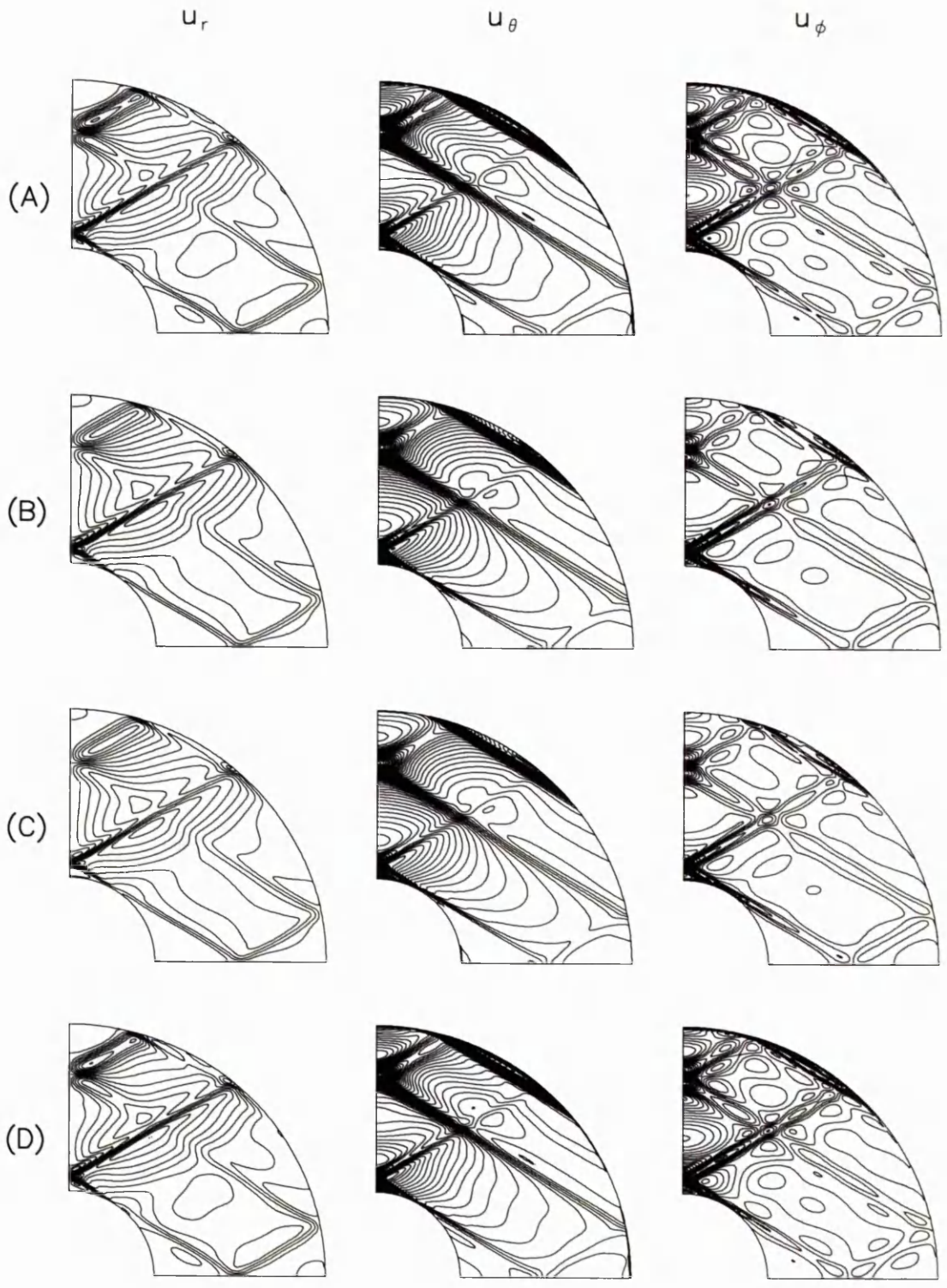

Figure 2.3: Contour plots of the $m = 1$ mode with $\omega_r \sim +\sqrt{3}$ at $E = 10^{-5.5}$. The contour interval is 0.3 throughout.

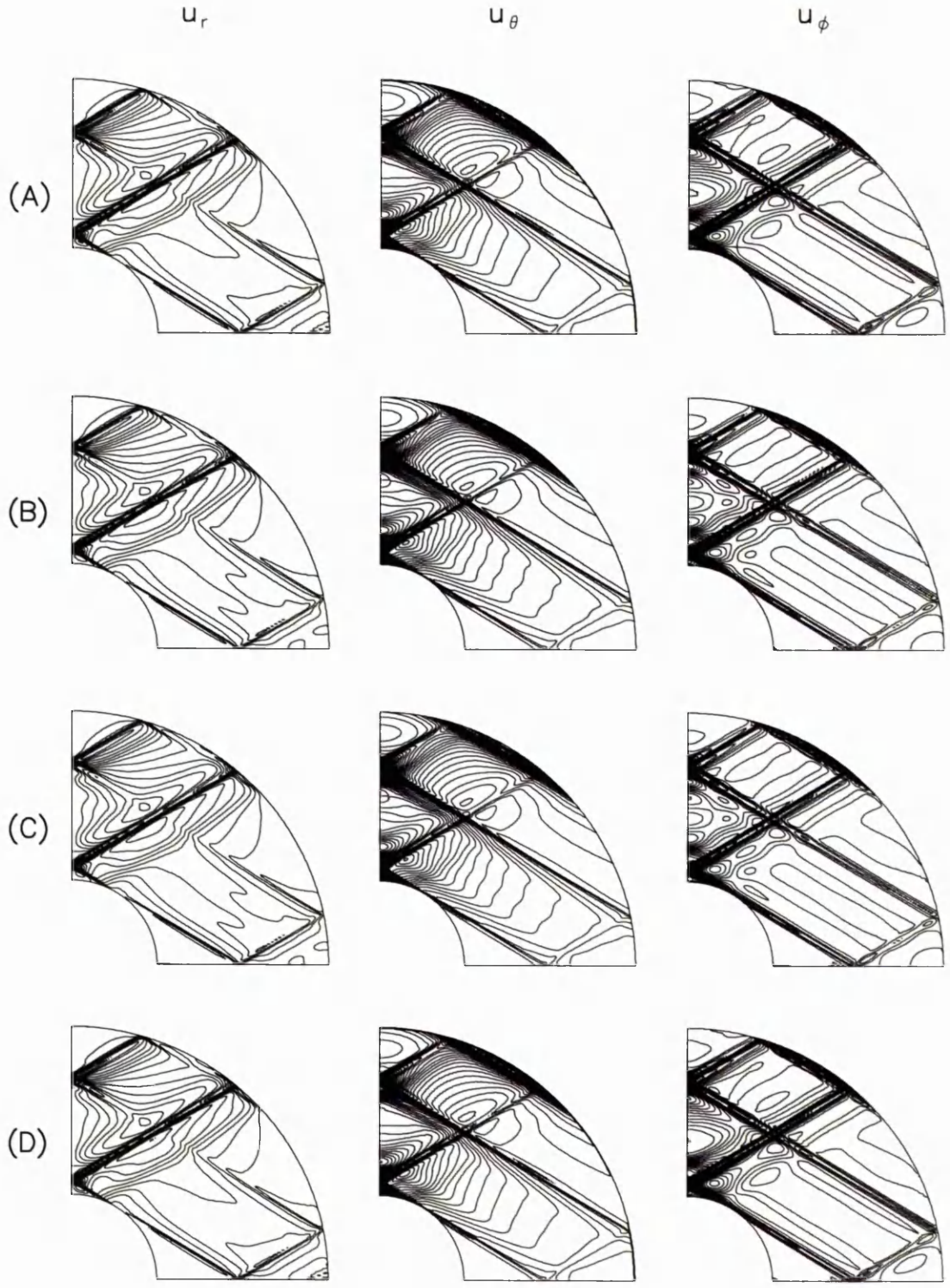

Figure 2.4: As in Figure 2.3, but at $E = 10^{-6.5}$

body rotation. There is certainly some background structure but the shear layers are a much more dominant part of the overall solution.

At first glance there is really not much difference between all four plots, certainly nothing as extravagant as for the spinover mode. All the shear layers seem to be of equal strength, which, of course, is still a surprising result given that we would at least expect the totally stress-free case (B) to show some signs of weakening. A closer inspection does reveal some slight differences though, most noticeable in the polar regions of the plots of u_r and u_ϕ. These differences do imply a weakening of the shear layers in cases (B) and (C) in this localised region but there is no indication that the shear layer coming tangentially off the inner core boundary has weakened in either of these two cases. There is also only a small change in the background flow, again in (B) and (C), most noticeable in the u_θ plot and near the rotation axis in u_ϕ.

The plots of Figure 2.4 show the same mode but at the reduced Ekman number of $E = 10^{-6.5}$. The first thing to notice is that the existing layers have thinned as one would expect. Also, shear layers have appeared in places where the pattern was previously weak eg. u_ϕ which gives us more to compare between plots. Surprisingly, it seems as if there is even less of a difference than there was before, with both shear layers and background flow showing only tiny changes. If this trend continues with decreasing E then one would end up with four identical solutions in the asymptotic limit as $E \to 0$.

As a second example we look at another $m = 1$ mode, this time with $\omega_r \sim -\sqrt{3}$. The frequencies and decay rates are shown in Table 2.3, again for the same two values of E. The frequency, which is a much better approximation to $\sqrt{3}$ than before, shows a larger difference between pairs {(B),(C)} and {(A),(D)} whereas the decay rates show a smaller difference. The corresponding plots for this mode are shown in Figures 2.5 and 2.6. At the higher value of E there is now a much more obvious difference between the plots. It is immediately clear that we are following the same behaviour as

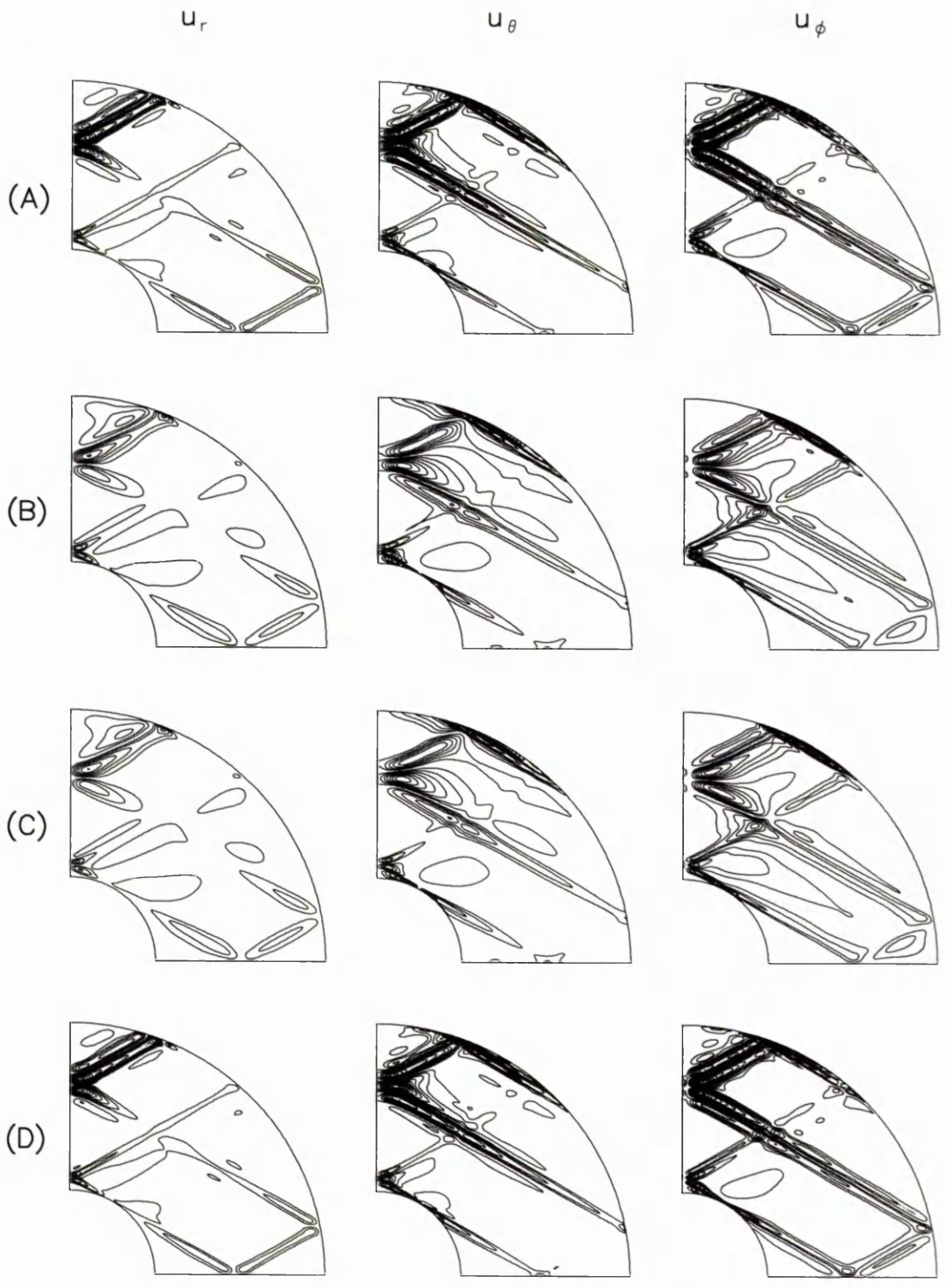

Figure 2.5: Contour plots of the $m = 1$ mode with $\omega_r \sim -\sqrt{3}$ at $E = 10^{-5.5}$. The contour interval is 0.3 throughout.

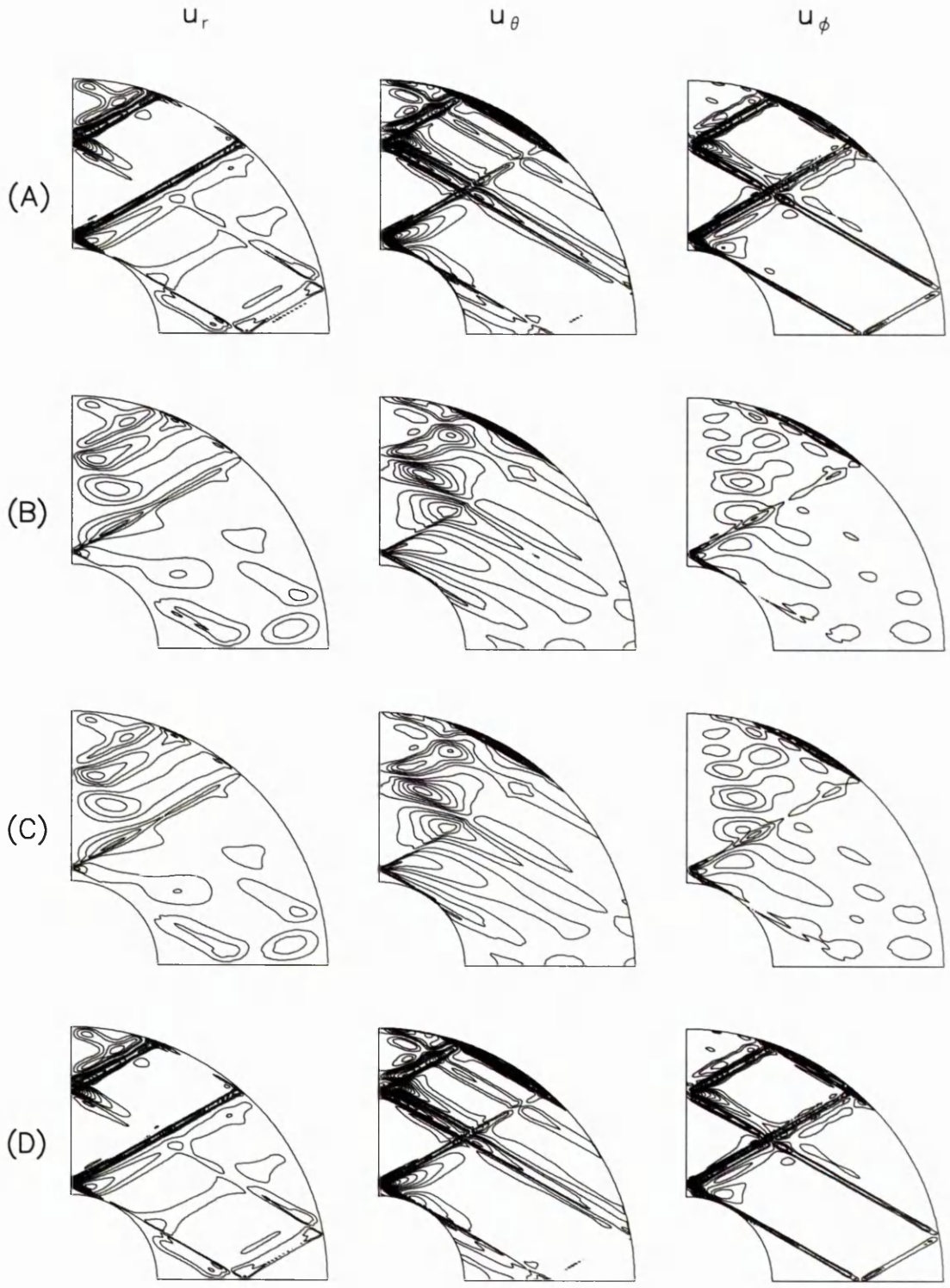

Figure 2.6: As in Figure 2.5, but at $E = 10^{-6.5}$

the spinover mode, with the outer boundary condition apparently governing the shear layer strength. For this mode the behaviour is amplified at smaller E. Not only are the layers thinner but they are very hard to make out at all in cases (B) and (C). It is therefore possible that for one of the two $m = 1$ modes we have considered here, or indeed both, the asymptotic regime has not yet been reached.

	$E = 10^{-5.5}$	$E = 10^{-6.5}$
A	(-1.7316,0.0140)	(-1,7300,0.0037)
B	(-1.7377,0.0079)	(-1.7401,0.0012)
C	(-1.7376,0.0080)	(-1.7401,0.0012)
D	(-1.7314,0.0138)	(-1.7300,0.0036)

Table 2.3: Complex frequencies ω, for the least damped mode nearest $\omega_r = -\sqrt{3}$ for $m = 1$.

To generalise further we now consider modes with an azimuthal wavenumber of 2. The first is the mode with $\omega_r = +\sqrt{3}$ and is shown in Figures 2.7 and 2.8 for cases (A) and (C). We only show these two cases because they are identical to the plots for cases (D) and (B) respectively. The difference is again clear suggesting that this phenomenon is not restricted to a particular azimuthal wavenumber. For this mode, however, the difference between (A) and (C) does not seem to be affected when the Ekman number is lowered.

Lastly we show the $m = 2$ mode with $\omega_r \sim -\sqrt{3}$ in Figures 2.9 and 2.10. At $E = 10^{-5.5}$ there is little difference between the plots, although the shear layers in (A) are slightly stronger than in (C). This mode shows the same behaviour as the $m = 1$ mode with the corresponding frequency when E is lowered. If one looks at u_r and u_ϕ, there is very little shear left at all in case (C) whereas the pattern is still almost completely closed in (A).

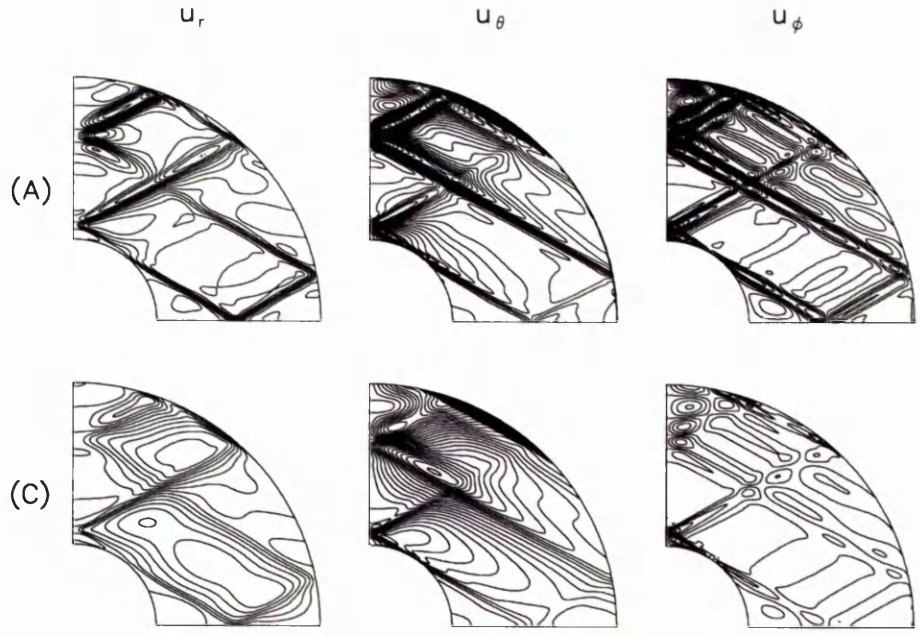

Figure 2.7: Contour plots of the $m = 2$ mode with $\omega_r \sim +\sqrt{3}$ at $E = 10^{-5.5}$. The contour interval is 0.1 throughout.

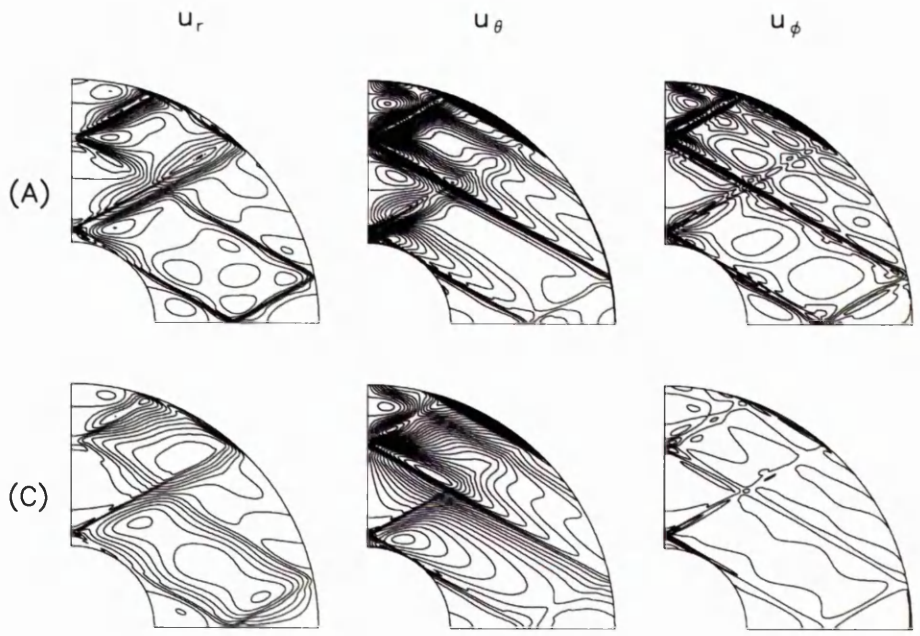

Figure 2.8: As in Figure 2.7, but at $E = 10^{-6.5}$

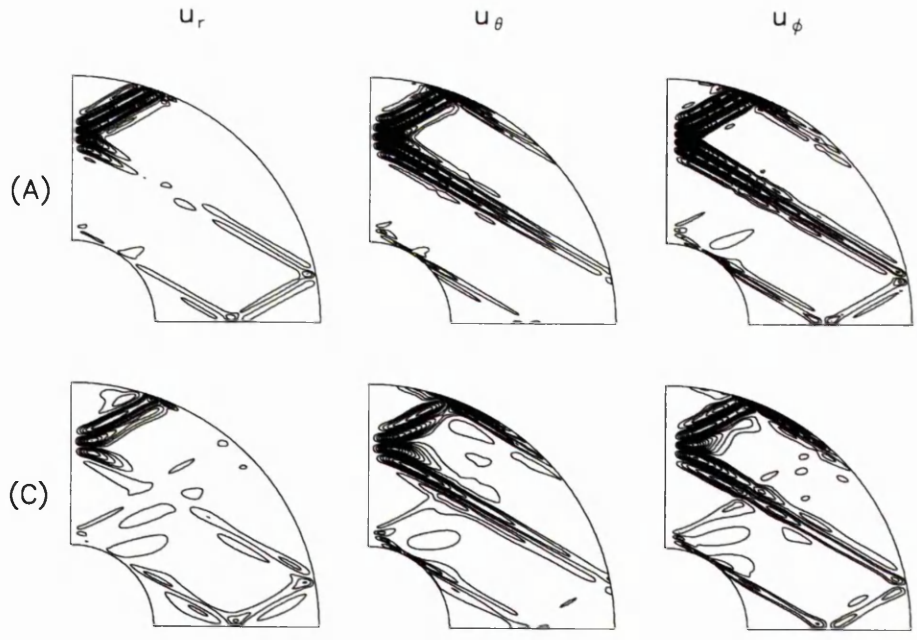

Figure 2.9: Contour plots of the $m = 2$ mode with $\omega_r \sim -\sqrt{3}$ at $E = 10^{-5.5}$. The contour interval is 0.3 throughout.

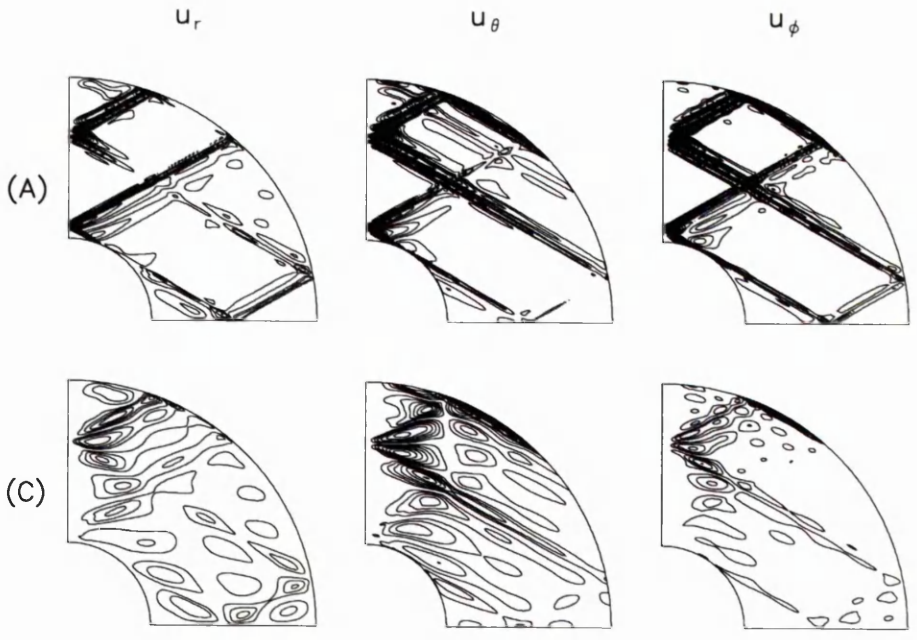

Figure 2.10: As in Figure 2.9, but at $E = 10^{-6.5}$

2.4 Mode verification

In light of the counter-intuitive results we have obtained it is important that we know we are comparing the proper quantities. We have consistently normalised both the phase and the amplitude of solutions but there still remains a slight doubt over the identity of each mode. After all, if one looks at the frequencies and decay rates quoted in Tables 2.2 and 2.3 then it is conceivable that we have inadvertently skipped to a different mode. Our inverse iteration technique will always converge to the mode with complex frequency closest to our guess, and so, when the boundary conditions are changed, it is possible the spectrum changes in such a way that the closest mode is no longer the one we were originally looking at. This is also an issue when the value of the Ekman number is lowered, since we might expect the decay rate to be much more affected in this case.

A first check is to notice that a typical change in frequency is usually about one order of magnitude smaller than the typical intermode spacing obtained from the spectrum analysis. Some of the changes are bigger than this, though, and given that we also have the decay rate varying, it is desirable to have a more rigorous test. The simplest way to verify that mode skipping has not occurred when the Ekman number changes is to simply increment E in small steps. We did this for all the modes considered here and are absolutely certain that no skipping occurred. To illustrate this, Figure 2.11 shows the path taken in the complex frequency plane as E is lowered from $10^{-5.5}$ to $10^{-6.5}$ for the $m = 2$ mode with $\omega \sim +\sqrt{3}$.

From a physical standpoint, it is not so obvious how one should go about confirming that mode skipping is absent when the boundary conditions are changed. Fortunately this is not a problem from a numerical point of view. All we need to do is continuously transform one boundary condition into the other, which can be achieved by simply

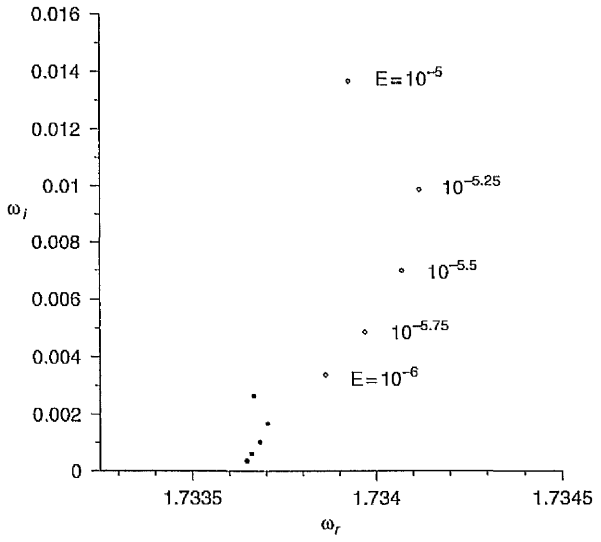

Figure 2.11: Variation in complex frequency, ω, as E is changed for the $m = 2$ mode with $\omega \sim +\sqrt{3}$. Diamonds represent set-up (A) and dots are set-up (B). The Ekman number for (B) decreases in exactly the same fashion as marked for (A).

taking a linear combination of the two as shown below.

$$\alpha \frac{df_n}{dr} + (\alpha - 1)\frac{d}{dr}\left(\frac{1}{r^2}\frac{df_n}{dr}\right) = 0 \tag{2.12a}$$

$$\alpha e_n + (\alpha - 1)\frac{d}{dr}\left(\frac{e_n}{r^2}\right) = 0 \tag{2.12b}$$

The parameter α controls the deformation process. When $\alpha = 1$ we have a no-slip condition, and when $\alpha = 0$ we have stress free. We only have two equations here because the no-normal flow condition $f_n = 0$ is common to both cases. The results of letting α run from 0 to 1 on the outer boundary are shown in Figure 2.12 for the $m = 1$ mode at $\omega \sim +\sqrt{3}$. A smooth continuous curve is transcribed through the complex frequency plane confirming that we are tracking the same mode. It is not surprising that the bulk of the curve is traversed when $\alpha \in [0.75, 1]$ since the no-slip condition imposes a much harsher restriction on the flow than the stress free condition. As with the Ekman number, all modes were tested using this technique and no mode skipping was found to occur.

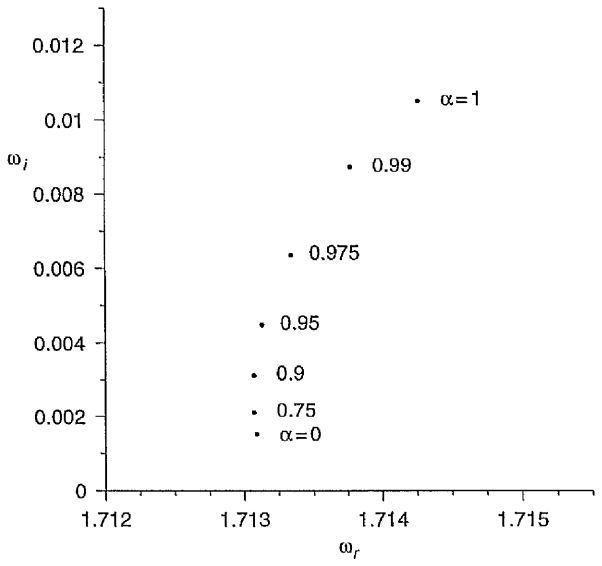

Figure 2.12: Variation in complex frequency, ω, as α is changed for the $m = 1$ mode with $\omega \sim +\sqrt{3}$. The outer boundary condition is the one under transformation, the inner held fixed at no-slip ie. (A) to (C). The Ekman number is 10^{-5}.

2.5 Conclusions

In this study we have set out to examine the internal shear layers associated with inertial oscillations in spherical shells. By focusing attention on modes having particularly simple closed shear layer patterns, we have investigated the influence of boundary conditions on these shear layers. We discovered, first of all, that the overall shear layer pattern is determined entirely by the presence of the inner boundary, with the shear layers occurring on the particular characteristic tangent to the inner boundary. The precise boundary conditions imposed on the inner boundary, however, appear to have no effect whatsoever, neither on the overall shear layer pattern nor even on the more detailed structure. In contrast, the boundary conditions imposed on the outer boundary can clearly influence the detailed structure (although not the overall pattern). The general trend appears to be that imposing no-slip boundary conditions enhances the shear layers somewhat compared to stress free. However, this result becomes considerably more complicated when one also takes into account the dependence on E.

We found that for one of our modes the difference decreased with decreasing E, for one it remained unchanged, and for two modes it actually increased with decreasing E. It is not clear that this increasing difference with decreasing E would necessarily continue indefinitely, but that merely highlights the difficulty outlined by Rieutord & Valdettaro, of never being absolutely certain that one has reached the true asymptotic limit in one's numerical solution.

Having obtained this result, that it is only the boundary conditions on the outer boundary which have any effect at all, one would naturally like to know why that should be so. We must admit that we do not really know. However, one point that is worth noting as being possibly related is that changing the outer boundary conditions has a considerably greater effect on the frequency than changing the inner ones. In particular, having no-slip boundary conditions always results in a higher decay rate. By itself that is, of course, hardly surprising, since it is well known that having no-slip boundary conditions will enhance dissipation in the Ekman layer. So perhaps the explanation is simply that because the outer Ekman layer has $(r_o/r_i)^2 = 9$ times more area than the inner one, switching boundary conditions at the outer boundary naturally has a correspondingly greater effect on the dissipation, and hence on ω_i, and indirectly perhaps on ω_r. It is difficult to believe that these very slight frequency differences between the pairs {(A),(D)} and {(B),(C)} could by themselves be sufficient to cause the observed differences in the shear layer structure, but we cannot be certain. Another possibility would be that the difference between having a convex outer boundary versus a concave inner one is once again crucially important, although again it is difficult to see why that would make the difference. One possibility for testing this hypothesis would be to solve the corresponding problem in cones or truncated cones, where it is known (Henderson & Aldridge (1992)) that similar shear layers exist, but without an inner boundary.

The general conclusion of this work would seem to be that we still do not fully

understand why these internal shear layers are needed in the solutions at all, and what ultimately determines their detailed structure. The answers to these questions will presumably only emerge from a complete asymptotic theory, which is, however, a formidable undertaking.

Chapter 3

Magnetic stability: the α^2 dynamo

We now wish to extend our purely hydrodynamic studies to include the effect of magnetic fields. This is a more realistic description of the Earth's core than in the previous chapter since the molten iron which comprises it is an electrical conductor. Motions in the core can reinforce existing magnetic field and ultimately drive the geodynamo, provided a power source is supplied to overcome Ohmic and viscous dissipation. That such a mechanism is necessary for the Earth can be easily demonstrated by noting that the magnetic diffusion time for the core is given by

$$\tau = \mathcal{L}^2/\eta \tag{3.1}$$

where $\mathcal{L}$ is a typical lengthscale of magnetic field variation and η is the magnetic diffusivity of the core. Taking $\mathcal{L}$ to be the gap width (ie. the difference between inner and outer radii = 2260km) and $\eta = 1m^2s^{-1}$ (Secco & Schloessin (1989)) we obtain $\tau = 1.62 \times 10^5$ years. This is much shorter than the paleomagnetic record which dates as far back as 3.5Ga and suggests that the geomagnetic field has been and still is being maintained by some sort of dynamo process. Of course there is still the possibility that the iron in the core is ferromagnetic but core temperatures ($\sim$4000K) greatly exceed the Curie point of iron (1043K) and so this too can be discounted.

In the introduction, three possible power sources were described for the geodynamo: compositional and thermal buoyancy and precession. Each one has its own supporters

throughout the scientific community but most agree the most likely source of driving would come from a combination of all three. Incorporating either compositional or thermal buoyancy alone into the equations is not a difficult task but would involve solving extra equations and introducing extra terms into the existing equations. Since the governing equations are CPU intensive at only moderate parameter values, the addition of extra work and extra parameters can severely limit the amount of results one could obtain. It is, therefore, presently rare to find a model which includes both forms of buoyancy. In the case of precession, it is a much more difficult effect to model due to the spheroidal geometry.

3.1 Basic Mean-Field Theory

In an effort to make our model more realistic than the diffusionless, imposed field approach, adopted by Hutcheson & Fearn, and yet still computationally tractable, we have adopted an alpha effect for our forcing. Alpha effects are at the heart of what is known as mean field theory, first developed by Braginsky (1964) and Steenbeck & Krause (1966). The idea is that small scale, turbulent, nonaxisymmetric flows can lead to field regeneration, and that ultimately this process can be modelled by a single parameter, α. This process gives an alternative mechanism to conventional forcings through which the axisymmetric parts of the field may be maintained. To see why this is so, let us write the field and flow as the sum of their axisymmetric parts, denoted by overbars, and their nonaxisymmetric parts, denoted with dashes, such that

$$\mathbf{B} = \overline{\mathbf{B}} + \mathbf{B}' \quad , \quad \mathbf{u} = \overline{\mathbf{u}} + \mathbf{u}' \tag{3.2}$$

The mean, or azimuthally averaged, induction equation becomes,

$$\frac{\partial \overline{\mathbf{B}}}{\partial t} = \nabla^2 \overline{\mathbf{B}} + \nabla \times (\overline{\mathbf{u}} \times \overline{\mathbf{B}}) + \nabla \times (\overline{\mathbf{u}' \times \mathbf{B}'}) \tag{3.3}$$

From this we see that the axisymmetric field, $\overline{\mathbf{B}}$, can be generated through the interaction of non-axisymmetric field and flow in addition to purely axisymmetric interactions.

Indeed this is essential if we are to circumvent Cowling's anti-dynamo theorem which states that it is impossible to sustain a purely axisymmetric field through dynamo action. If there was no nonaxisymmetric field then there could be no axisymmetric field.

The aim of mean field theory is to recast the nonaxisymmetric interactions of small scale turbulence into a simpler form by applying statistical techniques to the turbulent flow. One assumption made is that the turbulence is not mirror symmetric ie. not symmetric about the reflection $s \to -s$, where s is the cylindrical radius. This is justified by the presence of the Coriolis force in the momentum equation, which will ensure that fluid motions lack this mirror symmetry. With this, and other, assumptions, Steenbeck, Krause & Rädler (1966) showed that the induction equation (3.3) could be written as

$$\frac{\partial \overline{\mathbf{B}}}{\partial t} = \nabla^2 \overline{\mathbf{B}} + \nabla \times (\overline{\mathbf{u}} \times \overline{\mathbf{B}}) + \nabla \times (\alpha \overline{\mathbf{B}}) \tag{3.4}$$

where the scalar parameter α has been introduced.

Mean field theory does not determine the form of alpha, instead it must be prescribed. Clearly α is an axisymmetric quantity and so in general $\alpha = \alpha(r, \theta)$. Once again, appealing to the Coriolis force, and its equatorial symmetries, we can deduce that α must be equatorially antisymmetric. Apart from this symmetry we are free to choose whatever form for α that we deem appropriate.

To obtain a better understanding of the role that the alpha effect plays in driving the system it is convenient to use the axisymmetric decompositions for $\overline{\mathbf{u}}$ and $\overline{\mathbf{B}}$ given by

$$\overline{\mathbf{u}} = \nabla \times (\psi \hat{\mathbf{e}}_\phi) + v \hat{\mathbf{e}}_\phi \tag{3.5a}$$

$$\overline{\mathbf{B}} = \nabla \times (A \hat{\mathbf{e}}_\phi) + B \hat{\mathbf{e}}_\phi \tag{3.5b}$$

The ϕ component of the curl of eq(3.4) and the ϕ component of eq(3.4) become, respectively,

$$\frac{\partial A}{\partial t} = D^2 A + \alpha B + N(\psi, A) \tag{3.6a}$$

$$\frac{\partial B}{\partial t} = D^2 B + \hat{\mathbf{e}}_\phi \cdot \nabla \times [\alpha \nabla \times (A\hat{\mathbf{e}}_\phi)] + M(v, A) - M(B, \psi) \tag{3.6b}$$

where

$$D^2 = \nabla^2 - 1/s^2 \tag{3.7a}$$

$$N(X, Y) = \hat{\mathbf{e}}_\phi \cdot [\nabla \times (X\hat{\mathbf{e}}_\phi) \times \nabla \times (Y\hat{\mathbf{e}}_\phi)] \tag{3.7b}$$

$$M(X, Y) = \hat{\mathbf{e}}_\phi \cdot \nabla \times [X\hat{\mathbf{e}}_\phi \times \nabla \times (Y\hat{\mathbf{e}}_\phi)] \tag{3.7c}$$

We may now identify two key terms in eqs (3.6). The first is the αB term in eq(3.6a) which can give rise to amplification of poloidal field, A. The second is the $\hat{\mathbf{e}}_\phi . \nabla \times [\alpha \nabla \times (A\hat{\mathbf{e}}_\phi)]$ term in eq(3.6b) which conversely amplifies the toroidal field, B. The physical picture that explains the two processes can be thought of as small scale helical flows acting on the field. If the field is toroidal (B) then the flow would twist the field lines to produce poloidal field. In exactly the same way, poloidal field (A) can be twisted to produce toroidal field. Since both A and B are maintained by the alpha effect, this type of dynamo is known as the α^2 dynamo. For this particular kind of dynamo the toroidal and poloidal field strengths are usually comparable. It is worth noting that, in contrast to kinematic theories, where one prescribes a flow $\overline{\mathbf{u}}$, the field can be maintained entirely through the alpha effect. Of course one could still specify a flow but this will be dealt with in the next chapter when we discuss the $\alpha\omega$ dynamo.

3.2 Previous α^2 results.

The earliest work of any significance to study field generation through alpha effects was by Parker (1955). He introduced the idea of cyclonic turbulence and showed, using

a simple localised model, how the helicity associated with the flow could be used to regenerate magnetic field. However, the demonstration was for the case of poloidal field regeneration with large scale flows used to regenerate the toroidal field, thus actually falling under the category of $\alpha\omega$ dynamos, more of which will be discussed in the next chapter. The work of Steenbeck, Krause & Rädler (1966) gave a firmer mathematical foundation to the concept of α effects. Steenbeck & Krause (1966, 1969) studied examples of mean field dynamos which operated through the action of the α effect alone. These models were kinematic in nature meaning that the back reaction of the field on the large scale flow was ignored. This results in the simple linear system

$$\frac{\partial \mathbf{B}}{\partial t} = \nabla \times (\alpha \mathbf{B}) + \nabla^2 \mathbf{B} \tag{3.8}$$

The magnetic field was assumed to be axisymmetric thus reducing the already simplified problem to a purely 2-D calculation. An important point to note is that eq(3.8) permits solutions of $\mathbf{B}$ with dipole or quadrupole symmetry separately, provided α is antisymmetric with respect to the equatorial plane. When solving eq(3.8) one simply increases the amplitude of α until the linear growth rate becomes positive and dynamo action is then possible. If we take α to have the general form $\alpha_0 f(r, \theta)$ then the two parities can become unstable at different critical values, $\alpha_0 = \alpha_c$,

It is clearly important that a study of alpha effect dynamos should give qualitatively similar answers for different forms of α. If the solutions were strongly dependent on the form of α then little meaningful progress could be made since we arbitrarily prescribe the form of α. From studying a variety of forms for α, Steenbeck & Krause were able to deduce two general features of α^2 dynamos:

- The critical values, α_c, of the dipole and quadrupole parities were always close together.
- The eigenfunctions were steady ie. apart from their exponential growth there was no other time dependence in the form of an oscillatory component.

These results were confirmed by Roberts (1972) who studied the same forms of α but used different expansion functions in the numerical method. The explanation proposed appealed to the structure of the eigenfunctions which showed most activity in the polar to mid latitude regions. Since this configuration tends to maximise the separation of the current loops, the mutual inductance between the two hemispheres will be small and hence one could flip the sign of the field in one hemisphere with little overall effect on the solution as a whole.

It was recognised by Malkus & Proctor (1975) that the next step in the study of α^2 dynamos should be to discard the kinematic constraint and include a more realistic feedback in the system. The momentum equation was reintroduced giving a coupled nonlinear set of equations which allowed the field (and flow) to equilibrate at finite amplitude. In their analytic approach to the problem Malkus & Proctor were interested in the force balance in the momentum equation at equilibration and so began the search for Taylor states (for a discussion of Taylor states see the Introduction). This is an example of where mean field theory can come into its own. It allowed Malkus & Proctor to study the dynamics of the momentum equation without having to solve the full equations. The interaction of flow and field was of primary importance and the use of an alpha effect does not alter the essential physics of that part of the problem.

By ignoring inertia and searching for steady solutions they were able to identify both the viscous and inviscid regimes for small equilibrated field amplitudes. Unfortunately there was an error in the analysis for the inviscid regime, where, for the special case of constant α that they used, no steady solutions were permitted. Nevertheless they had shown that the field strength could be limited by the fluid back reaction and had not ruled out the possibility of an oscillatory inviscid solution. In a numerical approach shortly afterward, Proctor (1977), pointed out that the non-existence of steady solutions could be traced to α being independent of z, a fact which was proposed as

being unrealistic (recall that α should probably be antisymmetric about the equator due to the influence of the Coriolis force). Using an α with a $\cos\theta$ dependence Proctor time-stepped the equations (inertia was restored in the numerical approach) at different values of the Ekman number and the Rossby number. Although limited to fairly high parameter values, evidence of the progression to a Taylor state was visible.

This problem was revisited by Hollerbach & Ierley (1991) again using an α^2 model but restricted to fields of dipole parity. In order to prove that their equilibrated solutions were unambiguously in Taylor states they implemented a linear friction term instead of the usual Laplacian operator. This permitted values as low as 10^{-9} for E and showed that true Taylor states existed below $E \sim 10^{-6}$. The details of how the Taylor state was achieved depended on the exact choice of α. Two scenarios occurred, one where the evolution was smooth as α was increased and one where a finite amplitude jump occurred. The equilibrated inviscid solutions were steady, although at even higher values of α oscillatory inviscid states were found. Hollerbach (1991) extended this model to include both parities and investigated the question of parity selection. Although the dipole mode was favoured at the linear onset (α_c) there existed two solution branches in the inviscid regime, one dipolar and the other quadrupolar. Both set up large scale flows that stabilised the field to perturbations of the opposite parity and so the question of parity selection in the Taylor regime was left unresolved.

An alternative nonlinear feedback mechanism for mean field dynamos was first discussed by Stix (1972) in a one dimensional model and then by Jepps (1975) for an axisymmetric $\alpha\omega$ model. This mechanism relies on the large scale flow only indirectly and is concerned with the effect that both the large scale flow and field would have on the small scale turbulence. As one would expect, the turbulence would be affected by large scale fields and could possibly be weakened as the large scale field strengthened. Models incorporating this type of nonlinear feedback incorporate α effects that typically vary with the magnetic energy or field strength. A variety of these

"α- quenched" models have given equilibrated fields and can be found in Ivanova & Ruzmaikin (1977), Kleeorin & Ruzmaikin (1984) and Rädler (1984) amongst others. Just like mean field models themselves, α-quenchings can serve a useful purpose by allowing analysis of a simplified system. For example, Rädler & Wiedemann (1989) use α-quenching to study the stability of equilibrated axisymmetric and nonaxisymmetric solutions of an α^2 model to both axisymmetric and nonaxisymmetric perturbations, in the process revealing the dangers of restricting to purely axisymmetric studies. Their results showed that a pure parity axisymmetric state could be stable to perturbations of the opposite parity but not to nonaxisymmetric perturbations. It has also been pointed out by Brandenburg et al. (1989) that even at the onset of dynamo action the favoured solution may not be axisymmetric if the α effect is localised in a thin layer, as may be the case for the Sun. Although never obtaining nonaxisymmetric modes at onset they showed that only a weak differential rotation was required to make $m = 1$ the favoured mode.

A recent advancement in geophysical modelling has been the introduction of a finitely conducting inner core as opposed to an insulating one or indeed none at all. Electromagnetic torques may now act on the core and rotate it with respect to the mantle and so in the limit of vanishing viscosity an analogue of Taylor's constraint must apply. Again, the first study of the effect of this was via the use of an α^2 dynamo. Hollerbach & Jones (1993a) used the simple form $\alpha = \alpha_0 \cos\theta$ to examine how the field would adjust to the new constraint and found that this is achieved by minimisation of the Ohmic dissipation in the inner core.

It is this model which we shall in fact extend in this chapter, although with the emphasis on the magnetic stability of the fields produced rather than on seeking Taylor states. Reproduction of these results is the first aim of testing our numerical code of course.

3.3 Governing equations and numerical solution

The system we have chosen to study consists of an electrically conducting fluid contained in a spherical shell. The region exterior to the fluid is taken as an electrical insulator to model the Earth's mantle. Of course the mantle may, in fact, be weakly conducting but we shall ignore this fact in our present study as indeed most other models do as well. The region interior to the fluid is taken to be finitely conducting with the same electrical conductivity, σ ,as the fluid itself. In our numerical scheme it would be a simple matter to set the inner core conductivity to be different to that of the fluid but it is not of any interest to the current work. The energy source for our system is the work done by unresolved small scale turbulence which can manifest itself on large scales and be parameterised as the so-called "alpha effect". In this chapter this will be the only net source of energy in the system with the large scale flow, $\mathbf{u}$, being that induced by the large scale field, $\mathbf{B}$. The nondimensional induction equation governing the evolution of the magnetic field is then,

$$\frac{\partial \mathbf{B}}{\partial t} = \nabla \times (\mathbf{u} \times \mathbf{B} + \alpha \overline{\mathbf{B}}) + \nabla^2 \mathbf{B} \tag{3.9}$$

together with the condition

$$\nabla \cdot \mathbf{B} = 0 \tag{3.10}$$

One should note the overbar in the alpha effect term. We have chosen to regenerate only the axisymmetric part of the field through α with the nonaxisymmetric parts gaining energy only via the $\mathbf{u} \times \mathbf{B}$ term. Although the physically correct approach would be to include α in the entire field since the small scale helical motions should affect the field regardless of its azimuthal structure, one must bear in mind the point of this work. We are interested in the magnetic stability of axisymmetric fields and as such are not overly concerned with the generation mechanism of those fields. Of course, the whole point of using an α effect was to have a more realistic basic state than

simply imposing a diffusionless ambient state. We feel that by restricting α to only the axisymmetric part we have taken the problem one step further than the imposed field approach whilst retaining the underlying principles of a magnetic stability study. We will be able to examine how fully nonaxisymmetric solutions equilibrate at supercritical forcings, a feature not previously studied in mean field models.

Throughout this chapter and indeed the subsequent one the functional form of α chosen was,

$$\alpha = \alpha_0 \cos\theta \tag{3.11}$$

where α_0 is a positive real number representing the magnitude of the forcing. Eq(3.11) applies across the whole gap and is not confined to a narrow layer. One might note that this form of α has been widely used in previous studies, including those in full sphere geometries. In the case of the full sphere the radial symmetry of α must be odd if it is equatorially antisymmetric (see Kerswell & Davey (1996) for a derivation of the symmetries applying to spherical polar vectors in a sphere) and so technically this choice of α is incorrect. However, since our α effect applies only to a spherical shell, the exclusion of the origin allows a relaxation of the symmetries and so eq(3.11) is fully justified in this geometry.

The interaction of the large scale field with the small scale turbulence is neglected allowing equilibration through the effect of the large scale flow alone. The flow is governed by the Navier-Stokes equation

$$2\hat{\mathbf{k}} \times \mathbf{u} = E\nabla^2\mathbf{u} + (\nabla \times \mathbf{B}) \times \mathbf{B} - \nabla P \tag{3.12}$$

along with the incompressibility condition

$$\nabla \cdot \mathbf{u} = 0 \tag{3.13}$$

where we have neglected the inertial terms (cf. eq(1.12)). The Rossby number for the Earth's core is small, possibly as low as $O(10^{-9})$. Including this term in a timestepping

calculation forces one into taking a small timestep to resolve the short timescales that may exist, even though one is only interested in the long term behaviour, hence the use of the magnetic diffusion timescale as temporal normalisation.

However, we do not make the full magnetostrophic assumption by neglecting the viscous term as well. Despite geophysically relevant values of E being perhaps as low as $O(10^{-15})$ we chose to retain this as a parameter in the problem. If one chooses to attempt the magnetostrophic calculation then one is limited to a full sphere geometry. In the spherical shell there are complications introduced by the existence of the tangent cylinder. Hollerbach & Proctor (1993) derived a constraint applying to the forcing of the momentum equation (here the Lorentz force), which, if not satisfied, will induce discontinuities in the nonaxisymmetric components of the flow. When retaining the viscous terms to circumvent this problem via shear layers, current computational resources can only resolve solutions with $E \gtrsim O(10^{-4})$. Slightly lower values can be achieved if one includes hyperviscosity. This is a weighted form of the viscous term which damps modes with high angular structure more than the low order modes. We have chosen not to include this feature into our model since it has been shown that inclusion of hyperviscosity can change the qualitative features emerging from a geodynamo model, for details see Zhang & Jones (1997) and Zhang, Jones & Sarson (1998).

The finite E approach allows us to compare our results with the studies of Hutcheson & Fearn which were outlined in the Introduction. The most important step forward between the two studies has been to move from a cylindrical annulus geometry to the realistic spherical shell. We have also incorporated a finitely conducting inner core as opposed to their insulating core and have implemented a more sophisticated basic state generation mechanism. Due to the added complexity of our model the Ekman numbers attainable are roughly equivalent despite having quicker processors available. The lowest Ekman number of Hutcheson & Fearn was 4.5×10^{-4} while for our α^2 dynamo we have managed 2.5×10^{-4}. We are choosing to implement no-slip boundary

conditions on the flow at both boundaries, in accord with the cylindrical study.

The numerical solution of our system proceeds in a similar manner to that of the previous chapter. Here we apply the poloidal-toroidal decomposition to the field as well as the flow, thereby introducing two new defining scalars, g and h via,

$$\mathbf{B} = \nabla \times (g\hat{\mathbf{r}}) + \nabla \times \nabla \times (h\hat{\mathbf{r}}) \tag{3.14}$$

Again these scalars are expanded in terms of associated Legendre functions

$$g(r,\theta,\phi,t) = \sum_{l,m} g_{lm}(r,t) P_l^{(m)}(\cos\theta)\exp[im\phi] \tag{3.15a}$$

$$h(r,\theta,\phi,t) = \sum_{l,m} h_{lm}(r,t) P_l^{(m)}(\cos\theta)\exp[im\phi] \tag{3.15b}$$

where the index l now runs all the way from 1 to the truncation limit and the time dependence is no longer explicitly separated out. The expansions for $\mathbf{u}$ are identical for the scalars e and f and differ from those in the previous chapter in that we are also summing over azimuthal wavenumbers. In other words, for both field and flow, we are including full equatorial symmetry and resolving all structure in azimuth.

With these expansions, the r-components of eq(3.9) and $\nabla\times$ (3.9) become

$$\sum_{l,m} \frac{l(l+1)}{r^2}\left[\frac{\partial}{\partial t} - L_l\right] h_{lm}(r,t) P_l^{(m)} e^{im\phi} = \mathbf{e}_r \cdot \nabla \times (\mathbf{u} \times \mathbf{B} + \alpha\overline{\mathbf{B}}) \tag{3.16a}$$

$$\sum_{l,m} \frac{l(l+1)}{r^2}\left[\frac{\partial}{\partial t} - L_l\right] g_{lm}(r,t) P_l^{(m)} e^{im\phi} = \mathbf{e}_r \cdot \nabla \times \nabla \times (\mathbf{u} \times \mathbf{B} + \alpha\overline{\mathbf{B}}) \tag{3.16b}$$

where

$$L_l = \frac{\partial^2}{\partial r^2} - \frac{l(l+1)}{r^2} \tag{3.17}$$

The insulating boundary condition on the outer boundary takes the form

$$g_{lm} = \left(\frac{d}{dr} + \frac{l}{r}\right) h_{lm} = 0 \tag{3.18}$$

at $r = r_o$. For a finitely conducting inner core it is not sufficient to prescribe the behaviour of the field on the boundary as with the insulating case. Instead, the field within the inner core must be solved for as well. This is done in exactly the same way as for the outer core field except there is no longer an α effect and the velocity $\mathbf{u} = \Omega_{ic} r \sin\theta \mathbf{e}_\phi$ corresponds to the solid body rotation of the inner core at angular frequency Ω_{ic}. In fact, this calculation can be simplified even further by analytically computing the $\mathbf{u} \times \mathbf{B}$ term in terms of the inner core field expansion functions which we will denote by $\hat{g}$ and $\hat{h}$. The resulting equations are then

$$\sum_{l,m} \frac{l(l+1)}{r^2} \left[\frac{\partial \hat{h}_{lm}}{\partial t} + im\Omega_{ic} \hat{h}^*_{lm} - L_l h_{lm} \right] P_l^{(m)} e^{im\phi} = 0 \tag{3.19a}$$

$$\sum_{l,m} \frac{l(l+1)}{r^2} \left[\frac{\partial \hat{g}_{lm}}{\partial t} + im\Omega_{ic} \hat{g}^*_{lm} - L_l g_{lm} \right] P_l^{(m)} e^{im\phi} = 0 \tag{3.19b}$$

understanding that $\hat{h}_{lm} = \hat{h}_{lm}(r,t)$ and where $*$ denotes complex conjugate. The fields in the inner and outer cores must, of course, match up somehow. The appropriate matching conditions are

$$\begin{aligned} h_{lm} = \hat{h}_{lm} \quad , \quad \frac{dh_{lm}}{dr} = \frac{d\hat{h}_{lm}}{dr} \\ g_{lm} = \hat{g}_{lm} \quad , \quad \frac{dg_{lm}}{dr} = \frac{d\hat{g}_{lm}}{dr} \end{aligned} \tag{3.20}$$

where the first three represent the continuity of the components of the magnetic field and the remaining condition is the continuity of the tangential component of the electric field.

The last statement is not, in fact, strictly accurate since the tangential component of the electric field must clearly involve the alpha effect. However, one can show that the additional term is proportional to $\frac{\alpha}{r}\frac{\partial}{\partial r}(rA)$ evaluated at the inner core boundary. We exclude this term for two reasons. Firstly, we want to build on existing work which has already made this simplificaton, and secondly, one of the results of the previous work was that magnetic field is expelled from the inner core as the forcing

is increased. This will hopefully ensure that the correction term is small and can therefore be ignored. An advantage of this approach is that the boundary condition remains uncoupled in l and m. One should note that there is no such problem for the $\alpha\omega$ dynamo studied in the next chapter since there we only include an α-effect acting on the toroidal field, B.

For the flow, the equations governing the scalars e and f are similar to those derived in Chapter 2. For brevity they are not reproduced here but instead can be found in Appendix B. The no-slip velocity boundary conditions can be written as

$$f_{lm} = e_{lm} = \frac{df_{lm}}{dr} = 0 \tag{3.21}$$

on $r = r_o$, whereas at $r = r_i$ the flow must match to the angular velocity of the inner core and so

$$e_{10} = \Omega_{ic} r_i^2 \tag{3.22}$$

with all other modes as in eq(3.21). Just as we have to solve an additional induction equation for the inner core field we also have to solve an additional equation of motion for the mass of the inner core to determine its angular velocity. Since we are ignoring inertia in the fluid outer core it is consistent to ignore it for the solid inner core as well, leaving a resultant torque balance on the inner core of

$$E \int_S r \frac{\partial}{\partial r}\left(\frac{u_\phi}{r}\right)\Big|_{r=r_i} r_i \sin\theta dS + \int_S B_\phi B_r|_{r=r_i} r_i \sin\theta dS = 0 \tag{3.23}$$

Note that we are allowing the inner core to rotate about the z-axis only ie. the rotation axis of the mantle. Since our system already has an intrinsic rotation, any motion of the core about axes perpendicular to the z-axis should be suppressed and so we ignore this possibility. It turns out that the viscous torque only involves e_{10} and so evaluating the electromagnetic torque allows computation of e_{10} and hence Ω_{ic} using eq(3.22).

So far we have established the equations, boundary conditions and matching conditions for the scalars e, f, g, h and shown, in principle, how to calculate Ω_{ic}. To

implement the system numerically we have to apply some method to our coupled differential equations in r and t. The details of this can be found in Appendix B. Suffice to say, that we expand the r structure in terms of Chebyshev polynomials and use a second order accurate time-stepping procedure to evolve the solution. The Appendix also contains details of all the tests that were performed on the individual subroutines of the code.

3.4 Axisymmetric results

The axisymmetric problem has already received some attention by Hollerbach & Jones (1993a). Using the form of alpha in eq(3.11) and $E = 2.5 \times 10^{-4}$ they studied dipole constrained solutions up to $\alpha_0 = 8.0$. The aim of the work was to examine the adjustment of the field in the inner core to satisfy the second Taylor constraint outlined earlier. In our present study we will not be concerned with this but shall attempt to find where the axisymmetric field becomes unstable to nonaxisymmetric perturbations or indeed perturbations of the opposite parity. From the outset then, we will allow for quadrupole symmetry. Also, it will turn out that the axisymmetric state becomes unstable at much higher values of α_0 than previously studied and so we have chosen to retain an Ekman number of 2.5×10^{-4}. Given that we will be running fully three dimensional calculations later on it would be unwise to try to reduce E any further with current computational resources. The critical values of α_0 for the linear onset of dynamo action are quoted in Table 3.1. As expected for an α^2 dynamo the onset value for the dipole symmetry is extremely close to the quadrupole value but is nevertheless the preferred mode. Furthermore it turns out that both linear eigensolutions are steady at $\alpha = \alpha_c$. The value of α_c for the dipole mode is in exact agreement with that of

	Dipole	Quadrupole
α_c	5.15	5.23

Table 3.1: The linear onset value, α_c, for dynamo action.

Hollerbach & Jones.

The next stage was to map out the bifurcation sequence, if any, of the axisymmetric solutions. The value of α_0 was increased in steps of 0.5 and the system was allowed to equilibrate at each stage. From the pitchfork bifurcation of the trivial state, the dipole branch was followed all the way up to $\alpha_0 = 17.0$ with no subsequent bifurcations. The solution obtained on this branch was steady and tested stable to quadrupole perturbations. Since the problem is nonlinear, it is possible to find multiple solutions ie. two or more distinct solutions at a particular value of α_0. Indeed we managed to find a pure parity quadrupole branch existing in the region $5.5 \lesssim \alpha_0 \lesssim 7.0$. This branch was also steady and stable to perturbations of the opposite symmetry. At $\alpha_0 = 5.5/7.0$ it gains/loses stability, presumably through a pitchfork bifurcation. To visualise what is going on it is useful to plot out a bifurcation diagram which shows the different branches as α_0 is increased. We will use the magnetic energy of the solution as a measure of the field strength and denote this by E_M. Since all the solutions found were steady, the energy is simply given by

$$E_M = \frac{1}{2}\int_V |\mathbf{B}|^2 \, dV \tag{3.24}$$

where the volume V is the entire sphere. There is, of course, a contribution to the energy from the external potential field, but we ignore this and focus on the energy of the conducting region. Eq(3.24) represents a non-dimensional energy, to get back to dimensional units one should multiply by $\mathcal{B}^2\mathcal{L}^3/\mu_0$.

The bifurcation diagram got by plotting E_M against α_0 is shown in Figure 3.1. The most obvious feature of the dipole branch is a change in behaviour at around $\alpha_0 = 9.0$ in the trend of the magnetic energy. Below $\alpha_0 = 9.0$ the energy increases linearly with α_0 and this is the region focussed on by Hollerbach & Jones. Despite carrying out numerous tests on the individual sections of the code it is always good to be able to reproduce the results of an independent study. To this end, we show

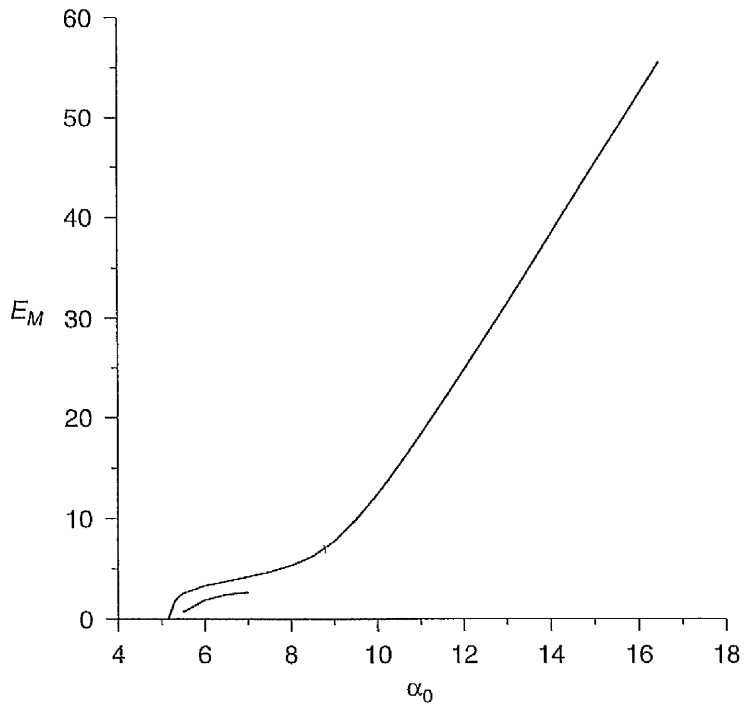

Figure 3.1: E_M vs. α_0 for both dipole and quadrupole, pure parity, steady state branches.

contour plots of the field and flow at $\alpha_0 = 8.0$ in Figure 3.3 which are identical with those in Figure 4 of their paper. We also reproduced Figures 2 and 3 of their work as well but do not show them here. At $\alpha_0 = 8.0$ the field is O(1) and has adjusted to the Taylor constraint on the inner core boundary by removing toroidal flux from the inner core and leaving behind a nearly current-free potential field. This is clear from Figure 3.2 where the electromagnetic torque is actually zero at two points either side of $\alpha_0 = 8.0$ and is generally at its lowest in this region. This figure also shows Ω_{ic} which decreases to zero at $\alpha_0 = 10.0$, demonstrating that the inner core is now passively controlled by the fluid adjacent to it rather than actively driving it.

Whether the equilibration at $\alpha_0 \sim 8.0$ is inviscid in nature is not pursued further here and we turn our attention to the region $\alpha_0 > 9.0$. Here the magnetic energy also appears to increase linearly with α_0 but with a steeper gradient than before. This is perhaps not surprising since we are now forcing the system harder and harder and

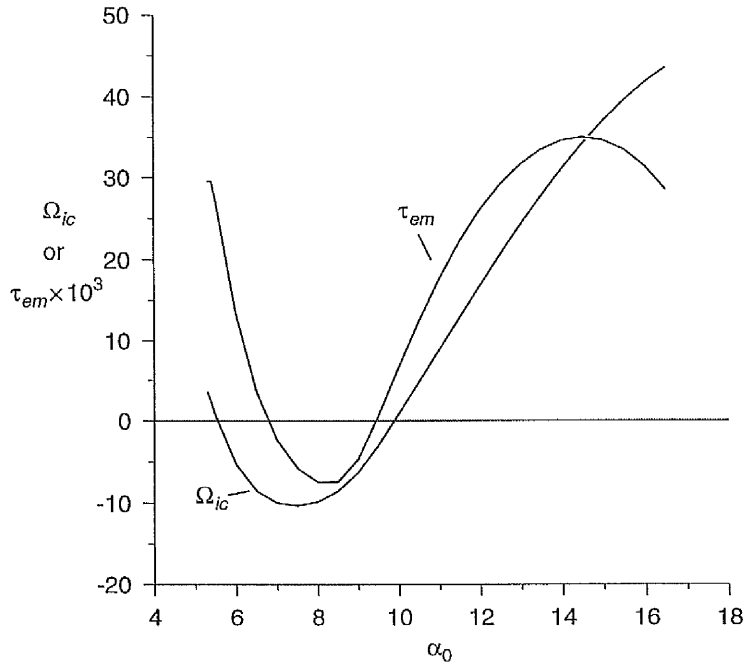

Figure 3.2: Ω_{ic} vs. α_0 for the dipole steady state branch. The corresponding electromagnetic torque, τ_{em}, multiplied by 10^3 to fit on the same scale, is also shown.

would expect to generate an infinite field strength if we let $\alpha_0 \to \infty$. This is of course a completely unphysical limit and for the geodynamo we are only interested in fields in the range O(1-10). At $\alpha_0 = 17.0$ the maximum field strength in the core is ~ 6 in nondimensional units, corresponding to an Elsasser number, Λ, of ~ 36.

One should note that it is more common to talk in terms of the Elsasser number in a magnetic stability analysis since this gives an indication of the field strength rather than α_0 which only measures the forcing. There is no reason for Λ to increase linearly with α_0 and in fact, it is possible that Λ may even decrease over a small localised interval in α_0 and so α_0 cannot be taken as a good measure of magnetic stability. For the case of the $\alpha\omega$ dynamo in the next chapter, we shall illustrate a clear example of how misleading the value of α_0 can be. To demonstrate the point here, all one needs to do is examine the trend of E_M. Since the energetic Elsasser number, Λ', (see eq(1.15) for the definition) is proportional to E_M it will follow exactly the same trend with

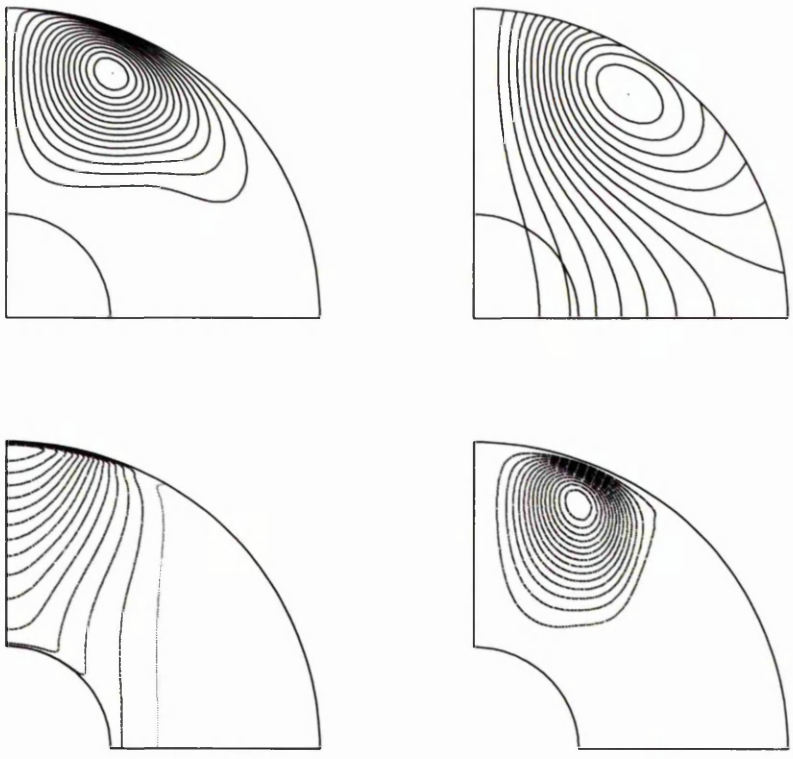

Figure 3.3: Contour plots of B, $Ar\sin\theta$ (top row) and $v/r\sin\theta$, $\psi r\sin\theta$ (bottom row) at $\alpha_0 = 8.0$ Contour intervals are 1/15 of the maximum values which are: $B_{max} = 1.82$, $(Ar\sin\theta)_{max} = 0.35$, $(v/r\sin\theta)_{max} = -77.2$, $(\psi r\sin\theta)_{max} = -0.34$

increasing α_0. For $\alpha_0 \gtrsim 9.0$ a unit change in α_0 gives rise to a bigger change in Λ' than for $\alpha_0 \lesssim 9.0$.

Looking at the inner core rotation we see that we have flipped over to a super-rotation which increases with α_0. There is a slight levelling out of Ω_{ic} at higher α_0 which coincides with a turning point in the electromagnetic torque. At $\alpha_0 = 17.0$ we have $\Omega_{ic} \sim 0.02^o$/year which is two orders of magnitude lower than some of the current experimental estimates although it is in the right direction. This is perhaps not too surprising for a model of α^2 type. Since the toroidal field is generated by α alone it will typically never be much stronger than the poloidal field which shares the same generation mechanism. Thus, the strong field regime, believed to be geophysically

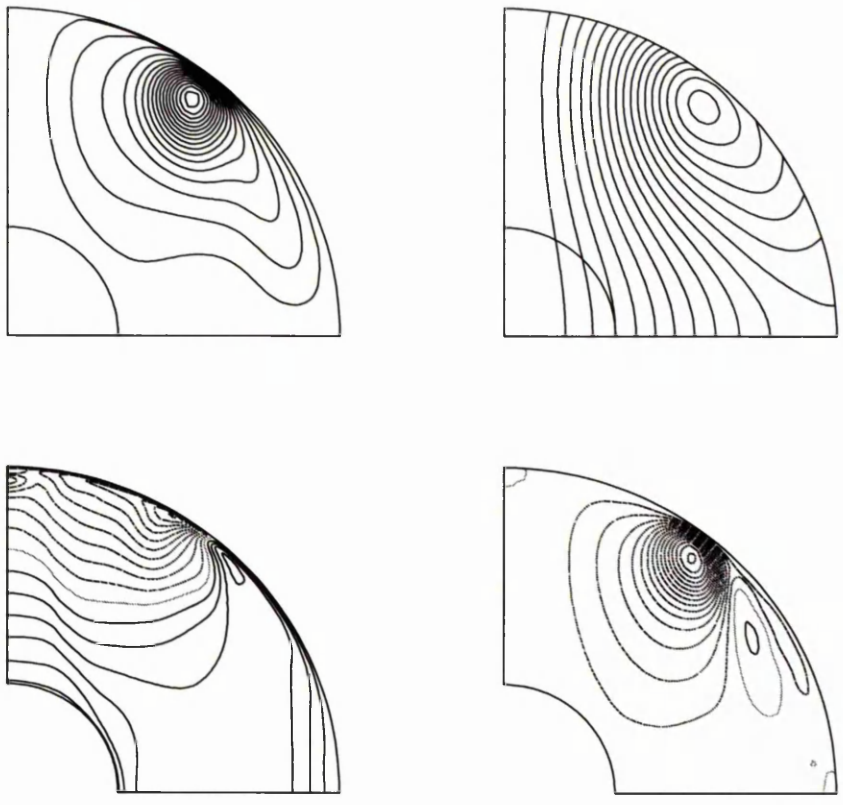

Figure 3.4: Contour plots of B, $Ar\sin\theta$, (top row) and $v/r\sin\theta$, $\psi r\sin\theta$ (bottom row) at $\alpha_0 = 14.0$ Contour intervals are 0.2, 0.08, 5 and 0.08 respectively.

realistic, where the toroidal field exceeds the poloidal by an order of magnitude, is never attained. With larger toroidal fields there will be larger zonal flows which can drive the inner core more efficiently.

The structure of the solutions in this regime are shown in Figure 3.4 for $\alpha_0 = 14.0$. There is little change in the structure of the poloidal field but the toroidal field has clearly changed. The toroidal field has become much more localised and the position of its maximum has changed. Though still located adjacent to the outer boundary the maximum has moved to a lower latitude and now coincides with the maximum of the poloidal field. The meridional flow shows similar behaviour. The angular velocity of the fluid has changed completely, with some locally geostrophic flow appearing in the

previously quiescent region outside the tangent cylinder. There is now just as much superrotation as there is subrotation, with the interface between the two passing very close to the maxima in the other quantities. Inside the tangent cylinder there are the beginnings of the formation of a shear layer almost parallel to the rotation axis but otherwise the flow simply accommodates the super-rotation of the inner core.

To be sure that this is a genuine feature and not a numerical artifact we chose this value of α_0 to carry out a truncation test. (Actually, this value was also chosen because, as we shall see in the next section, the field has already become unstable to nonaxisymmetric perturbations at this point.) By altering the truncation and monitoring the magnetic energy of the solution, the optimum truncations were found to consist of 34 Chebyshev polynomials in radius and 40 Legendre functions in θ for *both* field and flow. All the results presented in this section used this truncation and were timestepped with $\Delta t = 2 \times 10^{-5}$.

3.5 Linear stability results

We now turn to the topic of primary interest in this study. The pure parity axisymmetric fields of the previous chapter have all been tested for stability with respect to perturbations of the opposite parity. In no case was any instability found which would allow formation of a mixed parity state and so the axisymmetric solutions can be assumed to be of pure parity. In this section we will utilise this fact in our search for nonaxisymmetric instabilities. Given a steady state axisymmetric solution ($\mathbf{B}_0$, $\mathbf{u}_0$) we can split each of the field and flow into two parts,

$$\mathbf{B} = \mathbf{B}_0 + \mathbf{b}_m \quad , \quad \mathbf{u} = \mathbf{u}_0 + \mathbf{u}_m \tag{3.25}$$

where $\mathbf{b}_m$ and $\mathbf{u}_m$ represent the nonaxisymmetric components with particular azimuthal wavenumber m. The linearised versions of eqs(3.9,3.12) then become

$$\frac{\partial \mathbf{b}_m}{\partial t} = \nabla \times (\mathbf{u}_0 \times \mathbf{b}_m + \mathbf{u}_m \times \mathbf{B}_0) + \nabla^2 \mathbf{b}_m \tag{3.26a}$$

$$2\hat{\mathbf{k}} \times \mathbf{u}_m = E\nabla^2\mathbf{u}_m + (\nabla \times \mathbf{B}_0) \times \mathbf{b}_m + (\nabla \times \mathbf{b}_m) \times \mathbf{B}_0 - \nabla P_m \tag{3.26b}$$

At this point we will introduce some notation to describe the parities of our solutions. If a vector quantity, $\mathbf{S}$, is dipolar then we will denote this by $\mathbf{S} \in \mathcal{D}$ and if it is quadrupolar we will say $\mathbf{S} \in \mathcal{Q}$. The symmetries described by the terms dipole and quadrupole have the following interpretation when $\mathbf{S}$ is expressed in spherical polar coordinates,

$$\begin{array}{cccc} \text{Dipole} & & \text{Quadrupole} & \\ S_r(r,\pi-\theta,\phi) = -S_r(r,\theta,\phi) & & S_r(r,\pi-\theta,\phi) = S_r(r,\theta,\phi) & \\ S_\theta(r,\pi-\theta,\phi) = S_\theta(r,\theta,\phi) & & S_\theta(r,\pi-\theta,\phi) = -S_\theta(r,\theta,\phi) & \\ S_\phi(r,\pi-\theta,\phi) = -S_\phi(r,\theta,\phi) & & S_\phi(r,\pi-\theta,\phi) = S_\phi(r,\theta,\phi) & \end{array} \tag{3.27}$$

From eqs(3.26a,3.26b) one can easily enough verify the possible symmetries that are permitted for pure parity basic states. One can either have

$$\mathbf{b}_m \in \mathcal{D},\ \mathbf{u}_m \in \mathcal{Q} \quad \text{or} \quad \mathbf{b}_m \in \mathcal{Q},\ \mathbf{u}_m \in \mathcal{D} \quad \text{when} \quad \mathbf{B}_0 \in \mathcal{D} \tag{3.28}$$

or

$$\mathbf{b}_m \in \mathcal{D},\ \mathbf{u}_m \in \mathcal{D} \quad \text{or} \quad \mathbf{b}_m \in \mathcal{Q},\ \mathbf{u}_m \in \mathcal{Q} \quad \text{when} \quad \mathbf{B}_0 \in \mathcal{Q} \tag{3.29}$$

Let us first discuss the short branch of quadrupolar solutions since these turn out to be of little interest. By testing the linear stability of the $\alpha_0 = 7.0$ state for values of m from 1 to 8 it was concluded that this branch was stable to all perturbations. Indeed the decay rates associated with each mode were large enough to deduce that for these field strengths there was no danger of nonaxisymmetric instability at all. The form of the linear eigenfunctions was that of a steady drift about the rotation axis as they decayed.

Turning now to the more interesting dipole case, we first note that an α^2 dynamo is useful in that it has allowed us to test the stability of steady states. Since our basic state is trying to model the long term geomagnetic field, this is one advantage

the model has over the $\alpha\omega$ dynamo, which produces oscillatory states as we shall see shortly, despite being in the weak field regime. Not surprisingly, on the basis of the quadrupole results, when tested at $\alpha_0 = 8.0$, the dipole solution was found to be stable with respect to nonaxisymmetric perturbations up to $m = 8$. Indeed, it was not until $\alpha_0 \sim 13.0$ that any instability was found. Table 3.2 shows the values of α_0 at which the various nonaxisymmetric modes begin to go unstable, and to which parity of field.

α_0	m	Parity
13.1	3	$\mathcal{D}$
13.4	2	$\mathcal{D}$
14.1	4	$\mathcal{D}$

Table 3.2: The critical values of α_0 and parities for the linear onset of nonaxisymmetric modes of azimuthal wavenumber m.

The first surprising thing to note from Table 3.2 is that the mode with the largest structure in azimuth ie. $m = 1$ is not excited first and indeed is not excited in the range of α_0 tested. This is surprising because for our rather high value of $E = 2.5 \times 10^{-4}$ one might expect the mode with lowest azimuthal wavenumber to be excited first. An $m = 2$ mode is, however, the next mode excited at a value of α_0 very close to the $m = 3$ critical value. This is then followed by $m = 4$ again fairly soon after. A common feature of all these modes is their parity. In every case the preferred parity is dipole. To illustrate the variation of decay rate with α_0, Figure 3.5 shows the behaviour of a selection of modes in the range $\alpha_0 \in [11.0, 14.0]$.

The figure shows how the $m = 2$ dipole mode was "nearly" the preferred mode, but for the quicker rate of increase of the $m = 3$ growth rate. The gap between the two increases, which may encourage an $m = 3$ domination of the full nonaxisymmetric solution, at least in this range of α_0. The only quadrupole mode is $m = 1$, which has the smallest decay rate of that particular parity. The decay rates for the other quadrupole modes increases monotonically with wavenumber, and all exhibit the constant profile

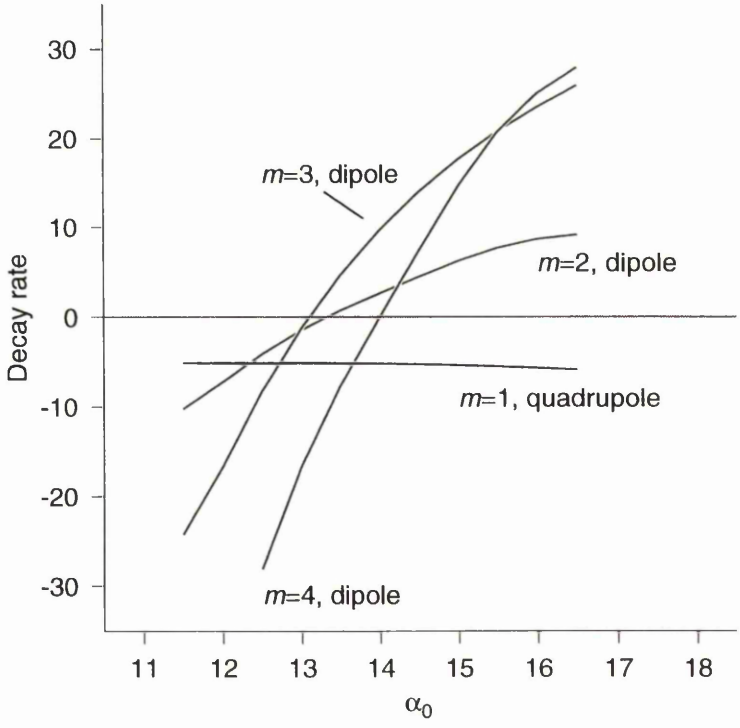

Figure 3.5: Growth rates of selected nonaxisymmetric modes.

shown by $m = 1$.

We can now make our first comparisons with the results of the studies of Hutcheson & Fearn (hereafter collectively referred to as HF). In their analysis with an imposed field, the first mode to go unstable was $m = 1$ when the basic state was independent of z ie. quadrupole. This was at an Ekman number more than 10 times our value which may explain the discrepancy. When they introduced a z-dependence to their basic state, they also lowered their Ekman number to a value comparable to ours. At the new value of E, both dipole and quadrupole basic states yielded an $m = 2$ mode as the first instability which suggests that for $E \sim 10^{-4}$ one should perhaps not expect to see an $m = 1$ mode coming in first at all.

The other similarity between the two models is the preference for a dipole symmetry perturbation when the basic state is dipolar. Indeed HF also found that for their quadrupole state the preferred perturbation field parity was quadrupole, suggesting

that the controlling influence was not the parity of the field, but of the flow. In both cases the perturbations have a quadrupole flow (see eqs(3.28,3.29)) which is the parity required for the formation of columnar rolls, a common feature of non-magnetic convection. Columnar roll formation is a consequence of the Taylor-Proudman theorem which may therefore still be partially operating. One effect of the magnetic field, which is verified here, is to reduce the azimuthal wavenumber of the most unstable mode from the non-magnetic asymptotic limit of $O(E^{-1/3}) \sim 16$. For our solutions, the preferred parity could also be tied in to the existing parity of the basic state flow which is also quadrupolar. Even though our quadrupole basic state was not linearly unstable to any modes, a comparison of the decay rates between $\mathcal{D}$ and $\mathcal{Q}$ perturbations showed that the dipoles were damped much more strongly than their quadrupole counterparts.

We have established that our basic state goes unstable at $\alpha_0 = 13.1$ but the question that remains is how does the Elsasser number for that particular field configuration compare to those reported by HF? It turns out that $\Lambda = 28.3$, which is one order of magnitude different from the value of 1.67 quoted by HF for their dipole basic state (the value for the quadrupole was 2.06). The reason for this discrepancy is presumably to be found in the structure of the fields. As previously pointed out, at this value of α_0 the field has localised very strongly near the outer boundary and at a preferred latitude. The classical Elsasser number only provides information about the maximum of the field which, in this case, does not give a very accurate picture of the field structure. In contrast, we find the value of Λ' to be 4.53 which is in much better agreement with HF's value. The field structure in HF is much more uniform and hence Λ is probably an adequate measure of the field strength in that case.

Finally, we turn to the structures of the nonaxisymmetric eigenfunctions themselves to examine the localisation, if any. Figure 3.6 shows the three components of the $m = 3$ dipole magnetic field at the supercritical value $\alpha_0 = 14.0$. The top row represents the r, θ structure associated with the $\cos(3\phi)$ part of the mode and the lower row shows the

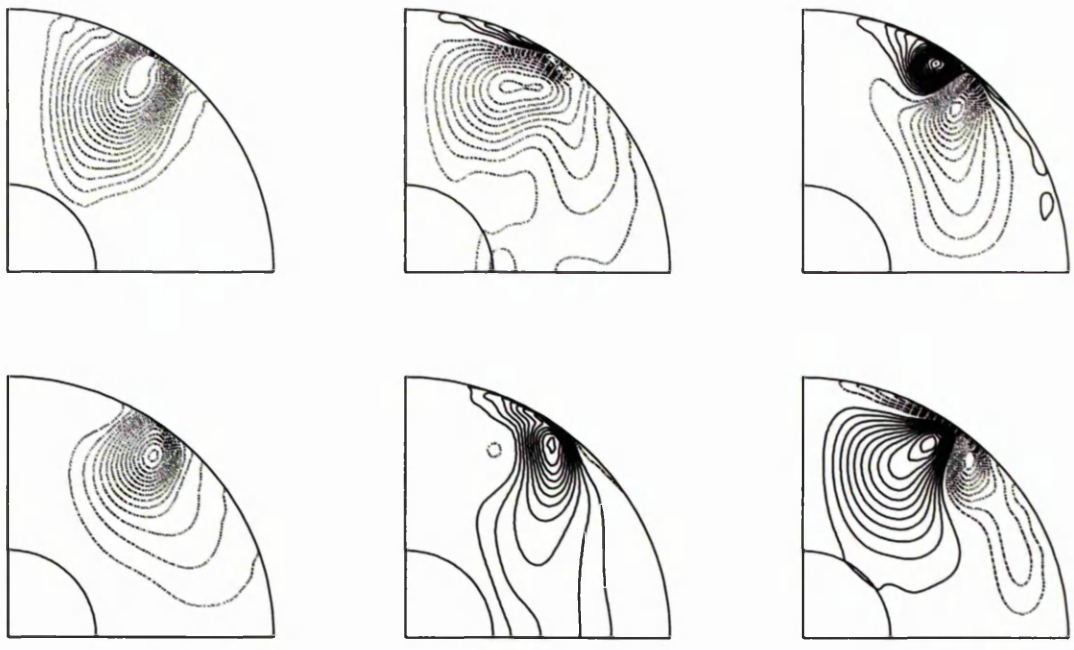

Figure 3.6: Contour plots of the linear eigenfunction of the $m = 3$, dipole mode at $\alpha_0 = 14.0$. Top row shows the meridional structure of the r, θ, ϕ components of the part with $\cos(3\phi)$ behaviour. Bottom row shows the same but for $\sin(3\phi)$. For the sake of comparison, all three components are shown at the same contour interval.

corresponding structure of the $\sin(3\phi)$ part. It is immediately clear that the instability has formed at the same latitude and radius at which the axisymmetric basic state concentrates. This is not unexpected and is in agreement with the solutions found by HF. For their dipole basic state they demonstrated a tendency for the eigenfunction to localise towards the equator due to the critical surface at $z = 0$ where the field vanishes. We do not see this at all because our basic state is not purely azimuthal. The meridional field does not vanish at the equator and so there is no critical surface to help induce instability.

One can see the beginnings of ripples in the contour plots for the linear eigenfunctions due to Gibb's phenomena. We did not carry out any truncation tests on the nonaxisymmetric modes and simply used the same truncation as for the axisymmetric part. Since the instability exhibits slightly more localisation than even the axisym-

metric part, there is correspondingly slightly more fine structure to be resolved. This probably accounts for the slight rippling visible in some of the plots. We could have reproduced these results at a higher truncation but we decided to keep a consistent truncation throughout the whole analysis. If we had used a higher truncation, then the results of the next section, where we include a number of nonaxisymmetric modes simultaneously, would have taken an inordinate amount of CPU time. We have tried to ensure that the region of greatest importance to the analysis ie. the point at which nonaxisymmetric instabilities come in, has been resolved adequately. Since this occurs at $\alpha_0 \sim 13.1$ we believe the truncations are justified. As before, all results were obtained with a timestep of 2×10^{-5}.

3.6 Nonaxisymmetric results

Having established from the linear study which azimuthal modes go unstable first, we now want to investigate the nonlinear equilibration of the solution. Since $m = 3$ is the first mode to go unstable, it will be interesting to see if this mode will dominate the solution or if all m's will be important. The main focus will be on whether the azimuthal symmetry breaking bifurcation is sub- or supercritical in nature and how the instability, once it evolves, extracts energy from the basic state.

We now solve the full system given by eqs(3.9, 3.12), recalling that the α-effect only regenerates the axisymmetric field, calculating the interactions of all the azimuthal modes with one another up to our truncation limits, MB and MU. In practice we always took $MB = MU$ which seems to be the most reasonable choice. To begin with we chose $MB = 6$ and started the run at the supercritical value of $\alpha_0 = 14.0$. The axisymmetric basic state was obviously used as the initial condition for the $m = 0$ part but we chose to include finite energy in both $m = 2$ and $m = 3$ since both of these were linearly unstable for this choice of α_0. For the two nonaxisymmetric modes the corresponding linear eigenfunctions were fed in and normalised so that each had one

m	E_M
0	37.1
3	9.38×10^{-1}
6	8.84×10^{-3}
9	1.99×10^{-4}

Table 3.3: Magnetic energies for the non-zero azimuthal modes at $\alpha_0 = 14.0$

tenth of the energy of the $m = 0$ part. The radial and angular truncations were as before and again a timestep of 2×10^{-5} was required for numerical stability. As the run progressed the behaviour of the two nonaxisymmetric modes was quite different. The $m = 2$ mode started to decay immediately whilst the $m = 3$ mode settled into a finite amplitude equilibration. There was no growth observed in any of the other modes except $m = 6$ where the quadratic interaction of $m = 3$ with itself generated a finite amplitude solution. The run was continued until all non-zero modes had equilibrated to their final state. The $m = 0$ mode was still steady whereas $m = 3$ with its $m = 6$ harmonic had, as in the linear regime, taken the form of azimuthally drifting waves. Since the whole structure rotates rigidly in ϕ this equilibration can be thought of as steady in the sense that the energy associated with it is constant. The equilibrated energies showed that the $m = 6$ mode was roughly 4 orders of magnitude less energetic than the $m = 0$ part. An extra three azimuthal modes were added and the system allowed to equilibrate again. There was little change with the addition of the new modes and as expected only $m = 9$ was excited. The equilibrated energies for the non-zero modes are shown in Table 3.3. Note that the axisymmetric magnetic energy has changed by only 3% from its original value of 38.2. Most of this energy is in the $m = 3$ mode but clearly the instability is unable to extract much energy from the basic state. Figure 3.7 shows the structure of the axisymmetric part of the full solution and should be compared with Figure 3.4. Clearly, there is no noticeable change at all and so, even if this bifurcation turns out to be subcritical, it is probably not of very much interest. The structure of the $m = 3$ part is shown in Figure 3.8 which should be

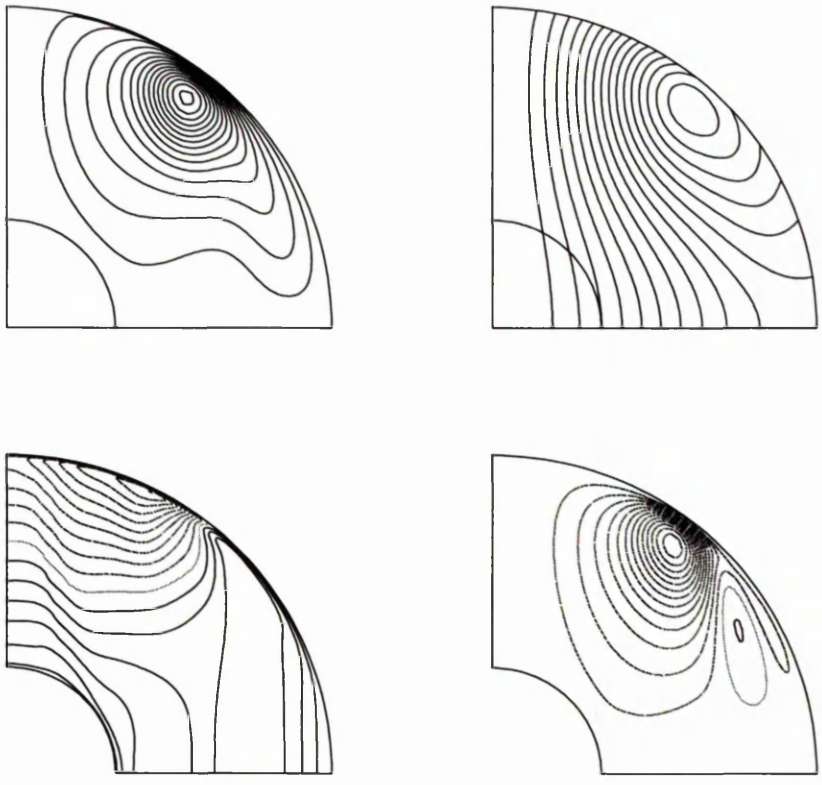

Figure 3.7: Contour plots of the axisymmetric part of the full nonaxisymmetric solution at $\alpha_0 = 14.0$. The contour intervals are exactly the same as in Figure 3.4.

compared with Figure 3.6. During the equilibration process there was no observed growth of the quadrupole symmetry of the $m = 3$ part and so we have again only shown one hemisphere in the plots. Again, there is very little change from the linear regime except that the nonaxisymmetric components are now being maintained at a definite amplitude. A view of the azimuthal structure of B_ϕ and u_ϕ is shown in Figure 3.9 in the plane $z = 1$. The $m = 3$ mode has enough energy to produce a clear perturbation to the underlying axisymmetric contours, however, despite the inclusion of the $m = 6$ and 9 modes, there is no evidence of them whatsoever in the plots. Since the nonaxisymmetric equilibration has favoured the unstable dipole parity of the two $m = 3$ linear eigenfunctions, the resulting final solution is therefore completely dipolar.

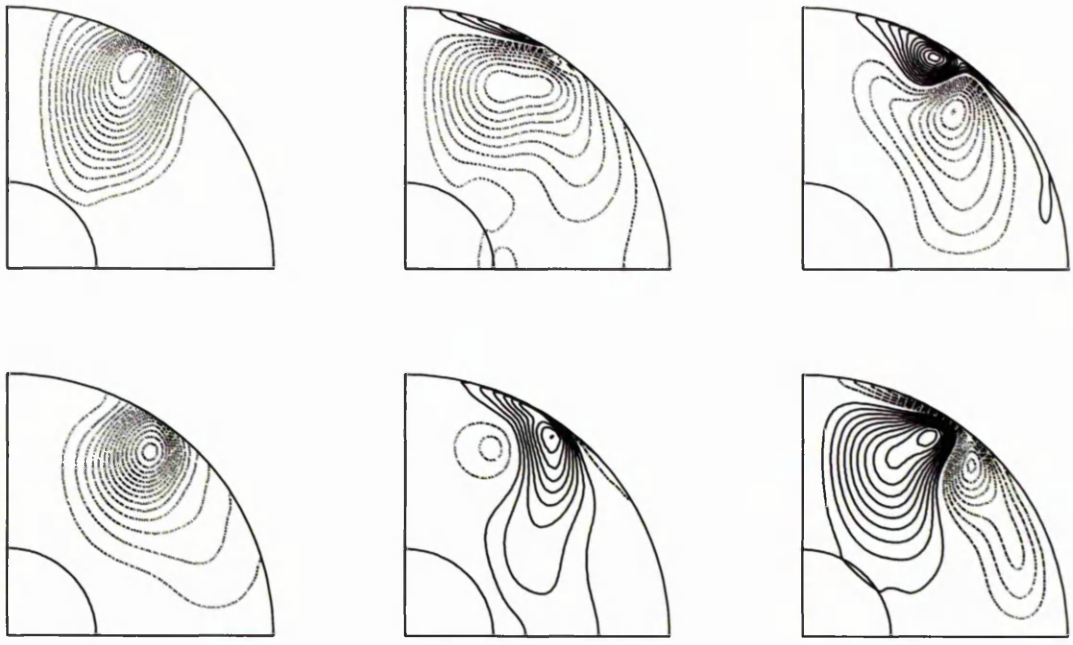

Figure 3.8: Contour plots of the $m = 3$ part of the full nonaxisymmetric solution at $\alpha_0 = 14.0$. The layout is as Fig. 3.4 but contour intervals are now all set at 0.06.

We now turn to the question of subcriticality and test if our full nonaxisymmetric solution can exist in the region of linear stability, $\alpha_0 \lesssim 13.1$. First of all, a solution at $\alpha_0 = 13.25$ was obtained which took the same form as the solution at $\alpha_0 = 14.0$ ie. azimuthally drifting dipole waves in $m = 3$ and its harmonics with a steady dipole axisymmetric part. Using this as an initial condition, a run at $\alpha_0 = 13.05$ was attempted. It was immediately clear that all the nonaxisymmetric parts were decaying, leaving behind the $m = 0$ steady state. This suggests that the azimuthal symmetry breaking bifurcation is supercritical in nature. We can, of course, test for this up to arbitrary precision by taking values of α_0 which are closer and closer to the linear onset value but this is not necessary. In the context of geomagnetic field reversals we are more interested in a solution which can equilibrate at a reasonable strength below linear onset than one which can exist just barely below onset.

Comparing our results to the cylindrical analysis of HF we can confirm that the

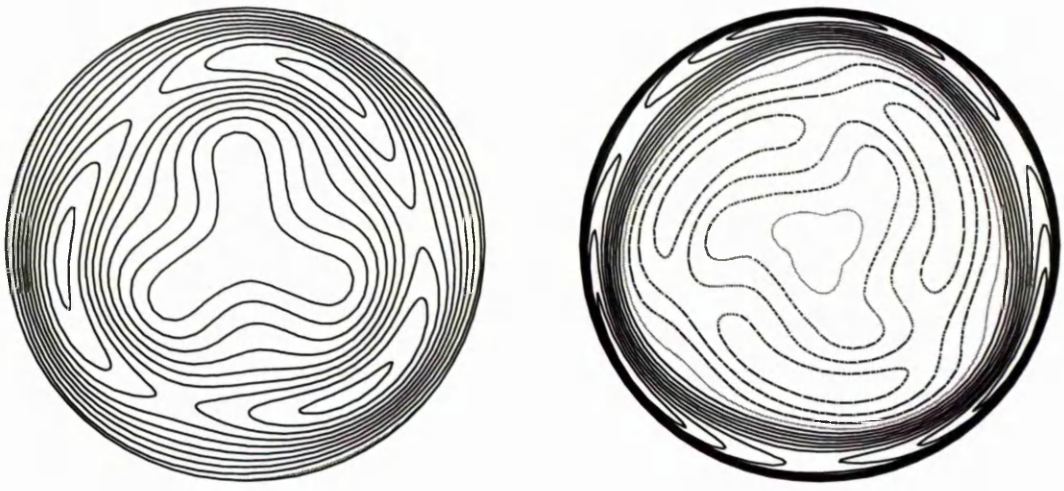

Figure 3.9: Contour plots of the full nonaxisymmetric solution at $\alpha_0 = 14.0$ taken through the slice $z = 1$. On the left is B_ϕ with a contour interval of 0.35. On the right is u_ϕ with a contour interval of 2.5.

nonaxisymmetric solution is dominated by the most unstable mode from the linear analysis. Furthermore, the initial azimuthal breaking bifurcation is of a supercritical nature.

Since we have a fully three dimensional mean field code and have obtained a nonaxisymmetric equilibrated solution from it, we can now increase α_0 to see what happens. After all, if there any subsequent bifurcations we should really check to see if these are subcritical as well. As previously mentioned, the nonaxisymmetric solution that we have can be thought of as steady and so is another ideal candidate to simulate the long term field. One should note, however, that the truncation tests suggest $\alpha_0 = 14.0$ is just within the limits of resolution and so the following results must be interpreted with that in mind. In our purely axisymmetric study we showed that steady dipolar states existed up to the highest value of α_0 attempted at $\alpha_0 = 17.0$. We shall now cover the same range in the nonaxisymmetric case.

Starting with the $\alpha_0 = 14.0$ solution we increased α_0 in steps of 0.5. At $\alpha_0 = 14.5$, 15.0, 15.5 and 16.0 the solution remained in the form of azimuthally drifting waves in

the $m = 3$, 6 and 9 modes. Table 3.4 lists the magnetic energies associated with the axisymmetric field before and after the addition of other azimuthal modes as well as the total energy of the full nonaxisymmetric solution at three different values of α_0. One can see that in each case the energy in the axisymmetric part has been decreased

α_0	$(E_M)^*_{m=0}$	$(E_M)_{m=0}$	$(E_M)_{TOTAL}$
13.25	33.1	32.9	33.0
14.0	38.2	37.1	38.0
16.0	52.1	47.9	51.7

Table 3.4: Magnetic energies for the purely axisymmetric solution, $(E_M)^*_{m=0}$, the $m = 0$ part of the full nonaxisymmetric solution, $(E_M)_{m=0}$, and the total energy of the full solution, $(E_M)_{TOTAL}$ for three values of α_0

from its original value since the nonaxisymmetric modes are drawing their energy from the basic state. The total magnetic energy of the nonaxisymmetric state is very similar to the original $m = 0$ value near the azimuthal symmetry breaking bifurcation as one would expect. This is followed by an increasing difference as α_0 is increased with the total energy always less than the original axisymmetric magnetic energy.

At $\alpha_0 = 16.5$, a change in the temporal behaviour was observed but no new azimuthal modes were excited. The drifting waves acquired a superimposed oscillation as they rotated and the axisymmetric part also became oscillatory. The frequency of oscillation for each azimuthal mode was higher than the drift frequency, but did not appear to be comensurate with it, resulting in a quasi-periodic solution. This new state was tested for subcriticality by reducing α_0 back down to 16.0, but again, a return to the original steady drift behaviour was observed.

At $\alpha_0 = 17.0$ yet another bifurcation was observed, this time another azimuthal symmetry breaking accompanied by another change in the temporal behaviour. Now all azimuthal modes were being excited from $m = 1$ through to our top limit of $m = 9$ but again the only symmetry present in the system was dipolar. The vacillating drift of the nonaxisymmetric components seemed to adopt yet another superimposed

frequency but we did not run the solution long enough to track down this detail. At this point, the nonaxisymmetric modes started having an impact on the axisymmetric part. Table 3.5 shows the energy in each azimuthal mode at a random snapshot in time. The $m = 3$ mode and its harmonics have increased more than the axisymmetric part

m	0	1	2	3	4
E_M	48.5	9.82×10^{-2}	6.12×10^{-2}	6.24	4.52×10^{-2}
m	5	6	7	8	9
E_M	7.66×10^{-3}	0.251	5.88×10^{-3}	1.16×10^{-3}	2.76×10^{-2}

Table 3.5: Magnetic energies for each azimuthal mode at $\alpha_0 = 17.0$

whilst the other modes are also becoming important with $m = 1, 2$ and 4 containing more energy than the $m = 9$ mode. This bifurcation, however, turned out to be supercritical leaving us with no subcritical bifurcations in our α^2 model at all.

In brief summary, we have confirmed that the onset of instability of an axisymmetric basic state occurs at around $\Lambda' \sim O(1)$ $\left(\Lambda \sim O(10)\right.$ for a localised field$\left.\right)$ in our weak-field α^2 model. The evolution of the initial instability is governed by the most unstable linear mode and equilibrates in a state almost unchanged from the initial configuration. All bifurcations have tested negative for subcriticality, although one cannot have full confidence in the secondary and tertiary bifurcations due to limited resolution. The next step is to examine how these results carry through to the strong-field regime pertinent to a dynamo of type $\alpha\omega$. This is the topic of the next chapter.

Chapter 4

Magnetic stability: the $\alpha\omega$ dynamo

So far, we have analysed a fully non-linear and nonaxisymmetric dynamo driven purely by the effect of the small scale helical motions parameterised by the α effect. We have included the back reaction of the resulting field on the large scale flow via the momentum equation and used this nonlinearity to equilibrate our system. Of course, a truly self consistent model of the geodynamo would explicitly include the energy source responsible for driving the core motions. As a step in the right direction we will now progress to the $\alpha\omega$ dynamo where a large scale fluid flow is included as part of the driving mechanism. The details of how this flow is generated and maintained are, again, not included in the formulation and so our system is still rather artificial. Nevertheless, as we shall see, the $\alpha\omega$ dynamo yields solutions that are probably more important to understanding the geodynamo than those from the α^2 dynamo.

In particular, we will be able to address the role of differential rotation in our solutions. Previously, the only differential rotation present in the solutions was that produced by the magnetic field. Now we can include a prescribed differential rotation in our system and examine what effect this has on the solutions. The previous work of McLean & Fearn (1999) suggests that in the limit of vanishing viscosity the differential rotation associated with the geostrophic flow can have a destabilising effect, thus allowing for the possibility of subcritical bifurcations.

4.1 The ω effect

Although the α effect is sufficient to maintain dynamo action, most models make use of the ω effect as well. Indeed, when Parker (1955) first introduced the notion of large scale field regeneration through turbulent motions, the model he put forward was $\alpha\omega$. The key difference between α^2 and $\alpha\omega$ dynamo models is how the toroidal field is generated. Parker only envisioned toroidal field lines being stretched into poloidal field by helical motions rising along radial lines. Instead of appealing to the same effect to generate the toroidal field he opted for a much more direct method. Given some poloidal field, all one needs to do is drive a differential rotation in the flow which will then quite effectively shear out the poloidal field into toroidal field.

Typically this differential rotation takes the form of an imposed flow, $\mathbf{u}_0$, given by,

$$\mathbf{u}_0 = U_0 s\omega \mathbf{e}_\phi \tag{4.1}$$

where $s = r\sin\theta$ and U_0 denotes the amplitude of the flow so that in the notation introduced in the last chapter,

$$\overline{\mathbf{u}}_\phi = v + U_0 s\omega \tag{4.2}$$

The equations governing the evolution of the toroidal and poloidal parts of the field then become (cf. eqs(3.6 a,b)),

$$\frac{\partial A}{\partial t} = D^2 A + \alpha B + N(\psi, A) \tag{4.3a}$$

$$\frac{\partial B}{\partial t} = D^2 B + M(U_0 s\omega, A) + M(v, A) - M(B, \psi) \tag{4.3b}$$

The $M(U_0 s\omega, A)$ term replaces the $\hat{\mathbf{e}}_\phi.\nabla \times [\alpha\nabla \times (A\hat{\mathbf{e}}_\phi)]$ term and represents the production of toroidal field, B, from poloidal field, A. This form of the mean-field dynamo takes its name from the fact that the poloidal field is generated by the α effect with the toroidal field created solely by the ω effect. Of course, one could retain

the action of helical motions on poloidal field and have toroidal field produced by both the shearing motion and the α effect. This is known, not surprisingly, as an $\alpha^2\omega$ dynamo. An $\alpha^2\omega$ dynamo has the advantage that one can study the whole spectrum of mean-field behaviour by simply adjusting the strength of the imposed differential rotation. For $U_0 \ll 1$ one should recover the α^2 dynamo, whereas for $U_0 \gg 1$ one would expect to find an $\alpha\omega$ dynamo. For $U_0 \sim O(1)$ the effect of large scale shearing and small scale turbulence will be comparable.

For the $\alpha\omega$ dynamo as described by eqs(4.3), it is clear that the onset of dynamo action is no longer governed by the magnitude of α alone. The strength, U_0, of the differential rotation must play a part, and it turns out that it is the product $\alpha_0 U_0$ which determines the initial bifurcation from the trivial state. This product, or some derived nondimensionalisation of it, is referred to as the dynamo number. At this point, one can see why the $\alpha\omega$ dynamo typically lies in the strong field regime. If one chooses $\alpha_0 \sim O(U_0^{-1})$ then eqs(4.3)can be rescaled with the transformations,

$$A \to U_0^{-\frac{1}{2}} A \quad , \quad B \to U_0^{\frac{1}{2}} B \tag{4.4}$$

provided $v \ll U_0$. The effect of the differential rotation not only generates toroidal field, but amplifies it as well so that it dominates the poloidal field by a factor U_0.

Since one or both of α_0 and U_0 can be negative, the dynamo number can be either negative or positive. If one takes $\alpha_0 > 0$ then flipping the sign of U_0 can give rise to two different values of α_0 for the critical onset of dynamo action. Similarly, if one fixes $U_0 > 0$ and flips the sign of α_0 then two distinct values are again obtained. In other words the sign of the dynamo number is important as well as its magnitude.

4.2 The ω effect via a thermal wind.

As with the α effect, one is free to choose the form of ω arbitrarily. This means that, despite having introduced a more realistic feature to the model, namely differential

rotation, we are still in the position of having to guess at the most appropriate form for our forcing mechanism. As before, one would hope that the particular choice of ω would not influence the qualitative outcome of the calculations. We are probably safest, therefore, to choose something fairly straightforward, much as we did with our choice of α, which was uniformly distributed across the fluid. A form of differential rotation previously studied by Roberts (1972) and more recently by Hollerbach et al. (1992) is

$$\omega \propto r \tag{4.5}$$

The imposed angular velocity, being independent of θ, simply increases uniformly across the gap. This form however does have obvious problems. If one has no-slip boundary conditions then some sort of modification would have to be made unless the boundaries were differentially rotating. In our model, we have a further complication which makes it impossible to specify ω at all, namely the finitely conducting inner core. As we have already seen from the α^2 dynamo, the magnetic field acts in such a way as to produce a non-zero torque on the inner core. The balancing of this torque is brought about by viscosity which, in turn, requires a rotation of the inner core with respect to the mantle. Since the angular velocity of the inner core is dynamically determined as part of the solution, we cannot specify what value ω should take at $r = r_i$. It is therefore not possible to use the classical approach to supply our system with a prescribed differential rotation.

Fortunately, there is a straightforward way to supply differential rotation without recourse to the classical ω effect. Instead of imposing part of the flow itself, we impose part of its forcing in the form of a buoyancy term in the momentum equation. To see why this should provide us with the flow we need consider the momentum equation,

$$2\hat{\mathbf{k}} \times \mathbf{u} - E\nabla^2\mathbf{u} = -\nabla P + (\nabla \times \mathbf{B}) \times \mathbf{B} + \Theta\mathbf{r} \tag{4.6}$$

with the buoyancy term denoted by Θ. Using the axisymmetric decompositions (3.5),

this becomes

$$2\frac{\partial \psi}{\partial z} + ED^2 v = -N(B, A) \tag{4.7a}$$

$$2\frac{\partial v}{\partial z} - E(D^2)^2\psi = M(B, B) + M(D^2 A, A) + \frac{\partial \Theta}{\partial \theta} \tag{4.7b}$$

where

$$\frac{\partial}{\partial z} = \cos\theta \frac{\partial}{\partial r} - \frac{\sin\theta}{r}\frac{\partial}{\partial \theta} \tag{4.8}$$

In the non-magnetic regime, before dynamo action is excited, eq(4.7b) suggests that for $E \ll 1$ we have the following balance,

$$2\frac{\partial v}{\partial z} \simeq \frac{\partial \Theta}{\partial \theta} \tag{4.9}$$

In geophysical parlance, the v driven by this buoyancy is known as the thermal wind. With an appropriate choice of Θ we can drive a thermal wind that simulates the form of ω given in eq(4.5). Since $v = U_0 s\omega$ we have that

$$\frac{\partial}{\partial z}(U_0 r^2 \sin\theta) = U_0 \cos\theta (2r \sin\theta) - U_0 \frac{\sin\theta}{r}(r^2 \cos\theta) = U_0 r \sin\theta \cos\theta \tag{4.10}$$

and so, if we take

$$\Theta = -\Theta_0 \, r \cos^2\theta \tag{4.11}$$

then $\partial\Theta/\partial\theta$ will have the required form. As can be seen from eq(4.7a) there will be a small ($O(E)$) amount of meridional circulation created as well but this will be dwarfed by the strong differential rotation.

Of course, after the onset of dynamo action the terms involving A and B will become important and so it is only in the linear kinematic regime that this system adequately represents an $\alpha\omega$ dynamo. In the nonlinear regime we would expect that the $M(B, B)$ term would dominate the $M(D^2 A, A)$ term by our previous arguments. In

classical $\alpha\omega$ theory one would neglect the $M(D^2A, A)$ term, however, it has been noted by Barenghi (1993) and Hollerbach & Jones (1995) that this can have a destabilising influence on the dynamics. We will therefore keep both contributions in, which will also allow us to reproduce the results of Hollerbach & Jones as a test of our code.

4.3 Previous $\alpha\omega$ results

The localised Cartesian study of Parker (1955) which first introduced the alpha effect showed that dynamo action was possible in $\alpha\omega$ dynamos. Furthermore, the form of the solution which was obtained contained a very interesting feature – a travelling dynamo wave. Parker called this a migratory dynamo and postulated that this could be potentially important in understanding the dynamics of the Sun. He reasoned that the periodic behaviour of his dynamo could be connected to the observed movements of sunspots and prominences on the surface of the Sun, which migrated from high to low latitudes.

This finding was backed up by Steenbeck & Krause (1969) who looked at the kinematic problem for the $\alpha\omega$ dynamo in a sphere. They found that the linear eigensolutions they obtained were typically oscillatory in nature in contrast to the steady behaviour of the α^2 dynamos. The travelling wave predicted by Parker was indeed confirmed to migrate pole-ward in the spherical geometry if the dynamo number was positive. For negative dynamo numbers the motion was from the poles to the equator. The preferred equatorial symmetry was also dependent on the sign of the dynamo number with quadrupoles easiest to excite for positive values and dipoles for negative.

These results were confirmed by Roberts (1972) who studied other choices of α and ω and also examined one case in a spherical shell. For the shell it was found that the preferred parity for both signs of dynamo numbers changed if the radius of the inner core was large enough but that dynamo action in general was prohibited for these large radii. As with the α^2 dynamos, the preference for one symmetry over the other was

still fairly marginal despite the clear dependence on the sign of the dynamo number. Roberts also looked at the effect of meridional circulation in addition to the imposed differential rotation. For moderate circulations, a transition to steady behaviour was observed with the preferred parity being opposite to that of the oscillatory solutions for weak or zero circulations. The direction of the circulation was shown to play an important role as well, with one sense impeding dynamo action and the other promoting it.

A feature observed in all the oscillatory $\alpha\omega$ models which was obviously lacking in the steady α^2 dynamos was field reversal. From the point of view of explaining the geomagnetic field it would be good to have a model which exhibits some sort of reversal process and so the $\alpha\omega$ models seem like good candidates. Unfortunately the typical timescales of the reversals are far too short to be typical of the geodynamo. It has been noted by Barenghi (1993), however, that the reintroduction of the α effect to toroidal field generation may help. His $\alpha^2\omega$ model exhibited much slower oscillations for values of U_0 believed to be relevant to the Earth's core.

The first study to introduce a nonlinear feedback mechanism on the otherwise linear, kinematic solutions was by Jepps (1975). Using a time-stepping approach he reproduced the previous linear results which had been obtained using an eigenvalue approach. A nonlinearity was introduced in the form of an α-quenched dependence of the toroidal field strength. Different forms were tried, including a cut-off model where the α effect disappears above a critical field strength. An attempt was made to guess what the form of the α-quenching should be by looking at the resulting solutions and comparing them with observed behaviour. Butterfly diagrams matching those of the Sun were more readily found when there was a gradual quenching rather than a sharp cut-off. For the steady state solutions with meridional circulation found by Roberts (1972), it was shown that oscillatory solutions could be recovered as one moved further into the nonlinear regime.

Due to the simplicity of kinematic models only moderate CPU is required and so many other studies of a similar nature were conducted at the beginning of the 1970s. For further references see Lilley (1970), Gubbins (1972, 1973) and Deinzer et. al. (1974). For example, the latter successfully produced steady $\alpha\omega$ solutions without recourse to meridional circulation by localising the α and ω effects into narrow layers. Including the momentum equation represents a much more severe undertaking numerically. The first study to attempt this for the $\alpha\omega$ dynamo was by Abdel-Aziz & Jones (1988) who made the simplifying move to a plane layer geometry. As with the α^2 models, the reason for introducing the momentum equation was to study the evolution of Taylor states. In the Cartesian geometry they did indeed find an Ekman regime where the geostrophic flow was the equilibrating nonlinearity and then an ageostrophic Taylor regime.

The lack of sidewall boundaries in the model of Abdel-Aziz & Jones was unsatisfactory since the travelling dynamo waves were unimpeded and the meridional circulation that could have been induced was absent. The move to a more realistic geometry was undertaken by Hollerbach et. al. (1992) who worked in a full sphere. The model was based on the previous Hollerbach & Ierley (1991) work for α^2 dynamos but now incorporated the usual Laplacian viscosity operator. Using an asymptotic expansion they were able to get $E = 2.5 \times 10^{-9}$. For ω as given in eq(4.5) and $\alpha = \alpha_0 \cos\theta$, they investigated both positive and negative dynamo numbers. The solutions for each branch were qualitatively different with the positive dynamo number solution undergoing a symmetry breaking bifurcation. However, for weakly supercritical dynamo numbers both branches were viscously controlled with an $E^{1/4}$ scaling. For larger dynamo numbers, both branches subsequently evolved to states where the average amplitudes were independent of E, but where the exact details of each solution clearly were not. This was in contrast to the α^2 dynamo where the steady states were unambiguously in an Ekman state or a Taylor state. The results for the $\alpha\omega$ dynamo suggested that

throughout the oscillatory cycle the solution may be in different states at different times making it impossible to classify it one way or the other.

To further complicate matters, a closely related study by Anufriev et. al. (1995) used an $\alpha\omega$ dynamo to produce a state apparently intermediate to that of the Ekman and Taylor states. They called this a "semi-Taylor" state since the field satisfied Taylor's constraint by internal cancellation in the Taylor integral (see eq(1.18)) but without an O(1) scaling. Instead they found a weak $E^{1/8}$ scaling after progressing from the familiar Ekman regime. This scaling was verified analytically by Hollerbach (1997) who showed that not only was this scaling possible, in addition to the other two familiar scalings, but that it was the only other scaling which could be achieved. It was also emphasised that the semi-Taylor state was likely to be a non-generic feature and that an evolution to a Taylor state would probably be favoured. The existence of the semi-Taylor state does however offer the possibility of sudden changes in field strength (from O(1) to O($E^{1/8}$)) without having to drop back to an Ekman state ie. without violating Taylor's constraint.

Models that make use of an imposed buoyancy rather than a classical ω effect have previously been used to determine the effect of using a finitely conducting inner core as opposed to either an insulating one, or none at all. Two papers by Hollerbach & Jones (1993b, 1995) restricted attention to pure dipole symmetry and looked at the axisymmetric solutions obtained at $E = 10^{-3}$ and then $E = 5 \times 10^{-4}$. The solutions were oscillatory, as expected, for moderately supercritical dynamo numbers, and so the effect of the two disparate timescales in the inner and outer cores could be better analysed than in the previous α^2 study. The bifurcation sequence was the same as for the model studied by Hollerbach et. al. (1992) and so the presence of the inner core was not affecting the broad behaviour of the solution. For highly supercritical forcing, a periodic solution was found that exhibited a gradual growth of field followed by a sudden collapse. Consistent with the findings of the α^2 study, most of the field

was concentrated in the outer core, although there was additional evidence to suggest that the localisation was in fact, more precisely, outside the tangent cylinder. The external dipole moment of the solution, however, did not show any signs of the rapid changes that were present in the internal field. Since the field lines which linked the inner core also happened to be the ones that managed to cross the CMB, the effect of the finitely conducting inner core was to smooth out the rapid variations, exactly as predicted. It was also postulated that this effect would stabilise a field reversal in the following sense: Only fluctuations large enough to reverse the field in the inner core would trigger reversals, with the resulting field then relatively stable again after the event.

Hollerbach & Glatzmaier (1998) made the important step of including both parities in the model of Hollerbach & Jones. Right from the onset of dynamo action they found a different bifurcation sequence, with the quadrupole modes being excited first. For moderate forcing they also found a bifurcation to a mixed symmetry state and for large forcings the previously oscillatory upper branch solution became a steady mixed solution. Both results highlighted the dangers of restricting to one parity. Indeed, the upper branch solution no longer exhibited the rapid fluctuations which the inner core had previously smoothed out, and so the influence of the inner core was less obvious.

It is this model that we will start with and extend into the nonaxisymmetric regime. As a further test of our code we will reproduce the axisymmetric bifurcation sequence for both lower and upper branch solutions. We will then modify the imposed buoyancy to provide us with a selection of differential rotations.

4.4 Governing equations and numerical solution

For our $\alpha\omega$ dynamo, the set-up is identical to that in the previous chapter for the α^2 dynamo, except for two things. The first is the addition of the imposed buoyancy term in the momentum equation, and the second is the fact that α is no longer a scalar, but

instead now must be treated as a tensor, $\tilde{\alpha}$. The equations governing the evolution of field and flow in the outer core now become,

$$\frac{\partial \mathbf{B}}{\partial t} = \nabla \times (\mathbf{u} \times \mathbf{B} + \tilde{\alpha}\overline{\mathbf{B}}) + \nabla^2 \mathbf{B} \tag{4.12}$$

$$2\hat{\mathbf{k}} \times \mathbf{u} - E\nabla^2 \mathbf{u} = -\nabla P + (\nabla \times \mathbf{B}) \times \mathbf{B} + \Theta \mathbf{r} \tag{4.13}$$

where

$$\tilde{\alpha} = \alpha_0 \cos\theta \, \mathbf{e}_\phi \otimes \mathbf{e}_\phi \tag{4.14}$$

As before, we are only including the effect of turbulent field regeneration in the axisymmetric part of the magnetic field and are neglecting inertia but retaining a finite E. As in Hollerbach & Glatzmaier we give the buoyancy term the form

$$\Theta = -\Theta_0 \, r \cos^2\theta \tag{4.15}$$

which, as was shown earlier, results in an approximation to an ω effect depending linearly on depth.

The equation determining the field in the inner core is unaltered and is simply

$$\frac{\partial \mathbf{B}}{\partial t} = \nabla \times (r \sin\theta \, \Omega \mathbf{e}_\phi \times \mathbf{B}) + \nabla^2 \mathbf{B} \tag{4.16}$$

The region outside the shell is taken to be an insulator and the appropriate matching conditions are used at the ICB. The numerical method follows the same path as that outlined in the previous chapter.

One important difference between the runs for the α^2 dynamo and the present set-up is the value of the Ekman number. Previously we took $E = 2.5 \times 10^{-4}$ to reproduce the axisymmetric results of Hollerbach & Jones (1993a). However, in the nonaxisymmetric regime, this proved extremely CPU intensive. The results of Hollerbach & Glatzmaier were carried out at $E = 5 \times 10^{-4}$ and so will match this value here to be consistent with their results. This will help to ease some of the numerical difficulties experienced with the α^2 model.

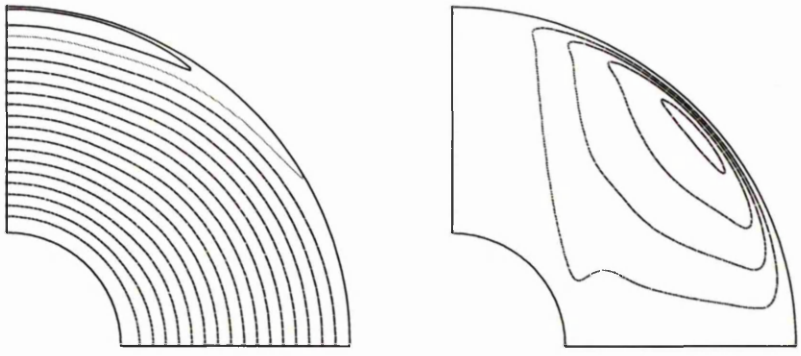

Figure 4.1: The thermal wind, $v/r\sin\theta$, (left) and the meridional circulation $\psi r\sin\theta$ (right) for $\alpha_0 < \alpha_c$. Contour intervals are 10.0 and 0.04 respectively.

4.5 Results for $\Theta_0 = 200$

4.5.1 Axisymmetric results

Our first choice of Θ_0 is that chosen by Hollerbach & Glatzmaier, hereafter referred to as HG, allowing us to reproduce known results. With Θ_0 fixed, we can adjust the dynamo number by simply changing α_0 in a similar fashion as to the previous chapter. The difference here, is that, below the critical value of α_0 for dynamo action, α_c, the fluid flow is in a non-trivial state. For the purposes of a linear analysis to find α_c, we need to find that state. Since the imposed buoyancy term responsible for inducing this flow is constant in time, it is clear that the resulting solution for $\mathbf{u}$ must ultimately be steady. Solving for this flow is then a very simple matter since we have already set up the code to solve the momentum equation for $\mathbf{u}$, given a field $\mathbf{B}$. Setting $\mathbf{B} = \mathbf{0}$, a single call to the routine for inverting the momentum equation yields the required flow. The thermal wind driven by this particular buoyancy can be seen in Figure 4.1 along with the weak meridional circulation which is also induced. The thermal wind is clearly dominated by a linear dependence on r.

From the previous mixed parity study, we know that the quadrupole modes are

	Dipole	Quadrupole
α_c	8.0	6.3
	$\sim$8	$\sim$6

Table 4.1: The linear onset value, α_c, for dynamo action. The second row indicates approximate values from previous studies.

excited before the dipoles but, unfortunately, they do not quote the critical value, α_c to better than one significant figure. The same can be said for the value of α_c for the dipole symmetry reported in Hollerbach & Jones (1995). In Table 4.1 we report our own findings for α_c as well as the approximate values from the two previous studies. The agreement is clearly satisfactory.

As expected, the eigenfunctions have an oscillatory component in addition to the exponential growth near α_c. This result emphasises that the meridional circulation which is necessarily produced is indeed weak, otherwise steady solutions might have been favoured. In the nonlinear regime, the initial bifurcation is to a pure quadrupole state which oscillates about a zero time average and is dominated by dynamo waves travelling from the equator to the pole. This is in agreement with the general behaviour of $\alpha\omega$ dynamos, the parity and direction of dynamo wave propagation being determined by the sign of the product $\alpha_0 \partial\omega/\partial r$. In Figure 4.2, we show the solution at six equally spaced intervals in time, throughout one period of oscillation, for $\alpha_0 = 10.0$. These plots are, apart from a slight difference in phase, identical to those in Figure 1 of HG. The period of the oscillation is found to be 0.22, also in exact agreement with the previous results. One can see that the angular velocity is still dominated by the thermal wind and so the system is still functioning essentially as an $\alpha\omega$ dynamo.

HG then reported a symmetry breaking bifurcation at $\alpha_0 \sim 11$, after which the quadrupole parts continued to oscillate about a zero mean with the now excited dipole parts oscillating about a non-zero mean. The period of the quadrupole parts was double that of the dipole parts which suggested the quadrupole parts consisted of only the odd harmonics with the dipole having the even (including zero) harmonics.

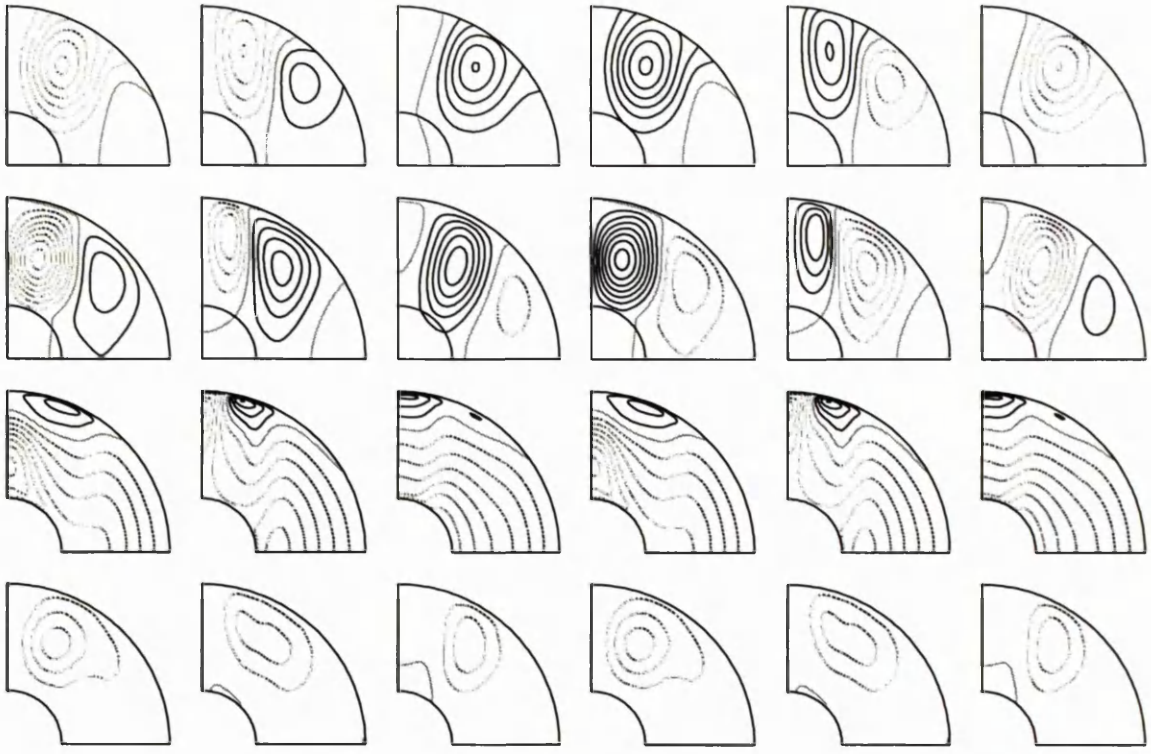

Figure 4.2: Contour plots of (from top to bottom) $Ar\sin\theta$, B, $v/r\sin\theta$ and $\psi r\sin\theta$ at six evenly spaced points throughout one period at $\alpha_0 = 10.0$. Contour intervals are 0.05, 0.5, 25 and 0.25 respectively. cf. Figure 1, Hollerbach & Glatzmaier (1998)

They went on to plot this solution at $\alpha_0 = 15$, and indeed, we are able to reproduce this as well, although we do not show it here to save space. However, the details of the bifurcation sequence to get from the pure parity state to the mixed parity state are not as straightforward as originally proposed. Although the bifurcation reported by HG is perfectly allowable from dynamical systems theory, it turns out that the transition is actually accommodated by, not one, but *four* distinct bifurcations. If one increments α_0 in small steps, even as large as 0.5 say, then a variety of different states can be found in the region of $\alpha_0 \sim 11$. Although not strictly relevant to the nonaxisymmetric linear stability analysis we will do later (all these states turn out to be stable to nonaxisymmetric perturbations), we would nevertheless like to be sure that we understand how the solution has managed to arrive at its mixed parity state. We shall now discuss the short sequence of bifurcations which leads to that state.

For a list of all the possible spatial symmetries and temporal behaviours, see Table 1 of Jennings & Weiss (1991). Detailed analysis of the bifurcation sequences of $\alpha\omega$ dynamos in the context of the solar cycle have previously been made by Tobias (1997) and Knobloch et. al. (1998)

The first of the four bifurcations actually occurs at $\alpha_0 = 10.2$ and is indeed a symmetry breaking bifurcation, in that the dipole parts are now excited. The difference between this new state and the one previously reported is that the dipoles now oscillate about a zero mean, as well as the quadrupoles. The period of oscillation of the two parities is now the same, suggesting the existence of odd harmonics only at this point. At $\alpha_0 = 10.8$ the second bifurcation takes place and breaks the odd harmonic symmetry in the temporal behaviour. Now all harmonics are present and both quadrupole and dipole parts oscillate about a non-zero mean. In the notation of Jennings & Weiss we will call this an asymmetric state.

If one then progresses to $\alpha_0 = 11.4$ an uncommon, but perfectly allowable, bifurcation is encountered. This is called a heteroclinic connection, and results in a solution which exhibits two completely disparate timescales. There is a short timescale that corresponds to the period of oscillation of the solution before the bifurcation and a much longer timescale over which the dipole part of the solution flips sign. This rather, at first, bizarre behaviour comes about in the following simple way: before the bifurcation, there are actually four distinct solutions, corresponding to reversing the signs of the dipolar and quadrupolar parts separately. If we had a non-zero mean in only one of the parities then there would only be two *distinct* solutions since flipping the sign of the parity with zero mean could be offset by shifting in time by an appropriate amount. Suppose that before the bifurcation we are in the state that has both dipole and quadrupole parts oscillating about positive means. As viewed in $\mathcal{DQ}$ space, the solution will follow some sort of closed path around the point defined by the means. At the point of bifurcation, the solution is suddenly unable to follow a path which is

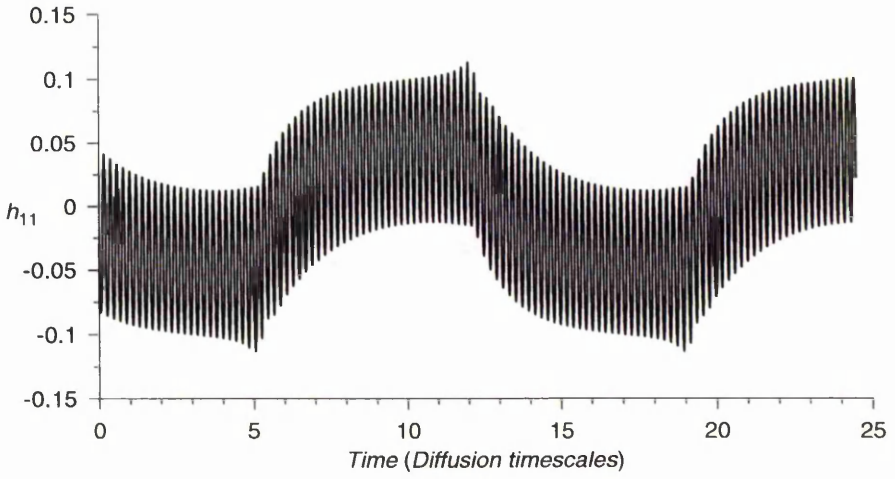

Figure 4.3: The value of the h_{11} coefficient versus time, showing the two disparate timescales of the solution at $\alpha_0 = 11.5$.

exactly closed eg. for one period of the $\mathcal{Q}$ part, say, the $\mathcal{D}$ part doesn't quite manage to complete a cycle. The resulting evolution gradually drifts away from its original position due to this instability and is attracted to one of the other three remaining solutions. However, these are all unstable in the same sense as that described above and so the drift towards the new solution is slower and slower as it approaches. When it reaches its destination, exactly the same process is repeated, which directs the evolution back to the original solution. Thus the solution yo-yos back and forth indefinitely between these two points in the $\mathcal{DQ}$-plane, explaining the long period behaviour. One can also now see why this long period does not violate any of the allowable bifurcation rules of dynamical systems theory. Right at the point of bifurcation, the four solutions are marginally unstable and so the long period will actually be infinite. As α_0 is increased, the period will become finite, but remain large compared to the underlying oscillation period. We verified this behaviour at the initial bifurcation and also at the next bifurcation which returns the solution back to a genuinely periodic state. Figure 4.3 illustrates the behaviour of a randomly chosen dipole spectral coefficient, exhibiting all of the features described above, at $\alpha_0 = 11.5$. Note the long period extends over approximately 14 timescales! The quadrupole equivalent is not shown

since the mean values involved are all extremely close to zero and so almost impossible to discern with the naked eye.

The quasi-periodic behaviour is ended at a bifurcation at $\alpha_0 = 11.8$. Beyond this point we return to the solution branch described by HG which is the one of most interest in the following sections. This branch is a periodic mixed parity state with even harmonics in time for the dipoles and odd for quadrupoles. HG quote that this branch goes unstable around $\alpha_0 \sim 30$ but do not give any further details. We find there is a transition to chaotic behaviour, not uncommon to $\alpha\omega$ dynamos, but at the smaller value of $\alpha_0 = 25$. This discrepancy is slightly worrying, but it is quite conceivable that HG did not take particularly small steps in α_0 in this regime since they were more interested in getting the strong field branch which exists for even higher α_0. Indeed, we were able to reproduce the strong field branch, which comes in at $\alpha_0 = 42$ in the form of a steady mixed parity solution. The fact that we have successfully reproduced all the contour plots from HG suggests our code is working satisfactorily and that any discrepancies are simply due to a lack of resolution in α_0 in HG.

A bifurcation diagram based on the magnetic energies of the various states is presented in Figure 4.4. Points are taken at intervals of 0.5 in α_0 which conveniently gives a point in each of the different regimes described above. Since the solutions are now oscillatory, the magnetic energy has been averaged over one period. In the pure quadrupole regime, just after onset, the energy increases approximately linearly up until the first bifurcation. At this point, the introduction of the dipole parity appears to be the explanation for the sudden increase in energy. The solid line indicates the energy of the full mixed parity solution with the bullet points showing the energy contained in the quadrupole part alone. During the short sequence of bifurcations, and indeed throughout the subsequent evolution of the periodic mixed branch that follows, the quadrupole energy is approximately constant. Once on the periodic mixed branch, for $\alpha_0 > 11.8$, the total energy returns to a trend following more closely that

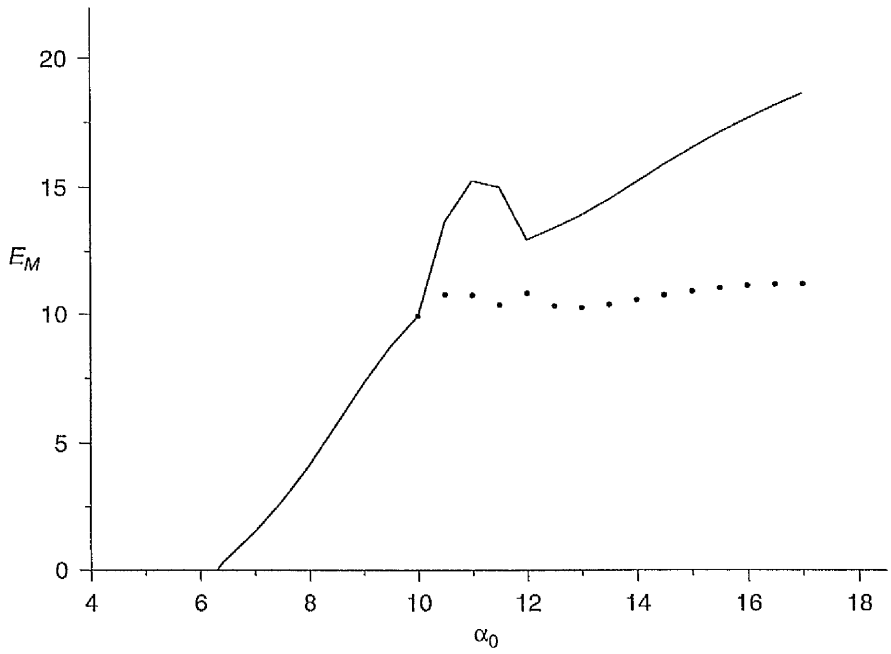

Figure 4.4: Period-averaged E_M vs. α_0.

of the pure quadrupole branch. The effect of increasing α_0 is then simply to increase the energy in the dipole parts until eventually this becomes unstable at $\alpha_0 = 25$ and chaos ensues. The chaotic branch continues as far as we searched, up to $\alpha_0 = 50$. Typically, the chaotic solutions, although showing no repetitive features whatsoever, always stayed statistically stationary in terms of magnetic energy and so a mean value could probably be obtained. As it turns out, we will not be concerned with this branch in the nonaxisymmetric regime and so we did not bother to try to obtain the average energies for this branch.

At $\alpha_0 = 42$ the strong field steady state branch comes in and coexists with the much weaker chaotic regime. The strong field branch was actually rather difficult to obtain since all random initial conditions, including those which had been amplified by arbitrary amounts, yielded the chaotic branch. Fortunately, since this branch had already been found and plotted by HG, it was possible to create initial conditions using simple analytic functions that closely approximated the required steady state.

Using these initial conditions, we were able to obtain the strong field branch relatively quickly. Surprisingly though, the evolution to the correct solution actually evolved via the oscillatory dipole version reported by Hollerbach & Jones (1993b) with the quadrupole parts of the initial conditions initially decaying. After a few diffusion times, the quadrupoles reappeared and the solution settled into a steady state with magnetic energy of ~ 500 at $\alpha_0 = 42$.

Due to limited time we did not bother to search for solution branches coexisting with the pure quadrupole and mixed branches at the lower end of the bifurcation sequence. Since the α^2 model possessed a stable quadrupole branch that coexisted with the dipole solutions, it is quite conceivable that we could find a dipole branch for this particular $\alpha\omega$ model which may itself bifurcate to yet another mixed branch. Although it would be nice, for the sake of completeness if nothing else, to find these branches and test them for nonaxisymmetric perturbations, it would probably yield similar results to the branches we do have. There is nothing to suggest that they should behave any differently, unless they have radically different field morphologies or magnetic energies, neither of which seems likely. In the α^2 model it was inevitable that the pure quadrupole branch would prove to be stable given the range of α_0 that it existed in, and the same principle would apply here.

We conclude this section on the purely axisymmetric behaviour of our model by showing an example of the solution at $\alpha_0 = 14.0$. The contour plots can be seen in Figure 4.5 which, as before, due to the oscillatory nature of the solution, shows six evenly spaced points throughout one period. The equatorial symmetry is clearly broken at any instant in time, however, as pointed out by HG, one can recover an equatorial symmetry by comparing plots half a period apart. This comes about exactly because the quadrupole parts have only the odd harmonics in time with the dipoles having only the even ones. As with the pure quadrupole branch shown earlier, there are dynamo waves propagating from the equator to the pole. They are slightly distorted

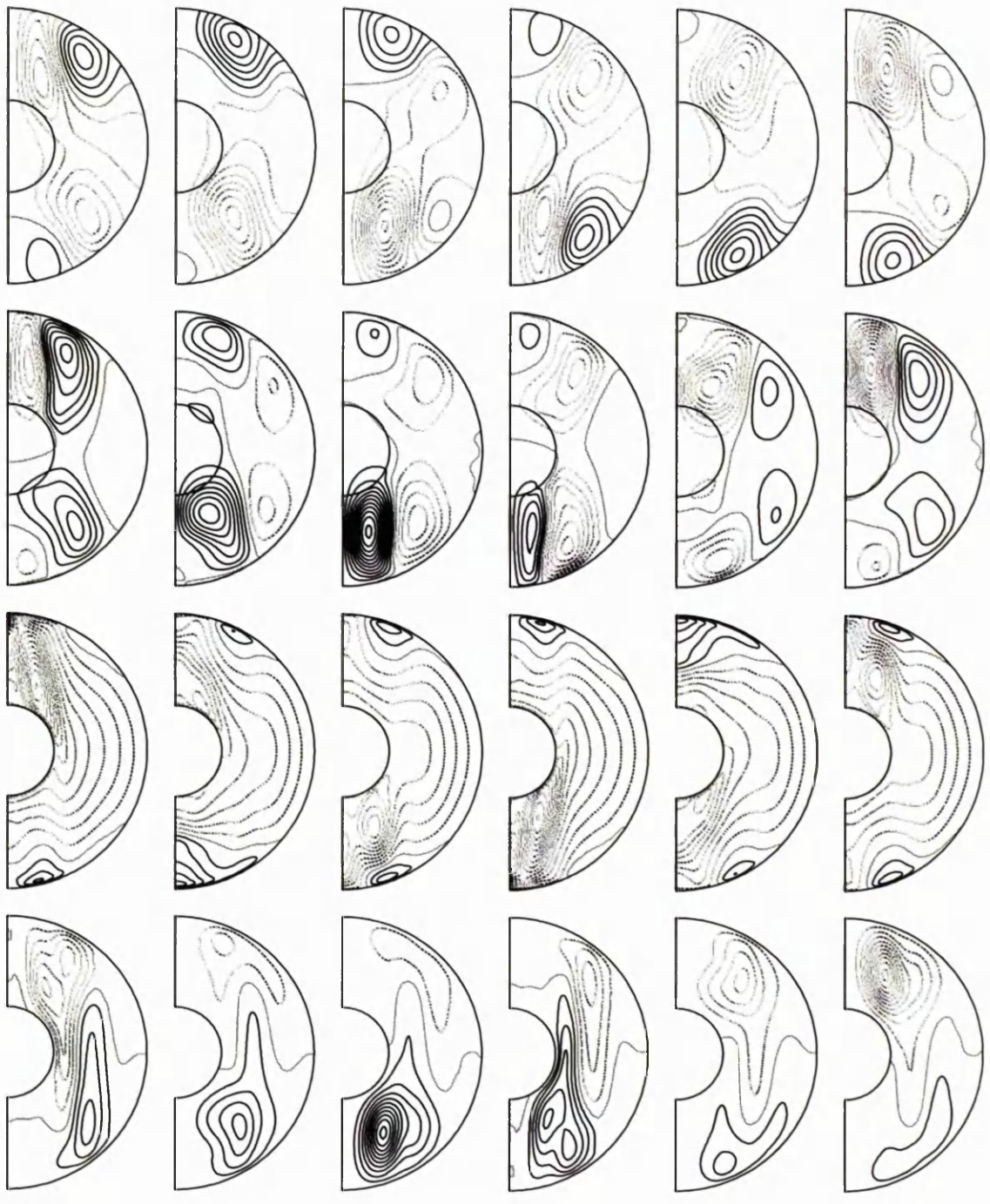

Figure 4.5: Contour plots of (from top to bottom) $Ar\sin\theta$, B, $v/r\sin\theta$ and $\psi r\sin\theta$ at six evenly spaced points throughout one period at $\alpha_0 = 14.0$. Contour intervals are 0.05, 0.5, 25 and 0.25 respectively.

by the loss of equatorial symmetry, but it is interesting to note that some of the field lines now cut the inner core. The period of oscillation, 0.18, is similar to that before the symmetry breaking bifurcation (0.22) at $\alpha_0 = 10.2$ and the general trend is a decreasing one. If the inner core was insulating it could well be the case that the period of oscillation would decrease more sharply as α_0 is increased. The "braking" action of the finitely conducting inner core will not be investigated any further here but it would be interesting to see if this feature could be observed. The contour intervals for the flow show we are still dominated by toroidal motion and that the ω effect is still approximately linearly dependent on r outside the tangent cylinder. Inside, the deviation from this behaviour, which was quite weak for $\alpha_0 = 10.0$, is now much stronger and oscillates from one hemisphere to the other throughout the period.

The convergence of all the results in the range $6.3 \leq \alpha_0 < 25$ were checked by performing a truncation test at $\alpha_0 = 20.0$. Since the Ekman number has been doubled from the last chapter, it was found that truncations consisting of 26 Chebyshev polynomials and 32 Legendre functions were adequate to produce the period-averaged magnetic energy to an accuracy of better than 0.5%. In fact, to facilitate a more thorough exploration of the detailed bifurcation sequence, recalling the long period of the heteroclinic connection, values of α_0 less than or equal to 15.0 were found using 22 Chebyshevs and 28 Legendre functions which seemed to produce satisfactory results. The runs in both the chaotic and strong field branches were performed at the {26,32} level and so must be treated with caution. However, the strong field branch was exactly as found in HG and so the results are better than just qualitatively correct. The low truncation level could also be the reason for the discrepancy between HG and the present work as to where the chaotic solutions come in.

The $\alpha\omega$ model was much more sensitive to the value of the timestep used than the α^2 model in which $\Delta t = 2 \times 10^{-5}$ was used throughout. For the lower range of α_0, between 6.3 and 25, Δt typically varied between 4×10^{-5} and 1×10^{-5}. In the strong

field regime, above $\alpha_0 = 42$, the required timestep was 1×10^{-6} for numerical stability. In all cases the maximum timestep that could be successfully implemented without numerical instability was used. Since this is always less than 4×10^{-5} we believe that any inaccuracy in the solutions is down to the spatial truncations, and that stability is the issue of greatest importance.

4.5.2 Linear stability results

Having established the details of the axisymmetric bifurcation sequence we now proceed to test these states with respect to nonaxisymmetric perturbations. Matters are now a little more complicated than for the α^2 dynamo since the basic states we will be testing are neither steady nor necessarily of pure parity. Previously, we were able to store the values of $\mathbf{B}_0$ and $\mathbf{u}_0$ at the collocation points and solve for the exponential behaviour of the single azimuthal mode by timestepping eqs(3.26a,3.26b). It is certainly possible to attempt a similar approach and store the values of $\mathbf{B}_0$ and $\mathbf{u}_0$ at each collocation point over a sequence of snapshots of the periodic solution. While this approach is just as quick as before, the downside is the extreme memory requirements for the storage ($\sim$ 100Mb). To avoid this problem we solved the equivalent linearised $2\frac{1}{2}$D problem where the axisymmetric basic state is also solved for, but does not receive any back reaction from the nonaxisymmetric mode. This increases the CPU, but not even by a factor two since there are no $\sin(m\phi)$ bits to solve for in the axisymmetric case.

For basic states not of pure parity, it is no longer possible to separate out the nonaxisymmetric modes themselves into pure parities. This is obvious from inspection of eqs(3.26a,3.26b). So in our current $\alpha\omega$ model we start off with a pure parity quadrupole basic state in which the dipole and quadrupole nonaxisymmetric modes can grow or decay at different rates. After the symmetry breaking bifurcation, both the dipole and quadrupole nonaxisymmetric perturbations must grow or decay at the

same rate since they are no longer independent of one another. Of course, the oscillatory nature of the underlying basic state modifies what we mean by the phrase "growth rate". The nonaxisymmetric perturbations will now, in general, exhibit some sort of unknown time dependence in addition to that of the exponential growth or decay that we are trying to ascertain. This additional time dependence has the same period as the axisymmetric basic state and so a quantitative measure of the growth rate is then still possible as long as one compares values at intervals given by the period of the axisymmetric basic state.

It turns out that the pure parity quadrupole branch is stable to all nonaxisymmetric perturbations up to and including $m = 8$. The eigenfunctions take the form of azimuthally drifting waves again, albeit modified by the periodic time dependence induced by the underlying basic state. At $\alpha_0 = 10.0$, just before the symmetry breaking bifurcation, the Elsasser number, $\Lambda = 28.3$. As with the energies quoted earlier, this quantity has been averaged over one period. This is identical to the value at which the first nonaxisymmetric mode started growing ($m = 3$) for the α^2 dynamo and so this particular $\alpha\omega$ model appears to be more stable. However, the period-averaged energetic Elsasser number, Λ' is only 1.40 in contrast to 4.53 previously which highlights the problem of how best to define this quantity.

During the short sequence of four bifurcations which introduces dipole symmetry to the basic state, we have seen that the magnetic energy, and hence Λ', increases momentarily and so we might expect the decay rates to come down. This was, in fact, observed and indeed the $m = 1$ decay rate is very close to marginal over this particular range of α_0. All higher azimuthal modes were still strongly damped though, suggesting that there will be a preference for the mode with the largest structure as opposed to $m = 3$. Also, Λ shows an even bigger jump than Λ' when the dipole symmetry appears, showing that the basic states in this regime are more strongly localised than those before the bifurcation. To illustrate the behaviour of Λ with α_0

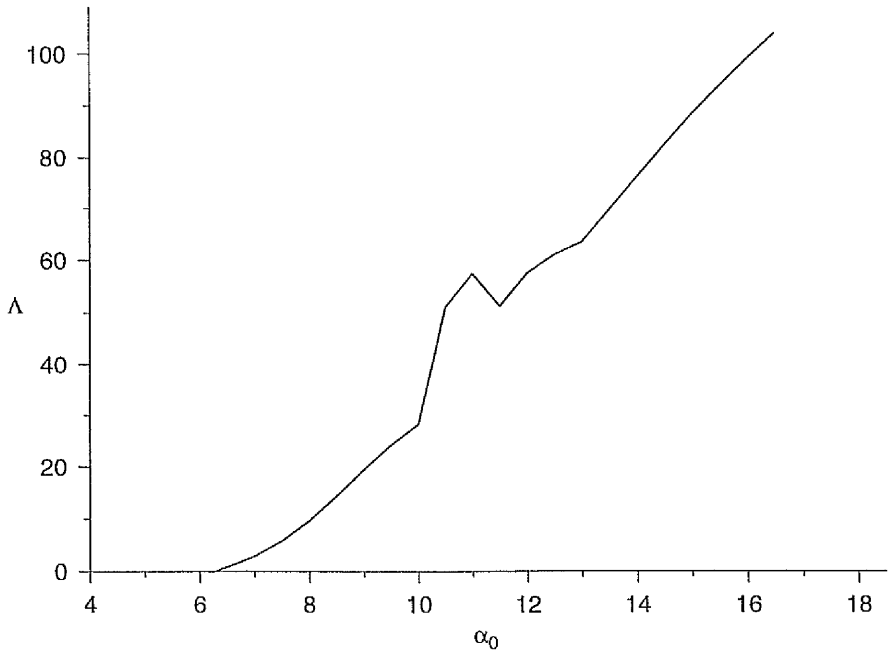

Figure 4.6: Period-averaged Λ vs. α_0.

we plot these two quantities against each other in Figure 4.6.

After all the activity at $\alpha_0 \sim 11$, the behaviour of the magnetic energy and the Elsasser number settles down again to a monotonically increasing function of α_0. The decay rate of the $m = 1$ mode rises again immediately after the last bifurcation but begins to decrease gradually as α_0 is then increased. The decay rate for this mode is approximately 10 times smaller than for the next least stable mode, $m = 2$, and indeed it is the first mode to go unstable. The value of α_0 for marginal stability is 12.8 which corresponds to an Elsasser number of 61.2, or equivalently, $\Lambda' = 1.94$. As compared to the α^2 dynamo, we actually have nonaxisymmetric modes coming in at much higher Λ, but much lower Λ'. The discrepancy between the values of Λ and Λ' is easily enough explained by looking again at the plots in Figure 4.5. Although, at first glance, the field does not seem to be nearly as localised as for the α^2 dynamo, one must remember to take into account the fact that this is now a mixed parity solution. For the snapshots where the field is concentrated in one hemisphere there is almost no

field at all in the other. Since the energetic Elsasser number involves the integral over the whole meridional section it is not surprising that it is appreciably lower than the classical Elsasser number which picks out the point of maximum field strength alone.

The obvious question now is what difference has the differential rotation made to our results. If we go by the classical Elsasser number, we conclude that instability has been inhibited, whereas, if we go with the energetic Elsasser number we could equally well say that the instability has been enhanced! It is probably the case that the ideal measure of field strength is somewhere between the two definitions given here. If we compare our results to previous work then we would expect that the differential rotation supplied here, with $d\Omega/ds$ predominantly greater than zero, would stabilise the system. If that is the case then it would appear that the classical Elsasser number would , in fact, be the more appropriate measure. However, the perturbation to the thermal wind that lies inside the tangent cylinder does provide a region of negative shear for some parts of the period and so perhaps Λ' is really the better choice. We will return to this issue later when we change the value of Θ_0, thus giving us something better to compare the present results with.

As is obvious from the choice of contour intervals in Figure 4.5, the toroidal field far exceeds the meridional field and so we are in the strong field regime as opposed to the weak field of the α^2 dynamo, where both parts were comparable. This could also play a major part in the stability of the axisymmetric basic state. Here the large toroidal field strength is, of course, directly related to the presence of the differential rotation and so we cannot study the two effects in isolation. What we can say, though, is that if the dominance of toroidal field over meridional field plays an important role, then it may not matter what the sign of $d\Omega/ds$ actually is as long as it produces strong toroidal field. Indeed, the work of Fearn, Lamb, McLean & Ogden (1997) was based on imposing arbitrary fields and flows, $\mathbf{B}_0$ and $\mathbf{u}_0$, that were completely independent of each other ie. their basic state was not necessarily consistent with the governing

equations and was therefore rather artificial.

Finally, we take a look at the structure of the linear eigenfunctions to check whether they are concentrated near to the regions of highest field strength in the basic state. Figure 4.7 shows the three components of the magnetic field of the $m = 1$ mode at $\alpha_0 = 14.0$ at the same evenly spaced points as for the corresponding axisymmetric plot in Figure 4.5. The steady drift of the solution has been compensated for, with each slice now effectively at constant ϕ. The growth rate is 7.35 and so we scaled the ith solution down by $e^{-7.35\frac{i}{6}T}$ to focus on the underlying periodicity. This confirms that the eigenfunction shares the same period as the basic state. Also, it has another feature in common, namely the "phase-shifted" equatorial symmetry, arising from the particular combination of even and odd harmonics in time.

During the cycle, the field is totally confined to one hemisphere, the location changing every half period. This is in agreement with the corresponding slices shown in Figure 4.5 which show a similar effect but not to the same degree. One difference though, is that the field is located almost exclusively inside the tangent cylinder for the entire period. Only the ϕ component contains a little field outside this region, presumably associated with the large thermal wind. The dynamo waves are therefore rather squashed up and still consist essentially of two patches of opposite flux as in the axisymmetric case. Surprisingly, although both $m = 0$ and $m = 1$ tend to concentrate in one particular hemisphere in each half of their period, they are apparently out of phase with each other. This is most clearly illustrated by the situation in the third snapshot where the axisymmetric toroidal field is strongly localised in the southern hemisphere. The $m = 1$ eigenfunction, on the other hand, has reached its minimum and has nearly vanished completely. (The field does not, in fact, go to zero as can be verified by looking at the global magnetic energy.) It seems then that the introduction of time dependence to the basic state allows the solution to evolve without the instability necessarily concentrating around the region of highest field strength. This

Figure 4.7: Contour plots of (from top to bottom) B_r, B_θ, and B_ϕ of the $m = 1$ eigenfunction at $\alpha_0 = 14.0$. The slices shown are at constant ϕ after removing the steady drift component. The plots from left to right correspond exactly to those in Figure 4.5. Contour intervals are the same for all plots.

differs from our previous steady state results and indeed was not observed in the work of HF, nor the magnetostrophic analyses of McLean & Fearn.

The truncations used for the linearised $2\frac{1}{2}$D code were exactly the same as for the axisymmetric case. For $\alpha_0 \leq 15.0$, 22 Chebyshev polynomials and 28 Legendre functions were used, whereas for $\alpha_0 > 15.0$, 26 Chebyshevs and 32 Legendres were employed. As in the last chapter we did not carry out any additional truncation tests on the nonaxisymmetric parts, choosing instead to simply retain a consistent truncation throughout.

4.5.3 Nonaxisymmetric results

We shall now follow much the same procedure as before in attempting to establish whether the initial nonaxisymmetric bifurcation is sub- or supercritical in nature. Since no other values of m became unstable after the $m = 1$ mode in the range of α_0 tested, we simply obtained our initial nonaxisymmetric state by using the $m = 0$ periodic solution and the $m = 1$ eigenfunction alone. As before, the linear eigenfunction, chosen at a random point in time, was given one tenth of the energy of the corresponding axisymmetric part and then timestepped to equilibrium. This was carried out at $\alpha_0 = 13.0$ using 9 azimuthal modes in addition to the axisymmetric part.

After a few diffusion timescales the solution settled in to a state with periodic axisymmetric part. The period was 0.18, which was unchanged from the purely axisymmetric case, although the time evolution of the spectral coefficients and the inner core rotation rate throughout one period was noticeably different. The nonaxisymmetric parts had the same periodicity as $m = 0$ in addition to their azimuthal drift. Using this state as an initial condition, the code was then run at $\alpha_0 = 12.7$ ie. in the regime of linear stability. After one timescale it initially appeared as if an equilibrium was being attained with finite energy in the nonaxisymmetric parts. However, as the run progressed, it became clear that the solution could not maintain this indefinitely. After three timescales the nonaxisymmetric parts began decaying rapidly and after a further timescale they had disappeared to such an extent that the axisymmetric part had almost returned to its original unperturbed state. As with the α^2 dynamo, the initial azimuthal symmetry breaking bifurcation is supercritical.

The behaviour of the full nonaxisymmetric solution in the supercritical regime is different to that of the α^2 dynamo in that the $m = 0$ mode is affected much more by the nonaxisymmetric modes just after onset. Table 4.2 shows how the energy decreases by roughly a factor ten for the large scale azimuthal modes at $\alpha_0 = 14.0$. As

the lengthscale becomes shorter, the energy falls off less rapidly with $m = 9$ having roughly half the energy of $m = 8$. The $m = 0$ energy has decreased by approximately 6% of its original value, 15.2.

m	0	1	2	3	4
E_M	14.3	1.08	0.115	1.60×10^{-2}	2.53×10^{-3}
m	5	6	7	8	9
E_M	5.41×10^{-4}	1.24×10^{-4}	3.22×10^{-5}	9.68×10^{-6}	4.48×10^{-6}

Table 4.2: Period-averaged magnetic energies for the individual azimuthal modes at $\alpha_0 = 14.0$.

A sequence of six snapshots of the axisymmetric part of the full solution is shown in Figure 4.8. The snapshots have been chosen to coincide as closely as possible with those from the purely axisymmetric case shown in Figure 4.5. Although the field evolution is very similar, there are clearly some minor differences, in contrast to the equivalent set of plots for the α^2 dynamo. The flow seems to be affected to a greater extent, in particular the toroidal part. We have simply used the same truncation as we did for the axisymmetric and linear results, which appears to cause a slight resolution problem in plots 3 and 6. It is unlikely this will affect the validity of the results since it occurs only briefly in one period and directly affects one quantity (the toroidal field is indirectly affected).

One very noticeable feature in the $m = 1$ behaviour is the drastic change in its drift frequency, $\omega_{DRIFT} = -6.79$, from the linear regime, $\omega_{DRIFT} = -223$. The drift is still retrograde but of a much smaller magnitude. Presumably this must be directly related to the presence and nonlinear interaction of all the higher m modes. If so, then this highlights how misleading a simple linear analysis can be, since the modes above $m = 1$ contribute less than 1% to the total energy of the solution. Accounting for the drift, the three components of the $m = 1$ part of the equilibrated solution are shown in Figure 4.9. Compared with the linear counterpart in Figure 4.7 one can see that the exact details of the mode have changed considerably, although the broad behaviour is

Figure 4.8: Contour plots of (from top to bottom) $Ar\sin\theta$, B, $v/r\sin\theta$ and $\psi r\sin\theta$ at six evenly spaced points throughout one period of the full nonaxisymmetric solution at $\alpha_0 = 14.0$. Contour intervals are 0.05, 0.5, 25 and 0.25 respectively.

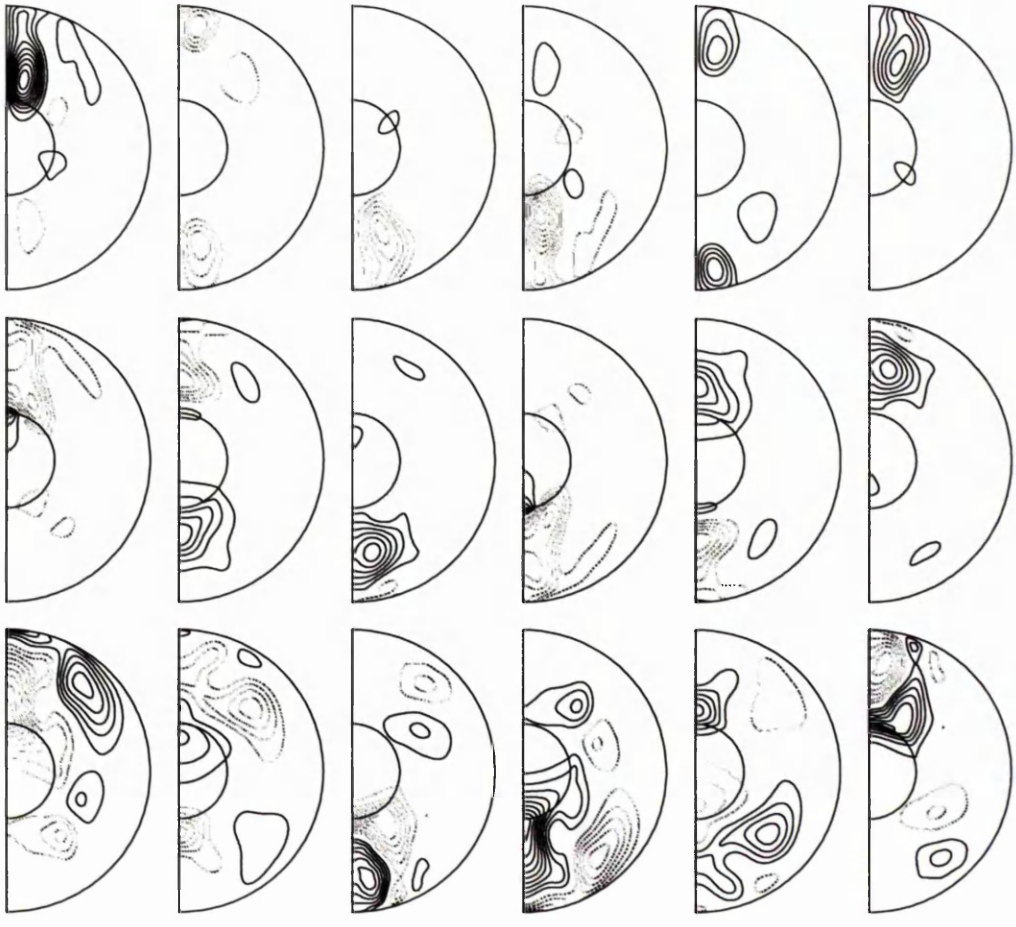

Figure 4.9: Contour plots of (from top to bottom) B_r, B_θ, and B_ϕ of the $m = 1$ part of the nonaxisymmetric solution at $\alpha_0 = 14.0$. The slices shown are at constant ϕ after removing the steady drift component. The plots from left to right correspond exactly to those in Figure 4.7. The contour interval is 0.2 throughout.

similar. For the r and θ components, the field is still essentially localised within the tangent cylinder, with the ϕ component branching out into the exterior region to a greater degree than it did in the linear case. Also, the field still remains more or less in one hemisphere in each half of the period. In the fully nonlinear regime the phase shifted equatorial symmetry is preserved, ie. we still have only odd harmonics in the quadrupole parts and even in the dipole.

To see the variation in azimuth of the full nonaxisymmetric solution we present,

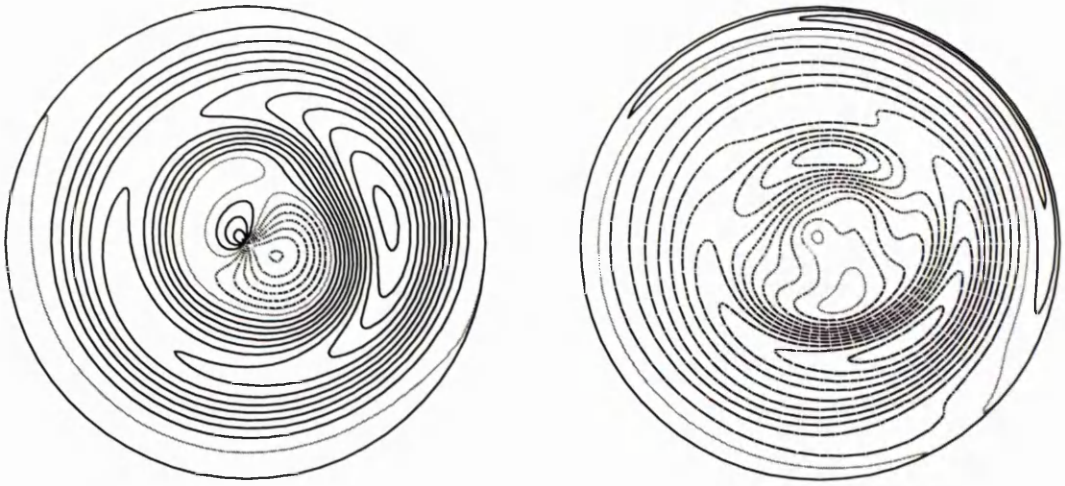

Figure 4.10: Contour plots of B_ϕ (left) and u_ϕ (right) in the plane $z = 1$ at $\alpha_0 = 14.0$. This snapshot corresponds to the first column in Figures 4.8 and 4.9. The contour interval for B_ϕ is 0.4 and for u_ϕ it is 4.0.

in Figure 4.10, a slice through the plane $z = 1$ at the instant in time represented by the first snapshot of the previous plots. As expected from the meridional sections, the field and flow deviate the most from axisymmetry within the tangent cylinder. The $m = 1$ mode is dominant here but it is clear that higher modes are also coming into play.

The α^2 and $\alpha\omega$ models are also similar in the way they behave at higher forcings. With the azimuthal symmetry completely broken, the next bifurcation is to a quasiperiodic state at $\alpha_0 \sim 15$. The short period is still roughly one fifth of a timescale and is modulated by a longer period of about 0.7. The nonaxisymmetric parts are also quasiperiodic as well as maintaining their azimuthal drift. There are certainly variations on the short timescale of the $m = 0$ part, but there is a clear periodic behaviour for all modes on the 0.7 timescale. This is weakly modulated by an even longer timescale, ~ 4, resulting in the quasiperiodicity mentioned. For $m = 1$, the drift frequency is essentially unchanged from that before the bifurcation. This type of behaviour persists at $\alpha_0 = 16$. At $\alpha_0 = 17$, there may be an even more compli-

cated time dependence appearing but we did not run the code long enough to establish what this might be, since our truncations are probably not sufficient at this sort of supercriticality.

4.6 Results for $\Theta_0 = 400$

4.6.1 Axisymmetric results

We now double the buoyancy force to examine the effect of increasing the magnitude of the differential rotation. In the nonmagnetic regime, it is clear from eq(4.13) that doubling Θ_0 will result in a flow which is exactly twice as large as before. The thermal wind and meridional circulation are then exactly as shown in Figure 4.1 but with the contour intervals doubled. As we go into the nonlinear regime we do not expect that this exact scaling will persist, but we do hope we will still have a much larger differential rotation than before.

Since we have not changed the sign of the differential rotation, we would still expect to have the quadrupole modes coming in first, and for the value of α_c to be half the previous value. It turns out that the quadrupole is still easiest to excite, but with $\alpha_c = 3.00$, which is not exactly one half of the previous value, 6.3. The discrepancy shows that, even though it is very weak, the meridional circulation can still produce an observable effect, albeit of little consequence. Similarly, for the dipole branch, the value of α_c was found to be 3.85, in contrast with 8.0 previously.

The solution in the nonlinear regime, past α_c, again takes on the form of an oscillatory quadrupole with zero time average. This solution persists until a symmetry breaking bifurcation at $\alpha_0 = 4.5$. At $\alpha_0 = 4.4$ the solution is still the oscillatory quadrupole and so over this short interval it is possible that there may be a sequence of bifurcations much as we had before. We did not check for this possibility since the bifurcation we have does not require intermediate symmetries, and the interval in α_0 is only 0.1, which is roughly 1/8 of the equivalent interval with half the buoyancy. The

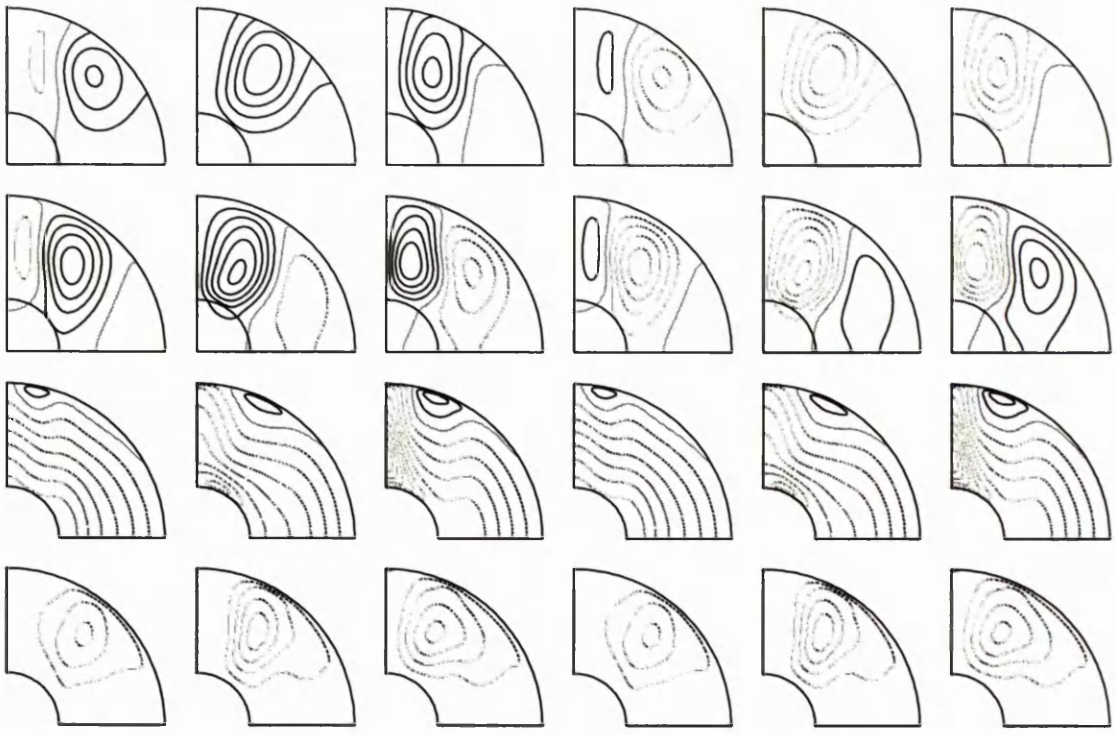

Figure 4.11: Contour plots of (from top to bottom) $Ar\sin\theta$, B, $v/r\sin\theta$ and $\psi r\sin\theta$ at six evenly spaced points throughout one period at $\alpha_0 = 4.4$. Contour intervals are 0.05, 1.0, 50 and 0.25 respectively.

evolution of the pure parity state throughout one period is shown in Figure 4.11 at $\alpha_0 = 4.4$.

The mixed parity solution which results does, however, differ from that in the last section, since the dipole part now oscillates with the same frequency as the quadrupole. It turns out that the total energy has half the period of the field, a feature shared with the flow. This implies that we do not have an asymmetric state, but rather one which only includes the odd harmonics in *both* parities. This state is also mentioned by Jennings & Weiss and so we are not violating any bifurcation rules. The evolution of this state throughout one period is shown in Figure 4.12 at $\alpha_0 = 5.0$. The value of α_0 for which the symmetry breaking bifurcation takes place is less than half of that for the previous model. Looking at the magnetic energy, we see that this has actually

Figure 4.12: Contour plots of (from top to bottom) $Ar\sin\theta$, B, $v/r\sin\theta$ and $\psi r\sin\theta$ at six evenly spaced points throughout one period at $\alpha_0 = 5.0$. Contour intervals are 0.05, 1.0, 50 and 0.25 respectively.

KB	LB	KU	LU	E_M
26	32	26	32	31.07
26	32	30	36	31.07
30	36	30	36	31.08

Table 4.3: Magnetic energies for various truncations at $\alpha_0 = 5.0$.

increased to 22.4 from the previous model's value of 13.7, showing that, if anything, the present model has actually had its symmetry broken later than the previous model. The bifurcation diagram is not shown here, but it exhibits the same behaviour as previously noted. The newly acquired dipole symmetry monopolises the energy input when α_0 is increased, leaving a fairly constant quadrupole part.

The truncations for this model were increased from the last section to take into account the larger differential rotation now present. A truncation test was carried out at $\alpha_0 = 5.0$ which suggests that the field and flow should still be resolved to the same extent. The period-averaged magnetic energies are shown in Table 4.3.

4.6.2 Linear results

As before, we have two distinct regimes in which to test for linear stability. One where the dipole and quadrupole modes will grow or decay independently, and one where they are coupled. To speed up the process, only the $m = 1$ mode was tested initially in the range $4.0 \leq \alpha_0 \leq 6.0$. Since this model has behaved in a similar fashion to the last one for the axisymmetric states, this seems a reasonable starting choice. Instability for this mode was found when $\alpha_0 = 4.31$, which is still in the pure quadrupole regime for the basic state. Only the dipole parity is excited, although the quadrupole comes in straight after, at $\alpha_0 = 4.32$. This is slightly surprising, since the parity of the associated flow eigenfunction is dipole, which is at variance with the results of HF and for our own α^2 dynamo. Again, as we pointed out for the case of eigenfunction concentration, one may point to the time dependence as a possible candidate for disrupting the previous pattern of results. Of course, one should remember that there is not much difference

between the onset of the two parities, and indeed, both are present soon afterwards when the basic state becomes mixed.

The period averaged critical Elsasser numbers corresponding to $\alpha_0 = 4.31$ are $\Lambda = 30.9$ and $\Lambda' = 2.67$. Increasing the differential rotation has produced another situation where Λ exhibits a different change than Λ'. Since the axisymmetric plots have a quadrupole symmetry, they are even less localised than they were before, hence Λ and Λ' are closer than for the previous buoyancy. Since the positive gradient of differential rotation should be stabilising, we expect to see higher Elsasser numbers than before. It would therefore appear that the energetic Elsasser number is the appropriate measure, as expected from the differing degrees of localisation of the two basic states under comparison.

To ensure that $m = 1$ is the first nonaxisymmetric mode to go unstable, we tested the basic state at $\alpha_0 = 4.31$ to both dipole and quadrupole perturbations up to and including $m = 8$. No other modes were found to be stable, with the decay rates increasing with wavenumber as is illustrated in Table 4.4. From these values we can

m	1	2	3	4	5	6	7	8
Dipole	+0.20	-64	-93	-115	-138	-160	-184	-208
Quadrupole	-0.39	-56	-82	-99	-125	-142	-170	-187

Table 4.4: The decay rates for the pure parity eigenfunctions, obtained by comparing the solutions one period apart, at $\alpha_0 = 4.31$.

see that the $m = 1$ mode actually behaves in the opposite manner to all the others with respect to parity selection. This suggests that the preference of a dipolar flow, as opposed to the expected quadrupole, may indeed be a non-generic result, perhaps simply an artifact of our particular choice of α and Θ. Of course we cannot assume that the parity selection of the higher azimuthal wavenumber modes at their individual critical onset would remain as they are at $\alpha_0 = 4.31$ and so further testing is desirable, but not within the scope of this work.

Figure 4.13 shows the structure of the $m = 1$ dipole eigenfunction as it evolves

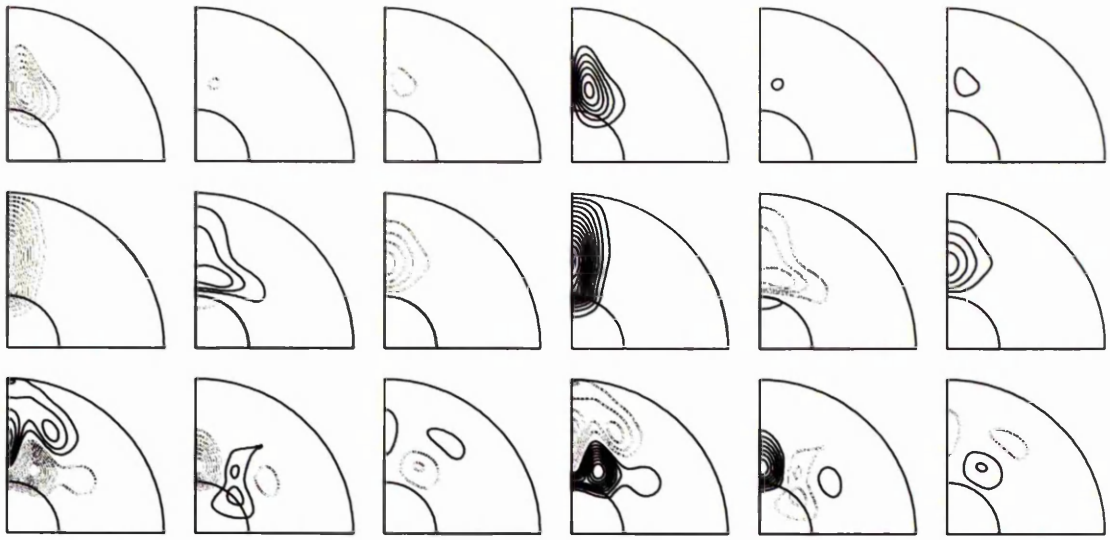

Figure 4.13: Contour plots of (from top to bottom) b_r, b_θ, and b_ϕ of the $m = 1$ eigenfunction at $\alpha_0 = 4.4$. The slices shown are at constant ϕ after removing the steady drift component and exponential growth. The plots from left to right correspond exactly to those in Figure 4.11. Contour intervals are the same for all plots.

in time. Once again, the drift and growth have been compensated for, and the six snapshots were taken at the same time as the axisymmetric plots in Figure 4.11. One can show easily enough that for a basic state with odd field harmonics and even flow harmonics, the resulting perturbation equations will admit two separate time dependences in the eigenfunctions. The one that is selected in this case is that having the same behaviour as the basic state ie. odd field and even flow. Due to its equatorial symmetries, this eigenfunction cannot localise itself within one hemisphere as with the mixed parity solution for the previous choice of Θ_0. It does, however, show signs of growth and decay throughout its periodic cycle and again is concentrated primarily within the tangent cylinder. The intense regions in the first and fourth plots are apparently unconnected to any such behaviour in the underlying basic state, which varies little in magnitude throughout its period.

In the mixed parity regime, at $\alpha_0 = 5.0$, the $m = 1$ eigenfunction that grows most quickly is the one which has the opposite time dependence to the basic state. The field

Figure 4.14: Contour plots of (from top to bottom) b_r, b_θ, and b_ϕ of the $m = 1$ eigenfunction at $\alpha_0 = 5.0$. The slices shown are at constant ϕ after removing the steady drift component and exponential growth. The first, third and fifth columns correspond exactly to the first three columns in Figure 4.12. Contour interval for b_r is one half of that for the other two components.

has even harmonics and has half the period of the flow which has the odd harmonics. Since the second half of one period will be identical to the first, Figure 4.14 shows six evenly spaced snapshots of the magnetic field over the first half of the period. The relaxation of equatorial symmetry has again encouraged the solution to localise in one hemisphere, although the effect is not as pronounced as before. The localisation within the tangent cylinder still appears to be a general feature of the nonaxisymmetric eigenfunctions, as does the lack of flux across either the inner core boundary or the

core-mantle boundary.

4.6.3 Nonaxisymmetric results

A snapshot of the mixed parity $m = 1$ eigenfunction at $\alpha_0 = 5.0$ was given one tenth of the energy of the simultaneous $m = 0$ basic state and then the full nonaxisymmetric equations were timestepped forward. The solution settled in to a state with the time dependence as predicted from the linear theory. In contrast to the previous choice of Θ_0, the drift frequency of the $m = 1$ mode (-0.70) was relatively unchanged from that of the linear eigenfunction (-0.88). With the present choice of Θ_0, we can examine what the behaviour of the nonaxisymmetric solution will be when we reduce α_0 back down to the $m = 0$ pure parity regime whilst still remaining supercritical and thus being assured of finite equilibration.

First of all, a run was made at $\alpha_0 = 4.5$, in which the dipole parts of the $m = 0$ mode and the quadrupole parts of the nonaxisymmetric modes started to decay. After running for 4 timescales the solution eventually equilibrated with finite amplitude in *all* symmetries and so the nonaxisymmetric solution is mixed parity over at least the range indicated by the linear analysis. The next run was made at $\alpha_0 = 4.35$ in which the aforementioned parities began to decay again. No sign of equilibration was found and so the energy in the decaying $m = 0$ dipole mode was quartered and the run restarted. This was repeated twice with no sign of the decay stopping, and so it appears that the nonaxisymmetric solution follows the parity selection exactly from the linear analysis.

The last test was to see if subcritical solutions could be obtained in the linearly stable regime. A run at $\alpha_0 = 4.3$ showed immediate decay of all nonaxisymmetric parts and so the procedure of reducing the energies was again employed to save time. The nonaxisymmetric energies were all reduced by a factor of 25, after which they continued to decay, leading us to conclude that the azimuthal symmetry breaking

Figure 4.15: Contour plots of (from top to bottom) $Ar\sin\theta$, B, $v/r\sin\theta$ and $\psi r\sin\theta$ at six evenly spaced points throughout one period of the full nonaxisymmetric solution at $\alpha_0 = 5.0$. Contour intervals are 0.05, 1.0, 50 and 0.25 respectively.

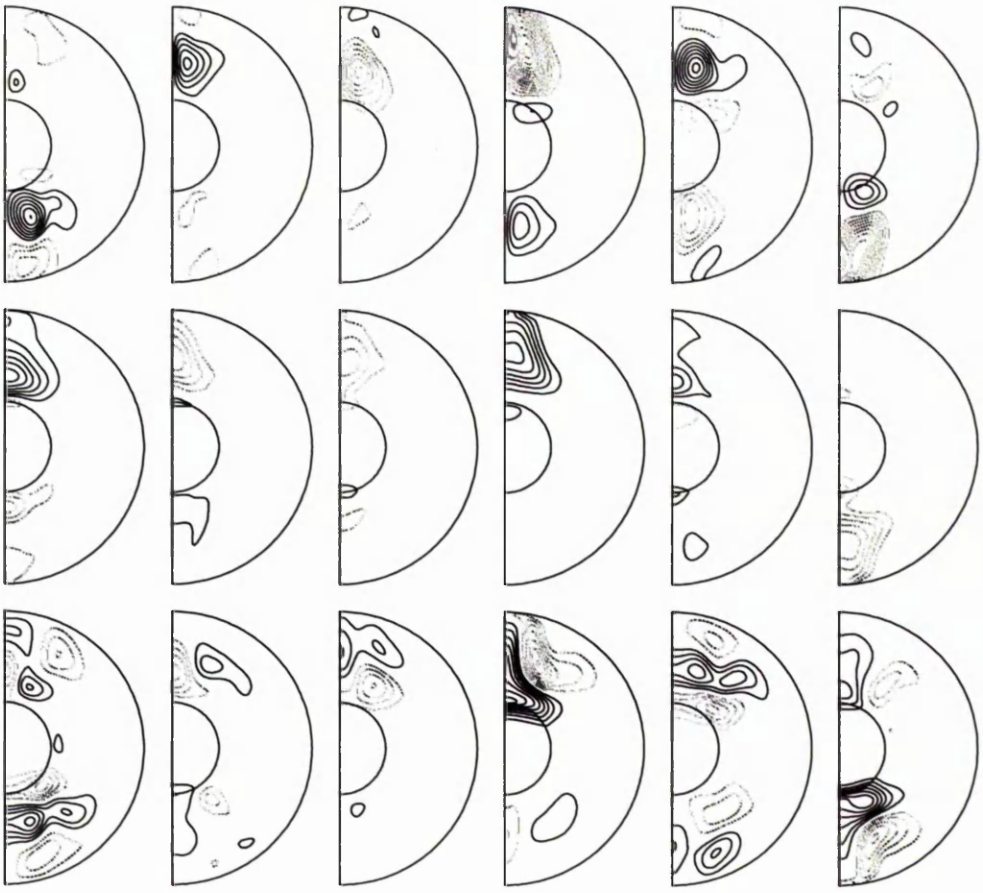

Figure 4.16: Contour plots of (from top to bottom) b_r, b_θ, and b_ϕ of the $m = 1$ part of the nonaxisymmetric solution at $\alpha_0 = 5.0$. The slices shown are at constant ϕ after removing the steady drift component and exponential growth. The first, third and fifth columns correspond exactly to the first three columns in Figure 4.12. Contour interval for b_r is 0.1 with 0.2 for b_θ and b_ϕ.

bifurcation is supercritical in nature.

Returning to the structure of the nonaxisymmetric solutions, we have chosen to focus on the mixed parity regime at $\alpha_0 = 5.0$. Figure 4.15 shows the axisymmetric part of the solution at a sequence of similar snapshots to those in Figure 4.12. The field is relatively unchanged with the flow being affected only slightly more. The $m = 1$ part of the solution is shown in Figure 4.16, again only over the first half of the period. As before, there seems to be a lot of fluctuations throughout a single period, but the

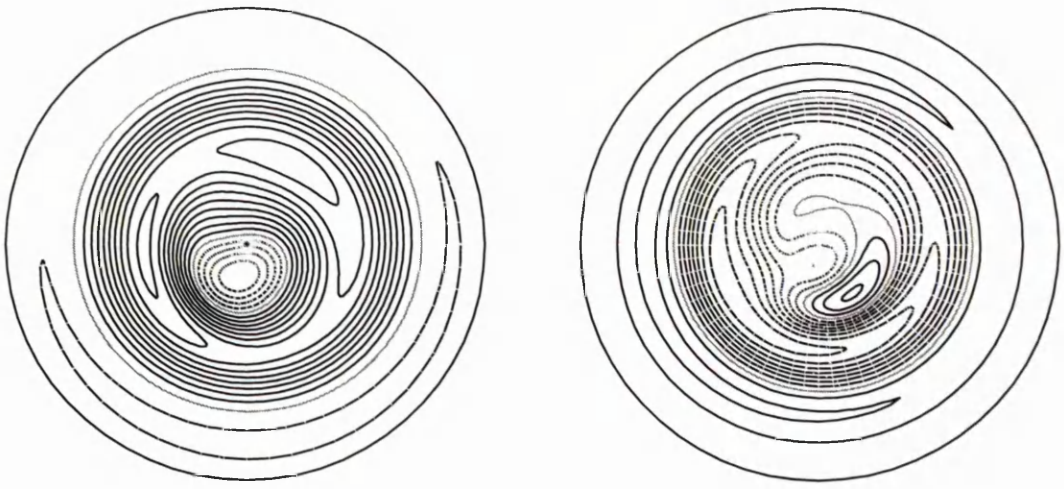

Figure 4.17: Contour plots of B_ϕ (left) and u_ϕ (right) in the plane $z = -1$ at $\alpha_0 = 5.0$. This snapshot corresponds to the first column in Figures 4.15 and 4.16. The contour interval for B_ϕ is 0.2 and for u_ϕ it is 2.0.

main feature is still that the field is localised within the tangent cylinder.

The importance of the various azimuthal modes can be seen by looking at a slice through constant z. Figure 4.17 shows the slice $z = -1$ corresponding to the first snapshot of the previous plots. The axisymmetric solution is dominant outside the tangent cylinder but perturbed inside it. The perturbations are clearly more than just the $m = 1$ mode, showing that once the linear instabilities are allowed to evolve, they can extract enough energy from the basic state to make an impact on the structure of the overall solution.

4.7 Results for $\Theta_o = -200$

4.7.1 Axisymmetric results

The final model we shall consider is one where the direction of the buoyancy, and hence the thermal wind, has been reversed. In the non-magnetic regime the contours look exactly as in Figure 4.1, but with the opposite signs. A similar model to this was studied by Hollerbach (1998) who included an exponential factor limiting the

thermal wind to the region inside the tangent cylinder. The model studied the effect of imposing a potential field on the system, rather than invoke mean field theory, and found that a large geostrophic flow, opposite to the thermal wind, was induced at sufficiently high field strengths. For the purposes of our analysis we would prefer this feature not to manifest itself so that we may focus on the prescribed differential rotation. Indeed there has been little evidence of this in the previous models with the opposite buoyancy and so we shall see whether this feature was an artifact of the prescribed field approach or not.

Changing the sign of the buoyancy means we have changed the sign of the dynamo number, and so we should not necessarily expect to obtain the same values of α_c as for $\Theta_0 = +200$. One should note though that Roberts (1972) does mention a possible link between the values of α_c for opposite parities on flipping the sign of the dynamo number. Indeed, we do follow the trend exhibited by previous models in that the reversed differential rotation promotes dipole instability before quadrupole. The critical onset of the dipole mode is at $\alpha_c = 6.15$, whereas for the quadrupole it is $\alpha_c = 7.70$. In the weakly nonlinear regime the dipole solution takes the familiar form of dynamo waves oscillating about a zero mean. As expected, these waves now travel in the opposite direction to before ie. pole to equator. The evolution throughout one period at $\alpha_0 = 10.0$ can be seen in Figure 4.18 where it should be noted that, except for the differential rotation, the contour intervals are now one half of those in the corresponding situation for $\Theta_0 = +200$ shown in Figure 4.18. The probable explanation is found by inspection of the angular velocity, which now shows a greater region of opposite flux than its earlier counterpart, thus limiting the toroidal field, and, in turn, the meridional field.

At $\alpha_0 = 11.2$, the dipole branch becomes unstable, however, the subsequent evolution is completely different than for the negative buoyancy. Instead of undergoing a symmetry breaking bifurcation, the solution jumps to a separate pure parity

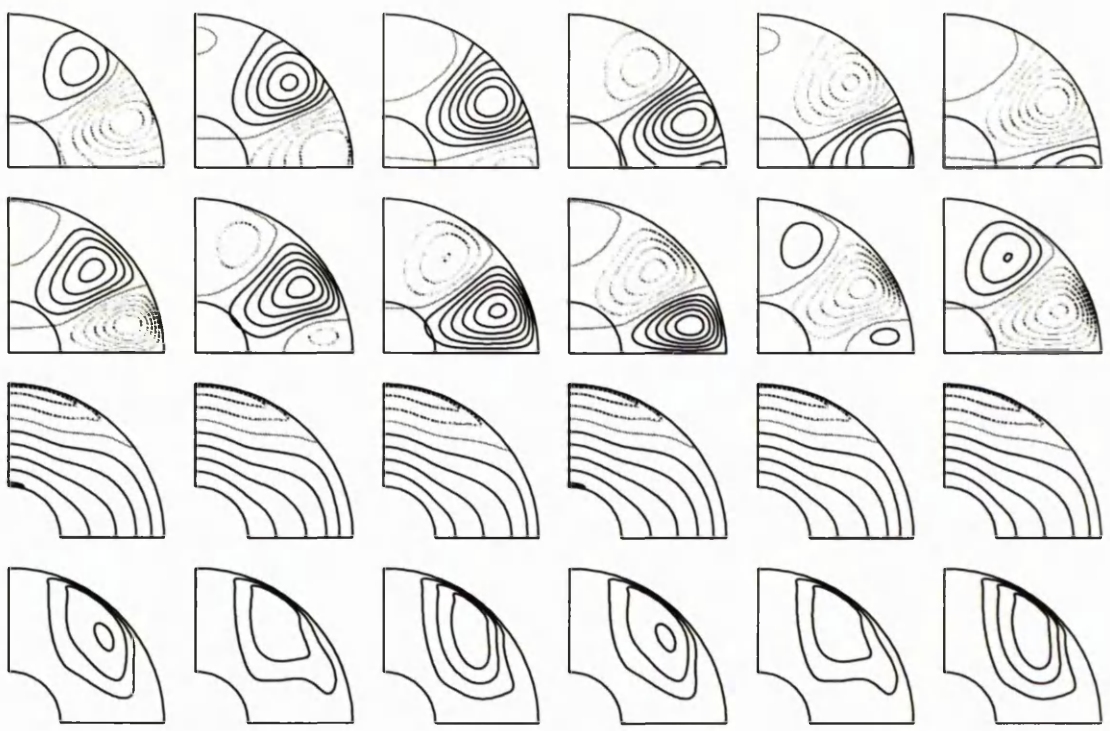

Figure 4.18: Contour plots of (from top to bottom) $Ar\sin\theta$, B, $v/r\sin\theta$ and $\psi r\sin\theta$ at six evenly spaced points throughout one period at $\alpha_0 = 10.0$. Contour intervals are 0.025, 0.25, 25 and 0.125 respectively.

quadrupole branch. Using this solution as an initial condition, it was possible to return to $\alpha_0 = 10.7$ before losing stability back to the dipole branch. It is possible that we have actually found a subcritical bifurcation, even though it is not in the manner originally envisaged! The dipole branch may undergo a subcritical bifurcation, presumably to an unstable mixed parity solution, which then bifurcates to the pure quadrupole branch, regaining stability in the process. This type of situation could be potentially very important in the context of geomagnetic reversals in which the predominantly dipolar field can become quadrupolar during the reversal process. If a perturbation to the long term dipole field causes it to flip to the quadrupole state, then the removal of the perturbation may cause it to flip back to either the original state or, equally possibly, the reversed state. The quadrupole state observed here has

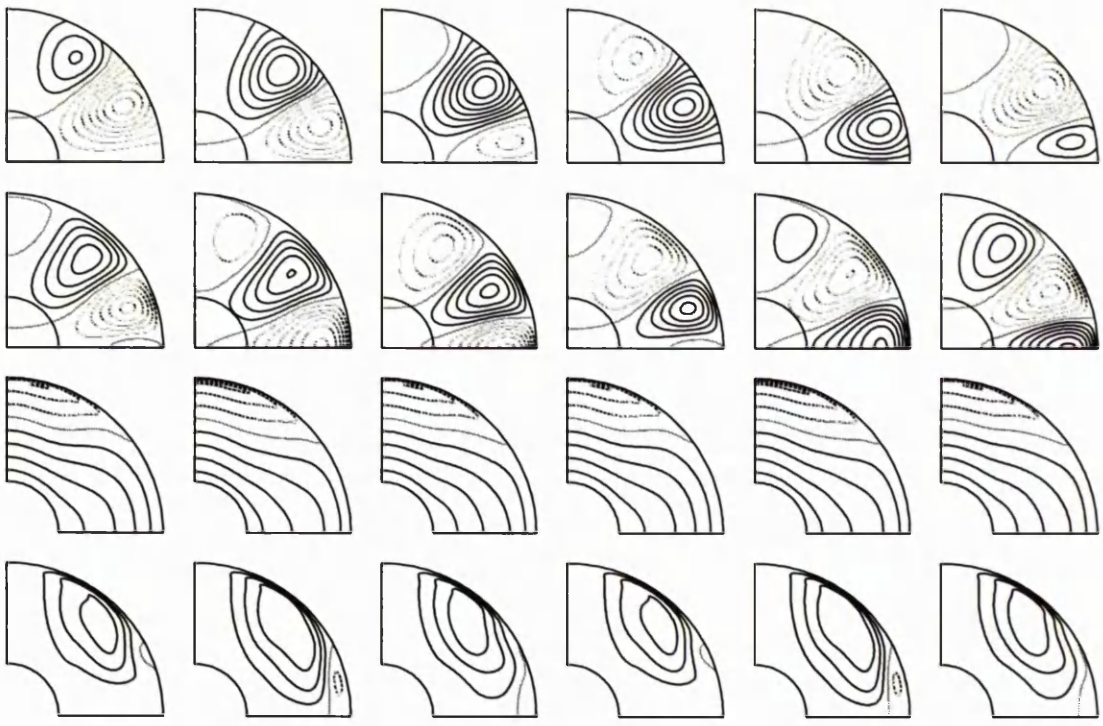

Figure 4.19: Contour plots of (from top to bottom) $Ar\sin\theta$, B, $v/r\sin\theta$ and $\psi r\sin\theta$ at six evenly spaced points throughout one period at $\alpha_0 = 12.0$. Contour intervals are 0.025, 0.25, 25 and 0.125 respectively.

lower energy than the dipole, which also fits the data from reversals. The quadrupole state is very similar to the dipole and can be seen in Figure 4.19 for $\alpha_0 = 12.0$. All the field is still virtually contained outside the inner core and the presence of only the odd harmonics in time induces a flow with half the period.

The equatorial symmetry is eventually broken at $\alpha_0 = 12.5$ to a state that contains only odd harmonics in both dipole and quadrupole parts. For $\Theta_0 = +200$, the sequence of mixed solutions contained a quadrupole part with energy essentially independent of α_0, corresponding to the energy of the pure parity state prior to the bifurcation. Here, for $\Theta_0 = -200$, we also observe growth of the dipole energy alone as α_0 is increased although the quadrupole energy is not equal to that before the bifurcation. This is outlined in Figure 4.20 which shows the quadrupole contribution to the energy

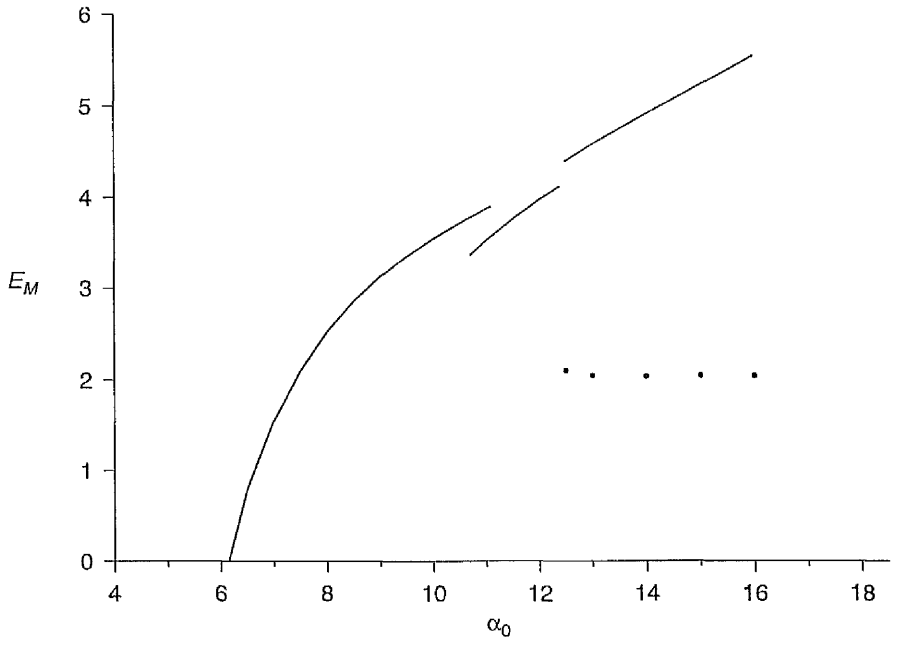

Figure 4.20: E_M vs. α_0 for Θ_0=-200. The quadrupole contribution to the energy in the mixed regime is shown by bullet points.

as bullet points. At the point of bifurcation, the energy is distributed evenly between the two parities suggesting an equipartition of energy. This does not persist as α_0 is increased though, with the dipole part increasing linearly with α_0.

A sequence of snapshots of the solution just after the bifurcation is shown in Figure 4.21. Apart from the lack of equatorial symmetry at any given instant of time, the dynamo waves in the magnetic field are much the same as before. The meridional flow shows only a weak symmetry breaking and the angular velocity is almost identical to that at $\alpha_0 = 12.0$. The toroidal flow also does not seem to vary much throughout its periodic cycle which, again, is still half that of the magnetic field.

From Figure 4.20, we see that that global period averaged magnetic energy of the solution at $\alpha_0 = 16.0$ is only 5.54, compared to 17.7 at the equivalent value of α_0 for the opposite buoyancy. It seems that the differing behaviour of the toroidal flow between the two cases is responsible for the difference. To underline this, we show snapshots of the solution at $\alpha_0 = 30.0$ in Figure 4.22, for which the period averaged energy is still

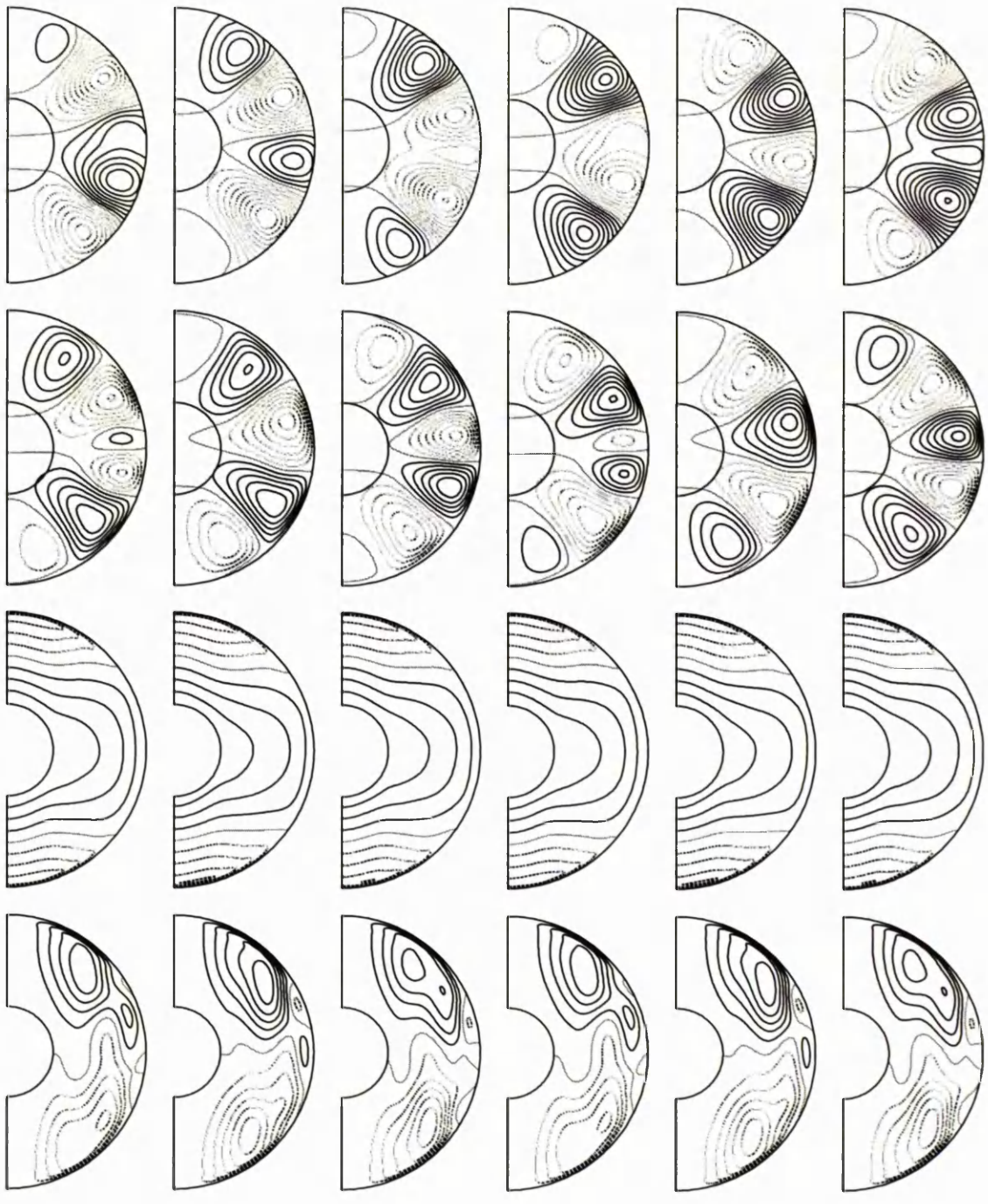

Figure 4.21: Contour plots of (from top to bottom) $Ar\sin\theta$, B, $v/r\sin\theta$ and $\psi r\sin\theta$ at six evenly spaced points throughout one period at $\alpha_0 = 14.0$. Contour intervals are 0.025, 0.25, 25 and 0.125 respectively.

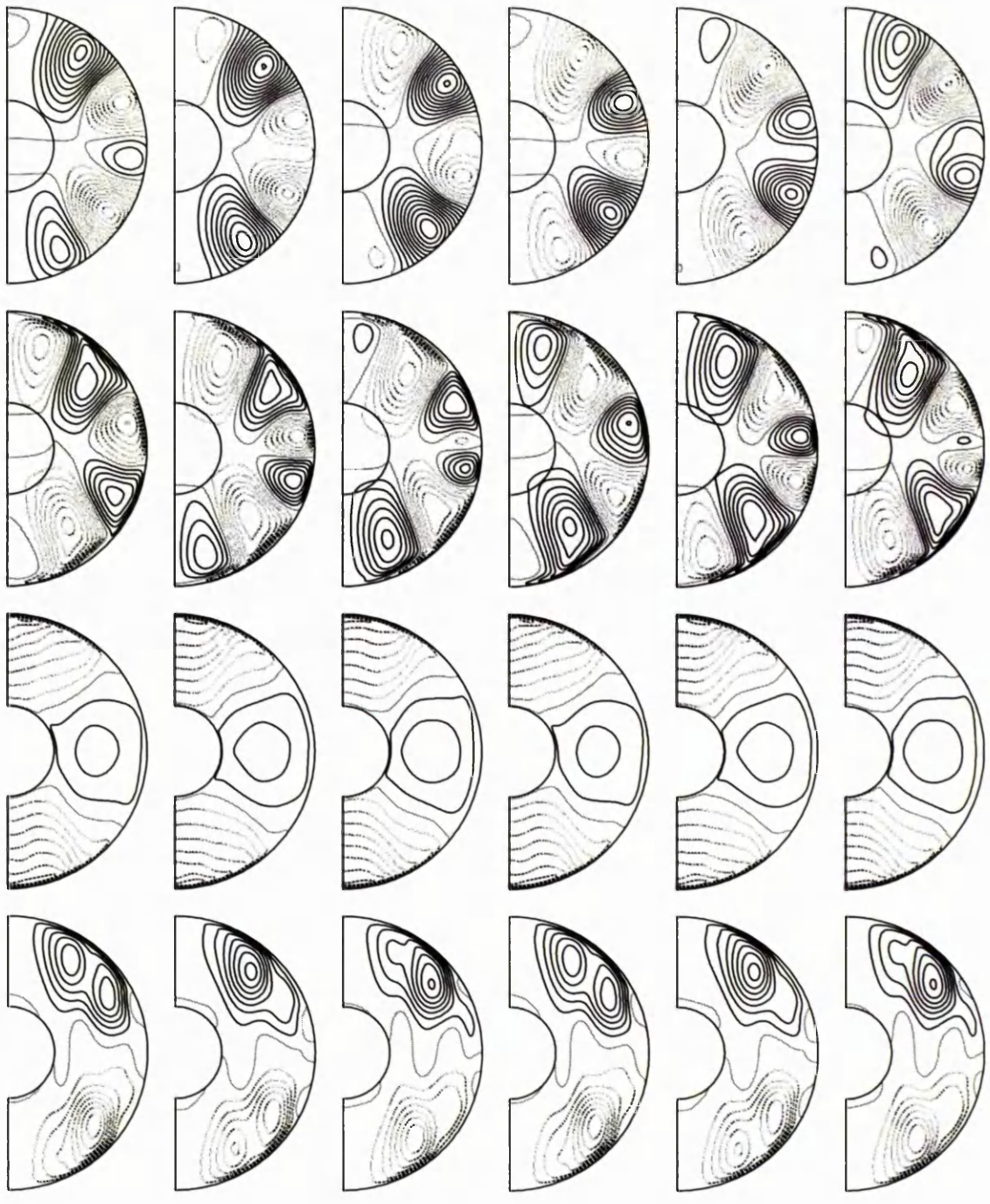

Figure 4.22: Contour plots of (from top to bottom) $Ar\sin\theta$, B, $v/r\sin\theta$ and $\psi r\sin\theta$ at six evenly spaced points throughout one period at $\alpha_0 = 30.0$. Contour intervals are 0.05, 0.25, 25 and 0.25 respectively.

only 13.8. The figure clearly shows that the thermal wind has been completely dwarfed by the magnetic wind generated by the dynamo waves. The contour intervals for the meridional field and flow have both been doubled but the zonal values are unchanged. Even with this change, the meridional field still has more contours than before, and so, one can see that in this regime, increasing α_0 has little effect on the (still dominant) toroidal field. The interaction of magnetic and thermal winds is pushing the system away from the strong field regime towards the weak field regime where poloidal and toroidal parts are comparable.

That the magnetic wind opposes the thermal wind in this case, and not for the other, is not surprising in the weakly nonlinear limit. We know that, despite the linear eigenfunctions having different parities, the overall structure is usually very similar and so the generated magnetic wind should therefore be similar. What we have shown here is that this similarity can persist into the strongly nonlinear regime and thereby change the evolution of the two systems entirely as α_0 is increased. Unfortunately, this has the effect of making a nonaxisymmetric linear analysis more or less redundant, since we were hoping to study the effect of some negative gradient differential rotation.

A quick linear analysis was made despite the above objections, and revealed that no modes were unstable at $\alpha_0 = 30.0$, although $m = 1$ was the least stable. At $\alpha_0 = 64.0$ the period averaged energy is ~ 49 and a truncation test was carried out which revealed no serious problems. Despite the high energy present in the basic state, no instabilities were found. It was not until $\alpha_0 \sim 75$ that instability was observed, and even then not in the manner expected. The modes that showed growth were with azimuthal wavenumbers of order 10 with the lower modes coming in gradually as α_0 was increased. At $\alpha_0 \sim 120$, the $m = 1$ mode eventually became unstable but a lack of time has unfortunately prevented a full analysis of what is going on here. Since the truncation test shows no problem at $\alpha_0 = 64.0$, it would appear these results are genuine, but one would like to be definite given the strange behaviour observed.

Clearly a nonaxisymmetric run is out of the question since we would have to include an extremely large number of azimuthal modes to be able to resolve the fine structures which would inevitably appear.

We have already seen the way in which the magnetic wind produced in this particular model alters the thermal wind profile beyond all recognition in contrast to the previous two models. It is therefore not surprising to see different behaviour, although one would hardly have expected the sharp contrast we have found. We would be able to gain a better understanding of the system by running more models at yet more values of Θ_0, but the codes are still sufficiently CPU intensive to make that a difficult task.

Chapter 5

Magnetic Stability: Conclusions

In the previous two chapters we have studied a mean field dynamo model including a prescribed buoyancy, for three different parameter values and an equivalent model without the buoyancy where the α effect regenerates the whole field. We will now bring together the results of all four studies and discuss the main points of interest.

The first aim of the study was to examine the magnitude of axisymmetric field one must have in a spherical geometry in order to obtain nonaxisymmetric instabilities. Table 5.1 summarises the critical parameter values associated with the onset of the first nonaxisymmetric mode.

Θ_0	0	+200	+400	-200
α_0	13.1	12.8	4.31	~ 75
m	3	1	1	O(10)
E_M	32.0	13.73	18.9	~ 61
Λ	28.3	61.2	30.9	~ 41
Λ'	4.53	1.94	2.67	~ 8.6

Table 5.1: Critical parameter values for the four different models attempted. The α^2 model is denoted by $\Theta_0 = 0$.

From a general point of view it would seem that instability typically ensues when $\Lambda \sim O(10)$ and when $\Lambda' \sim O(1)$. This agrees with the work of Zhang & Fearn (1994, 1995) who studied the instabilities of imposed toroidal and poloidal decay modes separately. In our α^2 model we were able to study a dynamo with toroidal and poloidal fields comparable, whereas the "$\alpha\omega$" model gave dominant toroidal fields. For the

latter, Λ_c is slightly higher although Λ'_c is actually lower. It is difficult to reconcile the results with and without the buoyancy term, but one must bear in mind that the two models differ fundamentally in that one is steady state (as was the Zhang & Fearn work) and one is oscillatory. It would appear that the time dependence can produce noticeably different results. For example, the axisymmetric field produced by the α^2 model is clearly a highly localised one, whereas the oscillatory field appears less so. Despite this, the difference between Λ and Λ' is actually more for the periodic solutions. Also, the nonaxisymmetric instabilities produced by the oscillatory states always showed a tendency to concentrate within the tangent cylinder, while the steady state field filled the whole shell.

If we compare the $\Theta_0 = 200$ solution with the one having twice the buoyancy, we can make a better comparison. There is less localisation in the $\Theta_0 = 400$ solution and so Λ decreases leaving us with Λ' as the more appropriate measure. The effect of doubling the predominantly positive gradient differential rotation, is to stabilise the system as previously noted by Ogden & Fearn (1995). Of course since our model is allowed to find its own natural equilibration, without the artificiality of including a prescribed field, we end up with a differential rotation which is not exactly increasing with cylindrical radius everywhere. This makes it difficult to compare accurately on a quantitative level but the broad stabilising feature of the differential rotation has been demonstrated.

For the case where $\Theta_0 = -200$ the interaction of the thermal wind and the magnetic wind unfortunately produced a flow of little interest. Inside the tangent cylinder the gradient of the angular velocity with respect to the cylindrical radius is quite small, with the contours being nearly aligned on planes of constant z. Given the tendency of all our oscillatory solutions to have their instabilities concentrated within this region, this is perhaps one of the reasons that this particular model failed to produce the expected behaviour.

Another issue raised by Zhang & Fearn was the direction of propagation of the instabilities. It was their conclusion that this quantity could be strongly influenced by small effects like changing the inner core radius slightly or even simply small changes in the basic state field. For the α^2 model the $m = 3$ mode propagates eastward, but we only ever obtain westward propagating waves when the buoyancy is included. It is difficult to say without studying more models, but it may be the case that the introduction of time dependence favours westward drifting modes. This could have important implications for the geomagnetic field, which is known to have a westwardly drifting nonaxisymmetric component.

The second aim of our study was to examine the possibility of subcritical solutions at the point of azimuthal symmetry breaking. Regardless of whether the basic state was steady or oscillatory there was no evidence for subcriticality in any of the models studied. We did, however, find evidence of a subcritical axisymmetric bifurcation in our last model. This bifurcation allows a dipole solution to temporarily change to a weakened quadrupole state, with the possibility of returning to a reversed dipole solution. This may be more relevant than the bifurcations we were originally trying to find.

Lastly, we also looked at how the instabilities could affect the basic state once they were allowed to evolve and equilibrate at finite amplitude. In all cases the basic state did not undergo any radical change but it was clear that the instabilities were able to draw more energy in the oscillatory solutions than for the steady state. This may be related to the fact that the α^2 model produced an $m = 3$ instability first rather than the $m = 1$ mode of the other models. For the oscillatory models, the azimuthal dependence of the whole solution within the core was not just dominated by $m = 0$ and $m = 1$ but by some of the higher modes as well. This is unlikely to be observed at the Earth's surface, however, since there was virtually no penetration of our nonaxisymmetric fields into the mantle.

Appendix A

Numerical method for solving the Inertial Mode problem

In Chapter 2 the problem of solving the momentum equation for inertial modes was tackled by first employing the poloidal-toroidal decomposition for the flow, $\mathbf{u}$, and then expanding the resulting defining scalars, e and f, in terms of spherical harmonics. The result of this process is the set of equations (2.6a,b) for the radial functions $e_n(r)$ and $f_n(r)$ as defined in the main text. Also shown, in eqs(2.8a,2.8b) were the boundary conditions for the two cases no-slip and stress free, expressed in terms of these radial functions.

A.1 Constructing the matrix system

If one applies the recursion relations (see Abramowitz & Stegun (1965)) given by,

$$\sin\theta \frac{dP_{n_i}^{(m)}}{d\theta} = \frac{n_i(n_i-m+1)}{2n_i+1} P_{n_i+1}^{(m)} + \frac{(n_i+m)(n_i+1)}{2n_i+1} P_{n_i-1}^{(m)} \tag{A.1a}$$

$$\cos\theta P_{n_i}^{(m)} = \frac{n_i-m+1}{2n_i+1} P_{n_i+1}^{(m)} + \frac{n_i+m}{2n_i+1} P_{n_i-1}^{(m)} \tag{A.1b}$$

to eqs(2.6a,b), then the angular dependence can now be separated out. Also, since we have imposed an equatorial symmetry, note that, for even m, eq(2.6a) only involves P's of even degree and eq(2.6b) P's of odd degree. For odd m the situation is reversed. If one focuses on that part of eq(2.6a) which has an angular dependence of $P_{n_1}^{(m)}$ with

$$\begin{bmatrix} X & X & & & & & & \\ X & X & X & & & & & \\ & X & X & X & & & & \\ & & X & X & X & & & \\ & & & X & X & X & & \\ & & & & X & X & X & \\ & & & & & X & X & \\ & & & & & & X & X \end{bmatrix} \begin{bmatrix} e_1 \\ f_1 \\ e_2 \\ f_2 \\ e_3 \\ f_3 \\ e_4 \\ f_4 \end{bmatrix} = \tilde{\omega} \begin{bmatrix} X & & & & & & & \\ & X & & & & & & \\ & & X & & & & & \\ & & & X & & & & \\ & & & & X & & & \\ & & & & & X & & \\ & & & & & & X & \\ & & & & & & & X \end{bmatrix} \begin{bmatrix} e_1 \\ f_1 \\ e_2 \\ f_2 \\ e_3 \\ f_3 \\ e_4 \\ f_4 \end{bmatrix}$$

Figure A.1: An outline of the structure of the block matrix problem obtained from eqs(2.6a,b). Each X represents a further matrix that implements the radial structure (see Figure A.2).

$n_1 = 2n' + m - 2$, then the radial functions which will be selected are just $e_{n=n'}$, $f_{n=n'}$ and $f_{n=n'-1}$. Thus the effect of the Coriolis force is to couple the angular modes, precluding the possibility of solving for each mode separately. In the case of eq(2.6b), an angular dependence of $P_{n_2}^{(m)}$ now picks out the functions $f_{n=n'}$, $e_{n=n'}$ and $e_{n=n'+1}$ where $n_2 = 2n' + m - 1$.

If we express the sequence of functions $e_1, e_2, e_3, \ldots$ and $f_1, f_2, f_3, \ldots$ as the vector $(e_1, f_1, e_2, f_2, \ldots)$ then what we have shown above is that for each angular mode the functions e and f only couple to their nearest neighbours. This suggests the schematic form shown in Figure A.1 for a matrix solution to the problem. This is the visualisation of the system $\mathbf{Av} = \tilde{\omega}\mathbf{Bv}$ introduced in eq(2.9) where $\mathbf{v}$ is the vector of e's and $f's$ defined above. Within each of the blocks will be the details of how to solve the radial structure which we will turn to in a moment. One should note that the boundary conditions, as given in eqs(2.8a,2.8b), are not coupled in the angular co-ordinate and so may be included quite easily in the structure outlined. Despite the two matrices having dimension N^2, their banded structure means we only have to store $3N - 2$ blocks for $\mathbf{A}$ and N blocks for $\mathbf{B}$ ie. the storage is only linear in N.

To solve for the radial structure of each angular mode we adopt an expansion in

Chebyshev polynomials for the functions e_n and f_n as follows:

$$e_n(r) = \sum_{k=1}^{K+2} e_{kn} T_{k-1}(x) \quad , \quad f_n(r) = \sum_{k=1}^{K+4} f_{kn} T_{k-1}(x) \tag{A.2}$$

where $x \in [-1, 1]$ and is linearly related to r by,

$$r = \frac{r_o + r_i}{2} + \frac{r_o - r_i}{2} x \tag{A.3}$$

The radius ratio was kept fixed at 1/3 so the only values of r_i and r_o actually used were 1/2 and 3/2 respectively. The reason for the top limits of the sums not simply being K will become apparent shortly.

Each e_n in the vector $\mathbf{v}$, now corresponds to the vector of spectral coefficients, $(e_{1n}, e_{2n}, e_{3n}, \ldots)$. Similarly for each f_n. To enable us to construct the structure within each block in the matrices $\mathbf{A}$ and $\mathbf{B}$, we must now discretise in radius as well. This is done by solving the equations at a finite set of collocation points in r. These points are taken to be the K zeroes of T_K. When using a Chebyshev expansion, one can show that these will be the most efficient choice of collocation points in terms of accuracy. One should also note that the zeroes of Chebyshev polynomials are concentrated towards $x = \pm 1$ giving better resolution in the boundary layers. Typically, this is a good thing from a fluid dynamical point of view, but of course in this study we are interested in shear layers throughout the entire body of the fluid, and so this effect may not be as beneficial as in other studies. However, if one recalls the various scalings of the shear layer widths with Ekman number (see Figure 1.1), one can see that the Ekman layers should still be the thinnest.

The structure of the blocks is now apparent. The blocks multiplying e's are square matrices of dimension $K + 2 \times K + 2$ whereas those multiplying f's have dimension $K + 4 \times K + 4$. The first K rows of each block correspond to the equations evaluated at each of the K collocation points whilst the $K + 2(4)$ columns correspond to the $K + 2(4)$ Chebyshev polynomials in the expansions. The reason for extending the

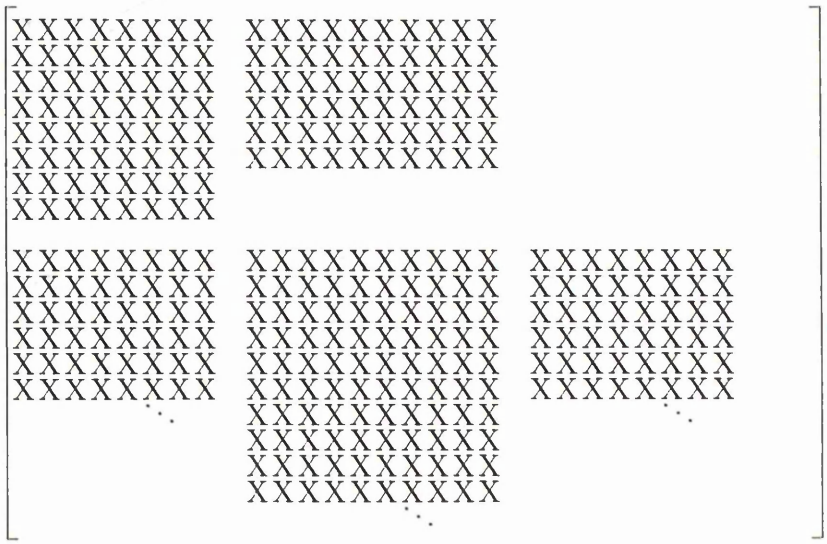

Figure A.2: The composition of the blocks that comprise the matrix **A**. The example illustrates the first two block rows for the case $K = 6$.

blocks by 2 for the e's and 4 for the f's was to accommodate the boundary conditions. The last two(four) rows contain the Chebyshev expansions of eq(2.8a) or eq(2.8b) at $x = \pm 1$. Since the boundary conditions are uncoupled in the angular co-ordinate, only the blocks on the main diagonal in **A** are used. The last two(four) rows in the off-diagonal blocks are set equal to zero. An outline of the structure for the case of the tri-diagonal matrix **A** is shown in Figure A.2.

It should be noted that although the equations have been derived for a general value of m, there is a slight problem when evaluating $m = 0$. In this case the value of n_1 is 0, which is not one of the angular modes included in our spherical harmonic expansions since it disappears after applying the curl operator. This in itself is not a problem, however, the fact that the first leading diagonal blocks in both **A** and **B** are then zero, is. To circumvent this, for the case $m = 0$, the first leading diagonal block in **A** is set equal to the identity matrix.

A.2 Inverse iteration

The matrix eigenvalue problem was solved using inverse iteration. A brief outline of the technique is given here. Denote the individual eigenvalues and eigenvectors of the system as λ_i and $\mathbf{v}_i$ respectively. We then have that

$$\mathbf{A}\mathbf{v}_i = \lambda_i \mathbf{B}\mathbf{v}_i \quad \text{for each } i, \tag{A.4}$$

or, equivalently,

$$\lambda_i^{-1}\mathbf{v}_i = \mathbf{A}^{-1}\mathbf{B}\mathbf{v}_i \quad \text{for each } i. \tag{A.5}$$

A general solution of the system can be expressed as a sum of the eigenvectors

$$\mathbf{v} = \sum_i c_i \mathbf{v}_i \tag{A.6}$$

and so acting successively on $\mathbf{v}$ with $\mathbf{A}^{-1}\mathbf{B}$ gives,

$$(\mathbf{A}^{-1}\mathbf{B})^p \mathbf{v} = \sum_i c_i \lambda_i^{-p} \mathbf{v}_i \tag{A.7}$$

As $p \to \infty$, the summation on the right will be dominated by the pth power of the largest λ_i^{-1} ie. the smallest λ_i. Denote this particular λ by λ_s. Also, let v stand for any of the components of the vector $\mathbf{v}$ and $v^{(p)}$ be the pth iterate of v produced by the above process. Then,

$$v^{(p)} \to c_s \lambda_s^{-p} v_s \text{ as } p \to \infty \tag{A.8}$$

and

$$\begin{aligned} \frac{v^{(p+1)}}{v^{(p)}} &= \frac{\lambda_1^{-1}(c_1\lambda_1^{-p}v_1) + \lambda_2^{-1}(c_2\lambda_2^{-p}v_2) + \ldots + \lambda_s^{-1}(c_s\lambda_s^{-p}v_s) + \ldots}{c_1\lambda_1^{-p}v_1 + c_2\lambda_2^{-p}v_2 + \ldots + c_s\lambda_s^{-p}v_s + \ldots} \\ &\to \frac{\lambda_s^{-1}(c_s\lambda_s^{-p}v_s)}{c_s\lambda_s^{-p}v_s} \\ &= \lambda_s^{-1} \text{ as } p \to \infty \end{aligned} \tag{A.9}$$

Hence the iteration procedure yields both the eigenvector and the eigenvalue. In our case the matrix $\mathbf{A}$ is actually of the form $\mathbf{C} + \lambda_0 \mathbf{B}$, where λ_0 then takes on the form of a guess at the actual eigenvalue. Successive iterations will then converge to the eigenvector with eigenvalue closest to the guess ie. with the smallest correction λ_s. In practice we used NAG routine F01NAF to obtain the LU decomposition of $\mathbf{A}^{-1}\mathbf{B}$, followed by repeated calls to routine F04NAF for each iterate.

Appendix B

Numerical method for solving the equations of mean-field MHD

In Chapter 2 the governing equations of mean-field MHD were outlined. The system of equations (3.9 – 3.13) represents a much bigger challenge than the eigenvalue problem of the inertial mode analysis. However, as we will show later, we can actually re-use a large part of the method outlined in Appendix A when solving the momentum equation. After applying the poloidal-toroidal decomposition to the magnetic field, as we did with the flow, we are left with equations (3.16,3.19) for the radial functions g, $\hat{g}$, h and $\hat{h}$. Let us deal with these four scalars first and we shall return to the momentum equation later.

Both inner and outer core induction equations are predictive and so we will need to use some sort of time-stepping procedure to advance them in time. As they stand, eqs(3.16,3.19) involve radial functions, albeit with an implicit time dependence, and so we use the same technique as in the inertial mode analysis to discretise in r ie. Chebyshev expansions. For the field in the outer core these take on exactly the same form as in eq(A.2),

$$g_{lm}(r,t) = \sum_{k=1}^{KB+2} g_{klm}(t) T_{k-1}(x) \quad , \quad h_{lm}(r,t) = \sum_{k=1}^{KB+2} h_{klm}(t) T_{k-1}(x) \tag{B.1}$$

with the same linear map between r and x. The first of two minor differences is that we now denote the angular index by l, since we are including the full symmetry ($P_l^{(m)}$

being the standard notation) and the subscript on g/h corresponds to the degree of the associated Legendre function associated with it. The second difference is that the top limits of both sums are $KB+2$ to accommodate the boundary and matching conditions for the field as we shall see shortly. Since the time dependence is no longer explicitly separated out, the spectral coefficients are now time dependent. For future reference the functions g_{lm} and h_{lm} will sometimes be referred to as radial functions even though they do have the implicit time dependence.

For the corresponding inner core functions there is one extra complication though, which prevents us from simply writing down the same expansions as in eq(B.1) – namely the inclusion of the origin when dealing with the inner core field. When a vector is expressed in spherical polar co-ordinates it turns out that its components must satisfy certain symmetry conditions. These conditions will not be derived here but see the appendix of Kerswell & Davey (1995) in which their concluding statement as applied to our variables is,

$$\hat{g}_{lm}(-r,t) = -(-1)^l \hat{g}_{lm}(r,t) \quad , \quad \hat{h}_{lm}(-r,t) = -(-1)^l \hat{h}_{lm}(r,t) \quad , \quad \forall t \qquad \text{(B.2)}$$

Clearly, whatever Chebyshev expansions we choose should satisfy these expansions. One should note that these symmetries apply equally to the outer core functions g and h, but since the origin of our Chebyshev expansion ($x=0$) was located in the middle of the gap, the issue does not arise. Here, the most natural choice is to map $r=[0,r_i]$ onto $\hat{x}=[0,1]$ and so the physical origin coincides with the expansion origin. To incorporate the symmetries given by eq(B.2), we adopt the following expansions in the inner core,

$$\hat{g}_{lm}(r,t) = \sum_{k=1}^{KBI+1} \hat{g}_{klm}(t) T_{2k-1}(\hat{x}) r^{l'} \quad , \quad \hat{h}_{lm}(r,t) = \sum_{k=1}^{KBI+1} \hat{h}_{klm}(t) T_{2k-1}(\hat{x}) r^{l'} \qquad \text{(B.3)}$$

where $l'=1$ if l is odd, and 2 if l is even. The linear map between r and $\hat{x}$ is simply $r=r_i\hat{x}$. The number of spectral coefficients for each l is $KBI+1$ where KBI can

be varied independently of the outer core truncation KB. In practice though, we always took $KBI = KB/2$ to give equal resolution in both cores. To complete the discretisation in r we enforce the equations at collocation points in the same manner as in Appendix A. For the outer core we used the KB zeroes of $T_{KB}(x)$ on $x = [-1, 1]$, and for the inner core we used the KBI zeroes of $T_{2KBI+1}(\hat{x})$ on $\hat{x} = (0, 1]$. In the case of the inner core, the fact that we are only working on [0,1] means that we are not wasting resolution on the origin, but can still resolve better than average at the inner core boundary.

B.1 Time-stepping method

The time-stepping procedure is implemented via a second order accurate Runge-Kutta method which has been modified to treat the diffusive terms implicitly. The process consists of a predictor step and then a corrector step. We will only outline the method for the coefficients, g_{klm} and $\hat{g}_{klm}$, the h_{klm} and $\hat{h}_{klm}$ coefficients proceeding in an identical manner. The predictor step involves firstly calculating the nonlinear forcing term $\mathbf{e}_r.\nabla \times \nabla \times (\mathbf{u} \times \mathbf{B} + \alpha \mathbf{B})$ in the outer core at each collocation point. We will discuss how this is done after we have established the details of the time-stepping procedure. For now, denote the result of the calculation as DG_j where $j = 1, KB$ is an index of the collocation points. We approximate time derivatives, $\frac{\partial}{\partial t}$, and diffusion operators, L_l, by the following,

$$\frac{\partial Z_{klm}}{\partial t} \sim \frac{Z_{klm}^{n+1} - Z_{klm}^{n}}{\Delta t} \quad , \quad L_l Z_{klm} \sim \frac{\Delta t}{2} L_l \left(\frac{Z_{klm}^{n+1} + Z_{klm}^{n}}{\Delta t} \right) \tag{B.4}$$

where a superscript n denotes the nth timestep. Eq(3.16a) can then be rewritten as

$$\sum_{k=1}^{KB+2} \frac{l(l+1)}{r_j^2} \left[(\tilde{g}_{klm}^{n+1} - g_{klm}^{n}) - \frac{\Delta t}{2} L_l (\tilde{g}_{klm}^{n+1} + g_{klm}^{n}) \right] T_{k-1}(x)|_{x=x_j} = \Delta t DG_j \tag{B.5a}$$

for each collocation point, x_j, and for each degree and order of the spherical harmonics. This formulation gives us the preliminary outer core coefficients $\tilde{g}_{klm}^{n+1}$. The

corresponding coefficients for the inner core are obtained via,

$$\sum_{k=1}^{KBI+1} \frac{l(l+1)}{r_j^2}\left[(\tilde{\hat{g}}_{klm}^{n+1} - \hat{g}_{klm}^{n}) - \frac{\Delta t}{2}L_l(\tilde{\hat{g}}_{klm}^{n+1} + \hat{g}_{klm}^{n})\right]\left(r^{l'}T_{2k-1}(\hat{x})\right)\Big|_{\hat{x}=\hat{x}_j} \qquad \text{(B.5b)}$$
$$= \Delta t\hat{DG}_j = -\Delta t\, im\Omega_{ic}\,\hat{g}_{lm}^{*n}(r_i\hat{x}_j)$$

The corrector step then uses the preliminary coefficients to reevaluate the forcings. These forcings are then weighted with the original evaluations to produce a more accurate value for g_{klm}^{n+1} and $\hat{g}_{klm}^{(n+1)}$ as follows,

$$\sum_{k=1}^{KB+2} \frac{l(l+1)}{r_j^2}\left[(g_{klm}^{n+1} - g_{klm}^{n}) - \frac{\Delta t}{2}L_l(g_{klm}^{n+1} + g_{klm}^{n})\right]T_{k-1}(x)|_{x=x_j} = \frac{\Delta t}{2}(\tilde{DG}_j + DG_j) \qquad \text{(B.6a)}$$

$$\sum_{k=1}^{KBI+1} \frac{l(l+1)}{r_j^2}\left[(\hat{g}_{klm}^{n+1} - \hat{g}_{klm}^{n}) - \frac{\Delta t}{2}L_l(\hat{g}_{klm}^{n+1} + \hat{g}_{klm}^{n})\right]\left(r^{l'}T_{2k-1}(\hat{x})|_{\hat{x}=\hat{x}_j}\right) \qquad \text{(B.6b)}$$
$$= \frac{\Delta t}{2}(\tilde{\hat{DG}}_j + \hat{DG}_j) = -\frac{\Delta t\, im\Omega_{ic}}{2}(\tilde{\hat{g}}_{lm}^{*n+1}(r_i\hat{x}_j) + \hat{g}_{lm}^{*n}(r_i\hat{x}_j))$$

In matrix notation, eqs(B.5, B.6) can be succinctly written as

$$\mathbf{X}\tilde{\mathbf{g}}^{n+1} = \mathbf{Y}\mathbf{g}^{n} + \Delta t\mathbf{DG} \qquad \text{(B.7a)}$$

$$\mathbf{X}\mathbf{g}^{n+1} = \mathbf{Y}\mathbf{g}^{n} + \frac{\Delta t}{2}(\tilde{\mathbf{DG}} + \mathbf{DG}) \qquad \text{(B.7b)}$$

where

$$\mathbf{g}^{n} = [g_{1lm}^{n}, g_{2lm}^{n}, \ldots, g_{KB+2\,lm}^{n}, \hat{g}_{1lm}^{n}, \hat{g}_{2lm}^{n}, \ldots, \hat{g}_{KBI+1\,lm}^{n}]^T \qquad \text{(B.8a)}$$

$$\mathbf{DG} = [DG_{1lm}^{n}, DG_{2lm}^{n}, \ldots, DG_{KB\,lm}^{n}, 0, 0, \hat{DG}_{1lm}^{n}, \hat{DG}_{2lm}^{n}, \ldots, \hat{DG}_{KBI\,lm}^{n}, 0]^T \qquad \text{(B.8b)}$$

and the square matrices $\mathbf{X}$ and $\mathbf{Y}$ have dimension $KB + KBI + 3 = KBDIM$. The structure of the system is outlined in Figure B.1.

$$\begin{bmatrix} X & X & X & X & X & X & X & X & & \\ X & X & X & X & X & X & X & X & & \\ X & X & X & X & X & X & X & X & & \\ X & X & X & X & X & X & X & X & & \\ X & X & X & X & X & X & X & X & & \\ X & X & X & X & X & X & X & X & & \\ X & X & X & X & X & X & X & X & & \\ X & X & X & X & X & X & X & X & X & X & X & X \\ X & X & X & X & X & X & X & X & X & X & X & X \\ & & & & & & & & X & X & X & X \\ & & & & & & & & X & X & X & X \\ & & & & & & & & X & X & X & X \end{bmatrix} \begin{bmatrix} g_{1lm} \\ g_{2lm} \\ g_{3lm} \\ g_{4lm} \\ g_{5lm} \\ g_{6lm} \\ g_{7lm} \\ g_{8lm} \\ g_{1lm} \\ \hat{g}_{2lm} \\ \hat{g}_{3lm} \\ \hat{g}_{4lm} \end{bmatrix} = \begin{bmatrix} X & X & X & X & X & X & X & X & & \\ X & X & X & X & X & X & X & X & & \\ X & X & X & X & X & X & X & X & & \\ X & X & X & X & X & X & X & X & & \\ X & X & X & X & X & X & X & X & & \\ X & X & X & X & X & X & X & X & & \\ & & & & & & & & X & X & X & X \\ & & & & & & & & X & X & X & X \\ & & & & & & & & X & X & X & X \end{bmatrix} \begin{bmatrix} g_{1lm} \\ g_{2lm} \\ g_{3lm} \\ g_{4lm} \\ g_{5lm} \\ g_{6lm} \\ g_{7lm} \\ g_{8lm} \\ g_{1lm} \\ \hat{g}_{2lm} \\ \hat{g}_{3lm} \\ \hat{g}_{4lm} \end{bmatrix} + \begin{bmatrix} DG_{1lm} \\ DG_{2lm} \\ DG_{3lm} \\ DG_{4lm} \\ DG_{5lm} \\ DG_{6lm} \\ 0 \\ 0 \\ \hat{DG}_{1lm} \\ \hat{DG}_{2lm} \\ \hat{DG}_{3lm} \\ 0 \end{bmatrix}$$

Figure B.1: The structure of the time-stepping matrices associated with the spherical harmonic $P_l^{(m)} e^{im\phi}$ for the radial function g when the truncations are $KB = 6$ and $KBI = 3$. The first subscript on g represents the index in the Chebyshev expansion, whereas the first subscript on DG is a collocation point index. The boundary conditions are implemented in rows 7 to 9. Note that inhomogeneous boundary conditions could be imposed by replacing the zeros in the DG vector with appropriate values.

Letting j now run from 1 to $KBDIM$, the contents of the $\mathbf{X}$ and $\mathbf{Y}$ matrices are given by,

$$\mathbf{X}_{jk} = \frac{l(l+1)}{r_j^2}\left[1 - 0.5\Delta t L_l\right] T_{k-1}(x)|_{x=x_j} \tag{B.9a}$$

$$\mathbf{Y}_{jk} = \frac{l(l+1)}{r_j^2}\left[1 + 0.5\Delta t L_l\right] T_{k-1}(x)|_{x=x_j} \tag{B.9b}$$

for $j = 1$ to KB and

$$\mathbf{X}_{jk} = \frac{l(l+1)}{r_j^2}\left[1 - 0.5\Delta t L_l\right] \left(r^{l'} T_{2k-1}(\hat{x})|_{\hat{x}=\hat{x}_j}\right) \tag{B.9c}$$

$$\mathbf{Y}_{jk} = \frac{l(l+1)}{r_j^2}\left[1 + 0.5\Delta t L_l\right] \left(r^{l'} T_{2k-1}(\hat{x})|_{\hat{x}=\hat{x}_j}\right) \tag{B.9d}$$

for $j = (KB+3)+1$ to $KBDIM$. The three rows of $\mathbf{X}$ at $j = KB+1, 2, 3$ are used to implement firstly the outer boundary condition, eq(3.18), followed by the two matching conditions, eqs(3.20). The corresponding three rows of $\mathbf{Y}$ are set to zero. The contents of both matrices can be precomputed before the computational run since neither changes from one timestep to the next. Furthermore, we can invert $\mathbf{X}$ and premultiply it onto $\mathbf{Y}$ saving even more computational effort.

By setting all entries in the **DG** and **DH** arrays to zero, it is possible to test the timestepping procedure independently of the other parts of the code. With no forcing supplied, all the spectral coefficients should follow a simple free decay evolution. Returning to eqs(3.16,3.19) and expanding the radial functions in terms of spherical Bessel functions, the analytical free decay rates can be obtained. Table B.1 shows both the analytically derived free decay rates and the ratio of the numerically calculated rates to the analytic ones for the the $l = 5$ modes. The results are shown for $\Delta t = 10^{-6}$ and for varying truncation. The equivalent set of results for variation of timestep with $KB = 20$ are shown in Table B.2 where the percentage error is quoted rather than the ratio of numerical and analytic decay rates. We have actually tested the more general case which arises when the ratio, σ, of the conductivities is not equal to one. This introduces only minor modifications to the code, and since we only ever use $\sigma = 1$, we have omitted it from the derivation of the equations. Excellent agreement is obtained for $\Delta t = 10^{-6}$ for fairly low truncations with the variation of timestep highlighting the second order accuracy of the scheme.

	$g_{\sigma=0.1}$	$h_{\sigma=0.1}$	$g_{\sigma=10.0}$	$h_{\sigma=10.0}$
analytic	38.9940319	29.7588808	33.2660269	26.0379254
$KB = 8$	1.00000006	1.00000157	1.00221871	1.00106601
10	1.00000005	0.99999996	1.00052537	1.00020151
12	1.00000000	1.00000000	0.99998076	0.99998200
14	1.00000000	1.00000000	0.99999952	1.00000130
16	1.00000000	1.00000000	0.99999993	0.99999995

Table B.1: The ratio of the numerical decay rates with the analytical rates for $l = 5$ at two different ratios of inner core conductivities, σ. Δt was fixed at 10^{-6}.

	$g_{\sigma=0.1}$		$h_{\sigma=10.0}$	
analytic	38.9940319	% error	26.0379254	% error
$\Delta t = 10^{-3}$	38.9989740	1.27×10^{-4}	26.0393967	5.65×10^{-5}
$\Delta t = 10^{-4}$	38.9940813	1.27×10^{-6}	26.0379402	5.68×10^{-7}

Table B.2: The variation of numerical decay rates with timestep. KB was fixed at 20.

Also, in practice, the routines which evaluated the nonlinear forcings did not ac-

tually return a vector of real space values at collocation points, but instead returned a vector of Chebyshev expansion coefficients in spectral space. Only one matrix multiplication is required to convert to the appropriate real space vector and this can be subsumed into the precomputed value of $\mathbf{X}^{-1}$. To test the real to spectral conversion, a set of examples was constructed which involved specifying a set of radial functions, $g(r), h(r)$ for the magnetic field. Substituting these functions into the left hand sides of eqs(3.16, 3.19), and setting $\frac{\partial}{\partial t} = 0$ gives functional forms of the forcing required for steady states corresponding to the original choices of g and h. Using simple forms for g and h, it was possible to calculate the spectral coefficients for the forcings by hand (details of these expansions will follow shortly). These coefficients were fed in to the code and kept constant throughout the run, which was timestepped from random initial conditions. For each example tried, the solution evolved to the steady state values corresponding to the initial choice of $g(r)$ and $h(r)$.

B.2 Evaluation of nonlinear forcings

In order to advance our system in time we must calculate the contents of the **DG** and **DH** arrays. The parts of these arrays which deal with the inner core are trivial, as can be seen from eqs(B.5b, B.6b), since they only involve reconstructing the inner core radial functions. The outer core parts, however, involve cross products and curl operations, both of which are common to the Lorentz forcing in the momentum equation as well. The same method of evaluation was used in each case and so we will outline how to treat the curl, and the curl of the curl, of a general vector $\mathbf{F}$.

The first issue is how to calculate $\mathbf{F}$ given the spectral coefficients for both the flow and the field. We use a pseudo-spectral method in that we do this by evaluating $\mathbf{u}$, $\mathbf{B}$ and $\nabla \times \mathbf{B}$ in real space. For each spherical harmonic we can easily enough get these three quantities at collocation points in r by simple matrix multiplications. Incidentally, only five quantities are needed to evaluate these terms, all of which can

be precomputed. They are,

$$\frac{1}{r^2}T_{k-1}(x), \quad \frac{1}{r}\frac{d}{dr}T_{k-1}(x), \quad \frac{1}{r}T_{k-1}(x), \quad \frac{1}{r^3}T_{k-1}(x), \quad \frac{1}{r}\frac{d^2}{dr^2}T_{k-1}(x) \tag{B.10}$$

The collocation points used were different than those used in the time-stepping matrices. For dealiasing purposes we took $KN = \frac{3}{2}KB+1$ points which, similarly to before, were the zeroes of $T_{KN}(x)$. The conversion to real space is completed by applying the precomputed angular structures

$$l(l+1)P_l^{(m)}(\cos\theta), \quad \frac{d}{d\theta}P_l^{(m)}(\cos\theta), \quad \frac{1}{\sin\theta}P_l^{(m)}(\cos\theta) \tag{B.11}$$

and

$$\cos(m\phi), \quad \sin(m\phi) \tag{B.12}$$

at appropriate collocation points in θ and ϕ. In ϕ we took 30 evenly spaced points when including 9 azimuthal modes, and in θ we took the $LN = \frac{3}{2}LB + 1$ zeroes of $P_{LN}^{(0)}(\cos\theta)$ where LB was the number of associated Legendre functions included in the expansions.

The cross products $\mathbf{u} \times \mathbf{B}$ and $\nabla \times \mathbf{B} \times \mathbf{B}$ are then calculated pointwise in real space. To evaluate the curls of these quantities we return to spectral space so that we may calculate all the derivatives in terms of the known expansion functions, much as we did when evaluating the field and flow from the poloidal-toroidal decomposition. To do this we need to realise that a vector expressed in spherical polar co-ordinates must be expanded as

$$\begin{aligned}
F_1 &= \sum_{k,l,m} F_1^{klm} T_{k-1}(x) P_l^{(m)}(\cos\theta) e^{im\phi} \\
F_2 &= \sum_{k,l,m} F_2^{klm} T_{k-1}(x) \frac{1}{\sin\theta} P_l^{(m)}(\cos\theta) e^{im\phi} \\
F_3 &= \sum_{k,l,m} F_3^{klm} T_{k-1}(x) \frac{1}{\sin\theta} P_l^{(m)}(\cos\theta) e^{im\phi}
\end{aligned} \tag{B.13a}$$

except for the special case $m = 0$ where the θ and ϕ components are expanded as

$$\begin{aligned} F_2|_{m=0} &= \sum_{k,l} F_2^{kl0} T_{k-1}(x) \sin\theta P_l^{(0)}(\cos\theta) \\ F_3|_{m=0} &= \sum_{k,l} F_3^{kl0} T_{k-1}(x) \sin\theta P_l^{(0)}(\cos\theta) \end{aligned} \tag{B.13b}$$

A Fourier transform in ϕ separates out $\mathbf{F}$ into azimuthal modes and two further matrix multiplications incorporating the expansions above produce the required spectral coefficients. Taking the curl then involves multiplying by more precomputed matrices based on the expansions

$$\frac{1}{r} T_{k-1}(x) \quad , \quad \frac{1}{r}\frac{d}{dr}\Big(r T_{k-1}(x)\Big) \tag{B.14}$$

and

$$\frac{1}{\sin\theta}\frac{d}{d\theta} P_l^{(m)}(\cos\theta), \quad \frac{m}{\sin^2\theta} P_l^{(m)}(\cos\theta), \quad \frac{d}{d\theta} P_l^{(m)}(\cos\theta) \tag{B.15}$$

which again leaves us the different azimuthal modes evaluated in real space in r and θ. If a second curl is required then the same process is repeated over again. Note that all the conversion matrices can actually be multiplied onto one another in the precomputation stage, so that only the bare minimum of effort is actually needed in the code itself. Also, we only need to pass the r-components of the curls to the time-stepping routine, and so, by eq(B.13a), we have automatically got the "correct" spectral coefficients for the angular structure ie. just the spherical harmonics with no extra factors of $\sin\theta$. As explained in the previous section, the matrices that are precomputed for the time-stepping procedure incorporate the necessary spectral to real conversion in r to get back to the original KB collocation points at which the equations are enforced.

The evaluation of the nonlinear forcings was tested by constructing simple examples consisting of spectral coefficients for flow and field. The computer algebra package MAPLE was used to analytically calculate the functional forms of the forcings resulting from these coefficients. The output was then separated by hand into spherical

harmonic components and a simple program written to transform the radial functions into spectral coefficients. The original coefficients for field and flow were then put into the numerical code and a single call to the nonlinear forcing routine was made. All the examples attempted produced output which agreed with that of the analytic results from MAPLE to double precision accuracy.

B.3 Solution of the momentum equation

The induction equation has been solved by stepping the field forward in time, evaluating the $\mathbf{u} \times \mathbf{B}$ term at each timestep. In contrast, since we have decided to ignore inertia, we are diagnostically solving the momentum equation ie. given a field $\mathbf{B}$ we want to invert it for $\mathbf{u}$. To begin with, one substitutes in the poloidal-toroidal decomposition for $\mathbf{u}$ and then expands e and f in a similar way to g and h via

$$e(r,\theta,\phi,t) = \sum_{l,m} e_{lm}(r,t) P_l^{(m)} e^{im\phi} \quad , \quad f(r,\theta,\phi,t) = \sum_{l,m} f_{lm}(r,t) P_l^{(m)} e^{im\phi} \tag{B.16}$$

except that this time around we retain both dipole and quadrupole equatorial symmetries and keep the time dependence implicit. With these expansions we obtain a set of equations not all that different from eqs(2.6a,b) after taking the curl, and curl of the curl, of the momentum equation. These are

$$\begin{aligned} \sum_{l,m} \Bigg\{ & \left[-\frac{2im}{r^2} - El(l+1)L_l \right] e_{lm}(r,t) P_l^{(m)}(\cos\theta) e^{im\phi} \\ & + \frac{2}{r^2}\left[\frac{l(l+1)}{r} - \frac{\partial}{\partial r} \right] f_{lm}(r,t) \sin\theta \frac{d}{d\theta} P_l^{(m)}(\cos\theta) e^{im\phi} \\ & + \frac{2}{r^2} l(l+1) \left[\frac{2}{r} - \frac{\partial}{\partial r} \right] f_{lm}(r,t) \cos\theta \, P_l^{(m)}(\cos\theta) e^{im\phi} \Bigg\} \\ & = \mathrm{e}_r . \nabla \times \mathbf{F} \end{aligned} \tag{B.17a}$$

$$\begin{aligned}\sum_{l,m}\Bigg\{ &\left[\frac{2im}{r^2}+El(l+1)L_l\right]L_l f_{lm}(r,t)P_l^{(m)}(\cos\theta)e^{im\phi} \\ &+\frac{2}{r^2}\left[\frac{l(l+1)}{r}-\frac{\partial}{\partial r}\right]e_{lm}(r,t)\sin\theta\frac{d}{d\theta}P_l^{(m)}(\cos\theta)e^{im\phi} \\ &+\frac{2}{r^2}l(l+1)\left[\frac{2}{r}-\frac{\partial}{\partial r}\right]e_{lm}(r,t)\cos\theta\,P_l^{(m)}(\cos\theta)e^{im\phi}\Bigg\} \\ &= \mathbf{e}_r.\nabla\times\nabla\times\mathbf{F}\end{aligned} \tag{B.17b}$$

where

$$L_l=\frac{\partial^2}{\partial r^2}-\frac{l(l+1)}{r^2} \tag{B.18}$$

The forcing $\mathbf{F}$ consists of the Lorentz force and, in the case of the $\alpha\omega$ dynamo, the imposed buoyancy term. After removing the terms involving complex frequencies from the inertial mode code and replacing them with the new forcing term, we arrive at the modified matrix problem,

$$\mathbf{A}_1\mathbf{v}_1=\mathbf{F}_1 \quad , \quad \mathbf{A}_2\mathbf{v}_2=\mathbf{F}_2 \qquad \text{for each } m. \tag{B.19}$$

There are two separate systems to be solved, corresponding to the two sets of equatorial symmetries that we now have. The matrices $\mathbf{A}_i$ take on the same block tri-diagonal form as before but without the ω_0 term appearing (see Figure A.1). $\mathbf{v}_1$ is exactly as before, with $\mathbf{v}_2$ having the e's and f's swapped round. The forcing vectors, $\mathbf{F}_i$, contain the output from the routine which provides the spectral coefficients of the nonlinear forcing, suitably transformed back to collocation points in r.

The most important difference is in the implementation of the boundary conditions. Since our inner core is free to rotate, we now enforce an inhomogeneous boundary condition at $r=r_i$. . The torque balance given in eq(3.23) is equivalent to

$$-\frac{8\pi}{3}Er_i^4\frac{d}{dr}\left(\frac{1}{r^2}e_{10}\right)\Bigg|_{r=r_i}=\int B_\phi B_r|_{r=r_i}r_i\sin\theta\,dS \tag{B.20}$$

and so all this involves is setting the appropriate entry in $\mathbf{F}_1$ to the value of the magnetic torque. The corresponding row in $\mathbf{A}_1$ is then the Chebyshev expansion of

the quantity on the left hand side. The evaluation of the magnetic torque is discussed in the next section.

The LU decompositions of the $\mathbf{A}_i$, for each m, can be precomputed and again are got from NAG routine F01NAF. During the computational run, all that is required at each timestep are four calls to NAG routine F04NAF to obtain the spectral coefficients for the flow. There is a call for each symmetry class and, of course, each timestep has a predictor and a corrector step. There is no need for an iteration procedure since this is no longer an eigenvalue problem and so is , in fact, simpler than solving for inertial modes.

B.4 Calculating the magnetic torque

Evaluation of the magnetic torque requires the solution of the surface integral on the right hand side of eq(B.20). We could do this using Gaussian quadrature, however, it turns out that it can be simplified into a set of matrix multiplications set purely in spectral space. First of all, note that as far as azimuthal behaviour is concerned, we can ignore all interactions of the form $\cos(m_1\phi)\sin(m_2\phi)$, since these will all integrate to zero regardless of the values of m_1 and m_2. The only integrals to give non-zero contributions are then

$$\int_0^{2\pi} \cos^2 m\phi \, d\phi \quad , \quad \int_0^{2\pi} \sin^2 m\phi \, d\phi \tag{B.21}$$

The multiplicative factors from the ϕ integrals are then just 2π when $m \neq 0$ and π when $m = 0$.

Working through the calculation for the θ contribution, one finds that this only requires the evaluation of one integral that depends on a weighted product of $P_l^{(m)}$'s. When the two Legendre functions have different degrees the integral is zero, simplifying the problem even further. When the degrees are the same we get,

$$\int_0^{\pi} \sin\theta P_l^{(m)} P_l^{(m)} \, d\theta = \frac{2(l+m)!}{(2l+1)(l-m)!} \tag{B.22}$$

So, at any given timestep, we can compute the electromagnetic torque via the expression

$$\begin{aligned} \tau_{EM} = \sum_{l,m} \Big(& TC1_{lm} hc_{lm}(r_i) hs'_{lm}(r_i) \; + \; TC2_{lm} hc_{lm}(r_i) gc_{l+1\,m}(r_i) \\ & + \; TC3_{lm} hc_{lm}(r_i) gc_{l-1\,m}(r_i) \\ & + TS1_{lm} hs_{lm}(r_i) hc'_{lm}(r_i) \; + \; TS2_{lm} hs_{lm}(r_i) gs_{l+1\,m}(r_i) \\ & + \; TS3_{lm} hs_{lm}(r_i) gs_{l-1\,m}(r_i) \Big) \end{aligned} \tag{B.23}$$

where the TCi and TSi arrays can all be precomputed. In the above expression we split the radial functions up into the parts that go as $\cos(m\phi)$ and $\sin(m\phi)$ and denoted these by hc, hs, gc and gs. A prime denotes differentiation with respect to r.

B.5 Calculating the magnetic energy

The energy contained in the magnetic field of the system can be calculated according to (see, for example, Bleaney and Bleaney (1976))

$$E_M = \frac{1}{2\mu_o} \int_V \mathbf{B}.\mathbf{B}\, dV \tag{B.24}$$

We take V to be the volume of the sphere, including both inner and outer cores but excluding the exterior insulator. The nondimensional form is given in eq(3.24). The volume integral was evaluated using Gaussian quadrature with 64 points in θ. The r domain was split into inner and outer cores with 64 points in the outer and 32 points in the inner. When the field was time dependent, the energy was calculated at each timestep and then averaged over one period by a simple trapezoidal approximation. Since the energy is also periodic, this amounts to nothing more than summing up the values at each timestep and then dividing by the total number of timesteps in a period.

As a check on numerical convergence we occasionally calculated the quantity

$$\frac{1}{2} \int_{V_o} \mathbf{u}.\mathbf{u}\, dV \tag{B.25}$$

where V_o denotes the volume of the outer core. One might be tempted to label this the nondimensional kinetic energy of the fluid, but this would be incorrect. The usual definition of kinetic energy is the work done in bringing the fluid to rest. Since we have ignored inertia, no work is required to bring the fluid to rest, and so the above definition, though valid in the limit of vanishing Rossby number, is now somewhat defunct. However, there is no reason for not using it as an acceptable measure of convergence for the fluid. Although the main text only refers to convergence checks on the magnetic field, these were usually backed up by checks on the flow as well.

References

Abdel-Aziz, M.M. & Jones, C.A., 1988. $\alpha\omega$-dynamos and Taylor's constraint. *Geophys. Astrophys. Fluid Dynam.* **44** 117-139.

Abramowitz, M. & Stegun, I.A., 1965. Handbook of Mathematical Functions. Dover, New York.

Acheson, D.J., 1983. Local analysis of thermal and magnetic instabilities in a rapidly rotating fluid. *Geophys. Astrophys. Fluid Dynam.* **27** 123-136.

Anufriev, A.P., Cupal, I. & Hejda, P., 1995. The weak Taylor state in an $\alpha\omega$-dynamo. *Geophys. Astrophys. Fluid Dynam.* **79** 125-145.

Barenghi, C.F., 1993. Nonlinear planetary dynamos in a rotating spherical shell III: $\alpha^2\omega$ models and the geodynamo. *Geophys. Astrophys. Fluid Dynam.* **71** 163-185.

Bondi, H. & Lyttleton, R.A., 1953. On the dynamical theory of the rotation of the Earth. II. The effect of precession on the motion of the liquid core. *Proc. Camb. Phil. Soc.* **49** 498-515.

Braginsky, S.I., 1963. Structure of the F layer and reasons for convection in the Earth's core. *Dokl. Akad. Nauk. SSSR* **149** 1311-1314.

Braginsky, S.I., 1964. Self-excitation of a magnetic field during the motion of a highly conducting fluid. *Zh. Exp. Teor. Fiz. SSSR* **47** 1084-1098.

Braginsky, S.I. & Roberts, P.H., 1995. Equations governing convection in Earth's core and the geodynamo. *Geophys. Astrophys. Fluid Dynam.* **79** 1-97.

Brandenburg, A., Tuominen, I. & Rädler, K.-H., 1989. On the generation of non-axisymmetric magnetic fields in mean-field dynamos. *Geophys. Astrophys. Fluid Dynam.* **49** 45-55.

Busse, F., 1968. Steady fluid flow in a precessing spheroidal shell. *J. Fluid Mech.* **33** 739-751.

Deinzer, W., Kusserow, H.-U.v. & Stix, M., 1974. Steady and Oscillatory $\alpha\omega$-dynamos. *Astron. Astrophys.* **36** 69-78.

Fearn, D.R., 1983. Hydromagnetic waves in a differentially rotating annulus I. A test of local stability analysis. *Geophys. Astrophys. Fluid Dynam.* **27** 137-162.

Fearn, D.R., 1984. Hydromagnetic waves in a differentially rotating annulus II. Resistive instabilities. *Geophys. Astrophys. Fluid Dynam.* **30** 227-239.

Fearn, D.R., 1985. Hydromagnetic waves in a differentially rotating annulus III. The effect of an axial field. *Geophys. Astrophys. Fluid Dynam.* **33** 185-197.

Fearn, D.R., 1988. Hydromagnetic waves in a differentially rotating annulus IV. Insulating boundaries. *Geophys. Astrophys. Fluid Dynam.* **44** 55-75.

Fearn, D.R., 1994. Nonlinear Planetary Dynamos, In: Lectures on Solar and Planetary Dynamos. Cambridge University Press.

Fearn, D.R., Lamb, C.J., McLean, D.R. & Ogden, R.R., 1997. The influence of differential rotation on magnetic instability and nonlinear magnetic instability in the magnetostrophic limit. *Geophys. Astrophys. Fluid Dynam.* **86** 173-200.

Glatzmaier, G.A. & Roberts, P.H., 1996. Rotation and magnetism of Earth's inner core. *Science* **274** 1887-1891.

Greenspan, H.P., 1968. The Theory of Rotating Fluids. Cambridge University Press.

Gubbins, D., 1972. Kinematic dynamos and geomagnetism. *Nature* **238 PS** 119-121.

Gubbins, D., 1973. Numerical solutions of the kinematic dynamo problem. *Phil. Trans. R. Soc. Lond. A* **274** 493-521.

Gubbins, D., Masters, T.G. & Jacobs, J.A., 1979. Thermal evolution of the Earth's core. *Geophys. J. R. Astr. Soc.* **59** 57-99.

Henderson, G.A. & Aldridge, K.D., 1992. A finite-element method for inertial waves in a frustum. *J. Fluid Mech.* **234** 317-327.

Hollerbach, R., 1991. Parity coupling in α^2-dynamos. *Geophys. Astrophys. Fluid Dynam.* **60** 245-260.

Hollerbach, R., 1997. The dynamical balance in semi-Taylor states. *Geophys. Astrophys. Fluid Dynam.* **84** 85-98.

Hollerbach, R., 1998. What can the observed rotation of the Earth's inner core reveal about the state of the outer core?. *Geophys. J. Int.* **135** 564-572.

Hollerbach, R., Barenghi, C.F. & Jones, C.A., 1992. Taylor's constraint in a spherical $\alpha\omega$-dynamo. *Geophys. Astrophys. Fluid Dynam.* **67** 3-25.

Hollerbach, R. & Glatzmaier, G.A., 1998. Mixed-parity solutions in a mean-field dynamo model. *Studia geoph. et geod.* **42** 239-246.

Hollerbach, R. & Ierley, G.R., 1991. A modal α^2-dynamo in the limit of asymptotically small viscosity. *Geophys. Astrophys. Fluid Dynam.* **56** 133-158.

Hollerbach, R. & Jones, C.A., 1993a. A geodynamo model incorporating a finitely conducting inner core. *Phys. Earth. planet. Int.* **75** 317-327.

Hollerbach, R. & Jones, C.A., 1993b. Influence of the Earth's inner core on geomagnetic fluctuations and reversals. *Nature* **365** 541-543.

Hollerbach, R. & Jones, C.A., 1995. On the magnetically stabilizing role of the Earth's inner core. *Phys. Earth. planet. Int.* **87** 171-181.

Hollerbach, R. & Kerswell, R.R., 1995. Oscillatory internal shear layers in rotating and precessing flows. *J. Fluid Mech.* **298** 327-339.

Hollerbach, R. & Proctor, M.R.E., 1993. Non-axisymmetric shear layers in a rotating spherical shell, In: Theory of Solar and Planetary Dynamos. Cambridge University Press.

Hutcheson, K.A. & Fearn, D.R., 1995. The nonlinear evolution of magnetic instabilities in a rapidly rotating annulus. *J. Fluid Mech.* **291** 343-368.

Hutcheson, K.A. & Fearn, D.R., 1996. The stability of toroidal magnetic fields with equatorial symmetry: implications for the Earth's magnetic field. *Phys. Earth. planet. Int.* **97** 43-54.

Hutcheson, K.A. & Fearn, D.R., 1997. The stability of toroidal magnetic fields with equatorial symmetry: evolution of instabilities. *Phys. Earth. planet. Int.* **99** 19-32.

Ivanova, T.S. & Ruzmaikin, A.A., 1977. A nonlinear magnetohydrodynamic model of the solar dynamo. *Sov. Astron.* **21** 479-485.

Jennings, R.L. & Weiss, N.O., 1991. Symmetry-breaking in stellar dynamos. *Mon. Not. R. Astron. Soc.* **252** 249-260.

Jepps, S.A., 1975. Numerical models of hydromagnetic dynamos. *J. Fluid Mech.* **67** 625-646.

Katayama, J.S., Matsushima, M. & Honkura, Y., 1999. Some characteristics of magnetic field behaviour in a model of MHD dynamo thermally driven in a rotating spherical shell. *Phys. Earth. planet. Int.* **111** 141-159.

Kerswell, R.R., 1993. The instability of precessing flow. *Geophys. Astrophys. Fluid Dynam.* **72** 107-144.

Kerswell, R.R., 1995. On the internal shear layers spawned by the critical regions in oscillatory Ekman boundary layers. *J. Fluid Mech.* **298** 311-325.

Kerswell, R.R., 1996. Upper bounds on the energy dissipation in turbulent precession. *J. Fluid Mech.* **321** 335-370.

Kerswell, R.R. & Davey, A., 1996. On the linear instability of elliptic pipe flow. *J. Fluid Mech.* **316** 307-324.

Kleeorin, N.I. & Ruzmaikin, A.A., 1984. Mean-field dynamo with cubic non-linearity. *Astron. Nachr.* **305** 265-275.

Knobloch, E., Tobias, S.M. & Weiss, N.O., 1998. Modulation and symmetry changes in stellar dynamos. *Mon. Not. R. Astron. Soc.* **297** 1123-1138.

Kuang, W., Bloxham, J., 1997. A numerical model of the generation of the Earth's magnetic field. *Nature* **365** 371-374.

Levy, E.H., 1972. Kinematic reversal schemes for the geomagnetic dipole. *Astrophys. J.* **171** 635-642.

Lilley, F.E.M., 1970. On kinematic dynamos. *Proc. R. Soc. Lond.* A **316** 153-167.

Liu, L., 1986. Potassium and the Earth's core. *Geophys. Res. Lett.* **13** 1145-1148.

Loper, D.E., 1975. Torque balance and energy budget for the precessionally driven dynamo. *Phys. Earth. planet. Int.* **11** 43-60.

Loper, D.E., 1978. The gravitationally powered dynamo. *Geophys. J. R. Astr. Soc.* **54** 389-404.

Loper, D.E. & Roberts, P.H., 1981. A study of conditions at the inner core boundary of the Earth. *Phys. Earth. planet. Int.* **24** 302-307.

Malkus, W.V.R., 1968. Precession of the Earth as the cause of geomagnetism. *Science* **160** 259-264.

Malkus, W.V.R. & Proctor, M.R.E., 1975. The macrodynamics of α-effect dynamos in rotating fluids. *J. Fluid Mech.* **67** 417-443.

McLean, D.R., 1997. Magnetohydrodynamic instabilities in a rapidly rotating system. Phd. Thesis. University of Glasgow.

McLean, D.R. & Fearn, D.R., 1996. The classification of magnetic instabilities. *Geophys. Astrophys. Fluid Dynam.* **82** 221-236.

McLean, D.R. & Fearn, D.R., 1999. The geostrophic nonlinearity and its effect on magnetic stability. *Geophys. Astrophys. Fluid Dynam.* **90** 79-112.

Moffat, H.K., 1978. Magnetic Field Generation in Electrically Conducting Fluids. Cambridge University Press.

Morrison, G. & Fearn, D.R., 2000. The influence of Rayleigh number, azimuthal wavenumber, and inner core radius on $2\frac{1}{2}$D hydromagnetic dynamos. *Phys. Earth. planet. Int.* **117** 237-258.

Ogden, R.R. & Fearn, D.R., 1995. The destabilising nature of differential rotation. *Geophys. Astrophys. Fluid Dynam.* **81** 215-232.

Olson, P., Christensen, U. & Glatzmaier, G.A., 1999. Numerical modeling of the geodynamo: Mechanisms of field generation and equilibration. *J. Geophys. Res. - Solid Earth* **104** 10383-10404.

Parker, E.N., 1955. Hydromagnetic dynamo models. *Astrophys. J.* **121** 293-314.

Parker, E.N., 1969. The occasional reversal of the geomagnetic field. *Astrophys. J.* **158** 815-827.

Parker, L.J., Atou, T. & Badding, J.V., 1996. Transition element-like chemistry for potassium under pressure. *Science* **273** 95-97.

Poincaré, H., 1910. Sur la précession des corps deformable. *Bull. Astron.* **27** 231.

Proctor, M.R.E., 1977. Numerical solutions of nonlinear α-effect dynamo equations. *J. Fluid Mech.* **80** 769-784.

Proudman, I., 1956. The almost-rigid rotation of viscous fluid between concentric spheres. *J. Fluid Mech.* **1** 505-516.

Rädler, K.-H., 1984. On spherical mean-field dynamo models with coupling between axisymmetric and non-axisymmetric field modes. *Astron. Nachr.* **305** 289-294.

Rädler, K.-H. & Wiedemann, E., 1989. Numerical experiments with a simple nonlinear mean-field dynamo model. *Geophys. Astrophys. Fluid Dynam.* **49** 71-79.

Rieutord, M., 1995. Inertial modes in the liquid core of the Earth. *Phys. Earth. planet. Int.* **91** 41-46.

Rieutord, M. & Valdettaro, L., 1997. Inertial waves in a rotating spherical shell. *J. Fluid Mech.* **341** 77-99.

Roberts, P.H., 1972. Kinematic dynamo models. *Phil. Trans. R. Soc. Lond. A* **272** 663-703.

Roberts, P.H. & Stewartson, K., 1963. On the stability of a Maclaurin spheroid of small viscosity. *Astrophys. J.* **137** 777-790.

Rochester, M.G., Jacobs, J.A., Smylie, D.E., & Chong, K.F., 1975. Can precession power the geomagnetic dynamo?. *Geophys. J. R. astr. Soc.* **43** 661-678.

Sarson, G.R., Jones, C.A. & Longbottom, A.W., 1998. Convection driven geodynamo models of varying Ekman number. *Geophys. Astrophys. Fluid Dynam.* **88** 225-259.

Secco, R.A. & Schloessin, H.H., 1989. The electrical-resistivity of solid and liquid Fe at pressures up to 7-GPa. *J. Geophys. Res.* **94** 5887-5894.

Steenbeck, M. & Krause, F., 1966. Erklärung stellarer und planetarer Magnetfelder durch einen turbulenzbedingten Dynamomechanismus. *Zeit. Naturforsch.* **21a** 1285-1296.

Steenbeck, M. & Krause, F., 1969. Zur Dynamotheorie stellarer und planetarer Magnetfelder I. Berechnung sonnenähnlicher Wechselfeldgeneratoren. *Astron. Nachr.* **291** 49-84.

Steenbeck, M., Krause, F. & Rädler, K.-H., 1966. Berechnung der mittleren Lorentz-Feldstärke $\overline{\mathbf{v} \times \mathbf{B}}$ für ein elektrisch leitendendes Medium in turbulenter, durch Coriolis-Kräfte beeinflußter Bewegung. *Z. Naturforsch.* **21a** 369-376.

Stewartson, K., 1957. On almost rigid rotations. *J. Fluid Mech.* **3** 17-26.

Stewartson, K., 1965. On almost rigid rotations. Part 2. *J. Fluid Mech.* **26** 131-144.

Stewartson, K. & Roberts, P.H., 1963. On the motion of a liquid in a spheroidal cavity of a precessing rigid body. *J. Fluid Mech.* **17** 1-20.

Stix, M., 1972. Nonlinear dynamo waves. *Astron. Astrophys.* **20** 9-12.

Tobias, S.M., 1997. The solar cycle: Parity interactions and amplitude modulation. *Astron. Astrophys.* **322** 1007-1017.

Taylor, J.B., 1963. The magnetohydrodynamics of a rotating fluid and the Earth's dynamo problem. *Proc. R. Soc. Lond.* A **274** 274-283.

Tilgner, A., 1998. On models of precession driven core flow. *Studia geoph. et geod.* **42** 232-238.

Verhoogen, J., 1961. Heat balance of the Earth's core. *Geophys. J. R. Astr. Soc.* **4** 276-281.

Walker, M.R. & Barenghi, C.F., 1997. Magnetoconvection in a rapidly rotating sphere. *Geophys. Astrophys. Fluid Dynam.* **85** 129-162.

Walker, M.R. & Barenghi, C.F., 1998. Accurate numerical computations of Taylor integrals. *Geophys. Astrophys. Fluid Dynam.* **87** 173-191.

Walton, I.C., 1975. Viscous shear layers in an oscillating rotating fluid. *Proc. R. Soc. Lond.* A **344** 101-110.

Zhang, K. & Fearn, D.R., 1994. Hydromagnetic waves in rapidly rotating spherical shells generated by magnetic toroidal decay modes. *Geophys. Astrophys. Fluid Dynam.* **77** 133-157.

Zhang, K. & Fearn, D.R., 1995. Hydromagnetic waves in rapidly rotating spherical shells generated by poloidal decay modes. *Geophys. Astrophys. Fluid Dynam.* **81** 193-209.

Zhang, K. & Jones, C.A., 1996. On small Roberts number magnetoconvection in rapidly rotating systems. *Proc. R. Soc. Lond.* A **452** 981-995.

Zhang, K. & Jones, C.A., 1997. The effect of hyperviscosity on geodynamo models. *Geophys. Res. Lett.* **24** 2869-2872.

Zhang, K., Jones, C.A. & Sarson, G.R., 1998. The dynamical effects of hyperviscosity on numerical geodynamo models. *Studia geoph. et geod.* **42** 247-253.